ALMA MATER STUDIORUM
UNIVERSITÀ DI BOLOGNA

DEPARTMENT OF PHYSICS AND ASTRONOMY ”A. RIGHI”

SECOND CYCLE DEGREE

PHYSICS

Analysis of the $D^0 \to K^- \pi^+ e^- e^+$ decay with the LHCb Upgrade I detector

Supervisor
Dr. Fabio Ferrari

Co-supervisors
Dr. Marianna Fontana
Dr. Alberto Bellavista

Defended by
Sofia Zalambani

Graduation Session 09/2025

Academic Year 2024/2025

La vita è più bella quando si ride!

Abstract

Rare charm decays, such as $D^0 \to K^-K^+e^-e^+$ and $D^0 \to \pi^-\pi^+e^-e^+$, provide a sensitive probe in the search for New Physics. In particular, a measurement of a branching fraction that significantly deviates from the Standard Model prediction could constitute a first indication of physics beyond the Standard Model. In this framework, the decay $D^0 \to K^-\pi^+e^-e^+$ is of particular importance, as it serves as the natural normalization channel for the aforementioned rare decays.

In this thesis, the yields of the normalization channel are determined for the first time using data collected with the upgraded LHCb detector. The analysis is based on proton–proton collision data recorded during Run 3 of the LHC at a center-of-mass energy of $\sqrt{s} = 13.6$ TeV.

The signal yields are extracted from unbinned maximum-likelihood fits to the invariant mass distributions of D^0 candidates. The selection and fit strategies are optimized to account for differences between decays with zero or at least one reconstructed bremsstrahlung photon. The background shapes used in the fit model are studied with RapidSim, a fast simulation framework for heavy-hadron decays, following a dedicated validation presented in this thesis.

The measured yields of the signal channel are 7389 ± 172 and 1130 ± 78 for the cases in which at least one reconstructed photon is associated with the decay, or no photon is associated, respectively. The quoted uncertainties are statistical only, as determined from the fits. This study will be extended within the LHCb experiment in the ongoing search for rare charm decays.

Contents

List of Figures

List of Tables

Introduction

The Standard Model (SM), which describes three of the four fundamental forces of Nature, represents one of the greatest achievements of the particle physics community. It is a well-established theoretical framework that aims to describe the Universe, and over the past decades it has been extensively tested through precise measurements of observables and theoretical predictions. However, several phenomena remain unexplained within the SM, pointing to the existence of physics beyond it. Notable examples include the hierarchy problem, the origin of neutrino masses, the nature of dark matter and dark energy, and the absence of gravity in the SM description of fundamental interactions.

At present, precision tests of SM observables are pursued in the search for new particles or interactions that could explain potential deviations from SM expectations. Experimentally, such searches can be carried out either directly, by looking for new particles in high-energy collisions at accelerators, or indirectly, by probing SM properties with increasing precision.

The Large Hadron Collider (LHC) at CERN is the most powerful particle accelerator ever constructed. Along its ring, four major experiments are installed, including the LHCb detector, which is dedicated to the study of flavour physics. A powerful probe of physics beyond the SM is the measurement of branching fractions of rare decays. In particular, rare semileptonic charm decays, governed by both long- and short-distance contributions, are especially sensitive since they proceed through quantum loops, where new particles or interactions may appear, potentially leading to deviations from SM predictions. The study of rare channels such as $D^0 \to h^-h^+e^-e^+$, with $h = \pi, K$, is therefore particularly promising. The study of rare decays is typically performed by normalizing to a more favored, topologically similar channel, in order to cancel systematic uncertainties in the ratio of branching fractions. In this case, the natural candidate for normalization is the $D^0 \to K^-\pi^+e^-e^+$ decay.

In this thesis, the first determination of the yields of the normalization channel using data collected with the upgraded LHCb detector during Run 3 of the LHC is presented. By comparing the extracted yields with those obtained using Run 2 data, the performance of the upgraded detector can be assessed.

This thesis is organized as follows: Chapter 1 introduces the theoretical framework of the SM, with a historical and theoretical overview of meson mixing, one of the most intriguing phenomena of flavour physics, which also accounts for the suppression of rare decays. Chapter 2 describes the upgraded LHCb detector. Chapter 3 presents the analysis of the $D^0 \to K^-\pi^+e^-e^+$ decay, including the event selection, validation, and the use of the fast simulation tool - RapidSim - to model background distributions. The extraction of the signal yields from fits to the invariant mass of the D^0 candidates is also discussed in detail. Finally, the conclusions are summarized.

1 Theory of rare charm decays

1.1 The Standard Model of particle physics

The Standard Model (SM) of particle physics is a quantum field theory that classifies all known elementary particles and describes their interactions via three out of the four fundamental forces: strong, weak and electromagnetic. The fourth fundamental force, gravity, is not included.

It is based on a gauge field theory which is locally invariant under the symmetry group

$$G = SU(3)_C \otimes SU(2)_L \otimes U(1)_Y . \tag{1}$$

The $SU(3)_C$ symmetry group leads to Quantum Chromodynamics (QCD), the theory of strong interaction, which is related to color charge. On the other hand, $SU(2)_L \otimes U(1)_Y$ represents the electroweak sector after the unification through the Glashow – Weinberg – Salam (GWS) model [1, 2, 3]: the former symmetry group accounts for the weak interaction, which couples only with left-handed (LH) fermions, while the latter is associated to the weak hypercharge Y and gives rise to the electromagnetic interaction after the spontaneous symmetry breaking via the Higgs mechanism.

Ordinary matter is composed of fermions that are particles with half-integer spin, split into quarks and leptons, both divided into 3 generations (also called families). Each quark and each lepton is made of two fields with opposite chirality: left-handed and right-handed ones. The left-handed fields of the two quarks of the same generation are grouped together into a chirality doublet ($Q_{L,i}$). The same applies to leptons ($L_{L,i}$). On the other hand, right-handed chirality fields are in singlet of $SU(2)_L$.

The fermionic fields are:

$$\begin{aligned} Q_{L,i} &= \begin{pmatrix} u_{L,i} \\ d_{L,i} \end{pmatrix}, \quad u_{R,i}, \quad d_{R,i}, \\ L_{L,i} &= \begin{pmatrix} \nu_{L,i} \\ \ell_{L,i} \end{pmatrix}, \quad \nu_{R,i}, \quad \ell_{R,i}. \end{aligned} \tag{2}$$

The interactions between particles are mediated by bosons, that have integer spin: the photon mediates the electromagnetic interaction, the 8 gluons mediate the strong force between quarks, and the W^+, W^- and Z^0 bosons mediate the weak force. The Higgs boson, discovered in 2012 [4, 5], explains how particles acquire mass through the Higgs mechanism. The Standard Model of particle physics is represented in Fig. 1.

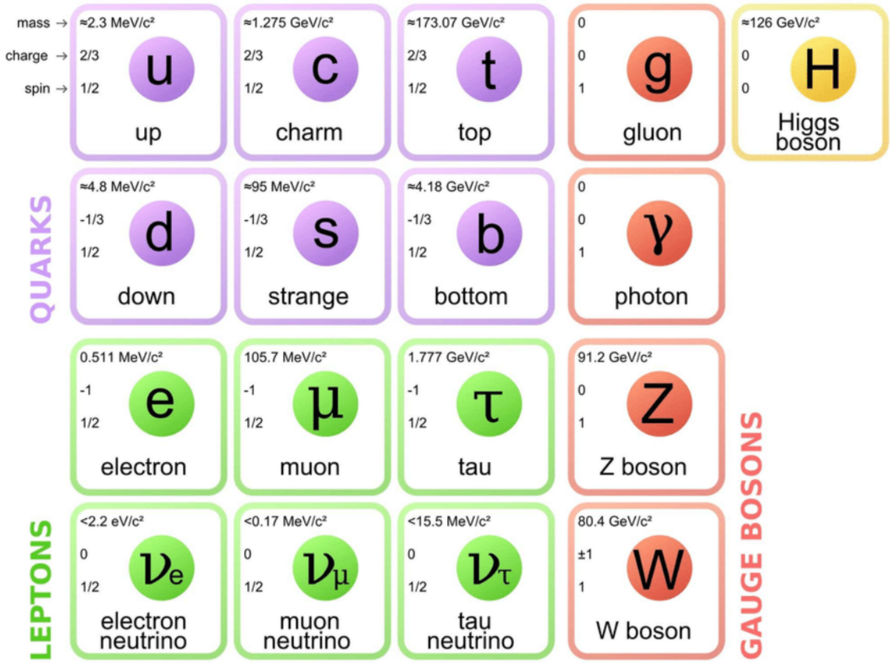

Figure 1: *Pictorial representation of the Standard Model. There are matter fields, i.e. 3 generations of quarks and leptons; 12 force carriers, i.e. fundamental gauge fields (8 gluons, 3 W_μ's and B_μ) and finally the Higgs boson, responsible for particles' masses.*

1.2 Historical overview

1.2.1 The quark mixing and the Cabibbo hypothesis

The problem After the introduction of the strange quantum number in 1953 [6, 7], later associated to the strange quark in 1964 [8], the existence of weak processes that didn't conserve the strangeness quantum number S ($\Delta S = 1$), implied the possibility of transitions among different doublets. The analysis of these decays with respect to the ones conserving the strangeness quantum number ($\Delta S = 0$) showed a different intensity between these processes. In particular, those with variation in the strangeness composition were rarest. This consideration seemed to imply a non universal behaviour of the weak interaction, characterized by different couplings between u and d with respect to u and s quarks, *i.e.* $g_{du} \neq g_{su}$.

Cabibbo's hypothesis In 1963 Nicola Cabibbo proposed that the weak interaction eigenstates are not the same as the mass eigenstates (the states that have definite masses and participate in the strong interactions). Instead, the weak eigenstates are mixtures of the mass ones [9]. This mixing can be described by a rotation in the quark flavor space, characterized by the Cabibbo angle, as described by the following expressions

$$\begin{pmatrix} u \\ d' \end{pmatrix} = \begin{pmatrix} u \\ d\cos\theta_C + s\sin\theta_C \end{pmatrix}, \qquad \begin{pmatrix} u \\ s' \end{pmatrix} = \begin{pmatrix} u \\ -d\sin\theta_C + s\cos\theta_C \end{pmatrix}, \tag{3}$$

where d' and s' represent the weak eigenstates, that are linear combinations of the mass ones. According to this hypothesis, coupling is still universal and the quark doublet in weak interaction is redefined by mixing which implies the different intensities in the coupling between u and d with respect to u and s. In particular, the leptons are weak eigenstates and for each lepton doublet the weak coupling is G_F. On the other hand, for transitions involving quarks u and d, with $\Delta S = 0$, the coupling constant corresponds to $G_F \cos\theta_C$; while for transitions involving quarks u and s, with $\Delta S = 1$, the coupling constants corresponds to $G_F \sin\theta_C$. The different value of the effective coupling constants is only due to the quark mixing process to form the weak eigenstates and since $\sin\theta_C \approx 0.225$, while $\cos\theta_C \approx 0.974$, transitions with $\Delta S = 0$ have an effective coupling constants larger than those with $\Delta S = 1$ [10]. At that time, the angle θ was determined through the comparison of the rates for the positive pion and positive kaon decays, respectively $\pi^+ \to \pi^0 + e^+ + \nu$ and $K^+ \to \pi^0 + e^+ + \nu$, yielding $\theta_C = 0.257$ rad [9], which corresponds to $14.72°$. At present, the Cabibbo angle is determined from high-precision measurements of the elements $|V_{ud}|$ and $|V_{us}|$ of the CKM matrix, yielding $\theta_C = 13°$ [11].

1.2.2 The GIM mechanism

The problem: Absence of Flavour Changing Neutral Currents According to Cabibbo's original formulation of quark mixing, the charged weak currents mediated by the W bosons are affected by the mixing, allowing transitions such as $u \to s$ and explaining their relative suppression. However, in this three-quark framework, the neutral weak currents are not flavour-diagonal at tree-level. This leads to flavor changing neutral current (FCNC) processes, involving for example $d \to s$ quark transitions. The problem lies in the fact that the experimentally observed suppression of these decays cannot be justified in this framework. The theoretical demonstration is now presented.

Let's recall that in the SM the weak interaction theory is based on the symmetry group $SU(2)_L \times U(1)_Y$. The three generators of $SU(2)$ are τ^a, expressed as functions of the Pauli matrices σ^a, as

$$\tau^a = \frac{\sigma^a}{2}, \qquad a = 1, 2, 3 \tag{4}$$

The corresponding vector fields are W_μ^a. The interaction Lagrangian is

$$\begin{aligned}\mathcal{L}_{int} &= -g\overline{\psi_L}\gamma^\mu\tau^a\psi_L W_\mu^a \\ &= -gJ_\mu^a W_\mu^a\end{aligned} \tag{5}$$

where g is the weak coupling constant, ψ_L a weak doublet, γ_μ the Dirac matrices and J_μ^a the current.

Generally, it is convenient to write the Lagrangian in terms of the charge raising and lowering operators, defined as

$$\begin{aligned}\tau^+ &= \frac{\sigma_1 + i\sigma_2}{2}, \qquad W_\mu^+ = \frac{1}{\sqrt{2}}(W_\mu^1 - iW_\mu^2), \\ \tau^- &= \frac{\sigma_1 - i\sigma_2}{2}, \qquad W_\mu^- = \frac{1}{\sqrt{2}}(W_\mu^1 + iW_\mu^2).\end{aligned} \tag{6}$$

Exploiting the tau operators one obtains the charged currents and the neutral current. The charged currents are

$$J_\mu^+ = \overline{\psi_L}\gamma_\mu\tau^+\psi_L \quad \text{and} \quad J_\mu^- = \overline{\psi_L}\gamma_\mu\tau^-\psi_L, \tag{7}$$

that become at the quark level considering the Cabibbo mixing:

$$\begin{aligned}J_\mu^+ &= (\overline{u}_L, \overline{d'}_L)\gamma_\mu \begin{pmatrix}0 & 1\\ 0 & 0\end{pmatrix}\begin{pmatrix}u_L\\ d'_L\end{pmatrix} = \overline{u}_L\gamma_\mu d'_L = \cos\theta_C\,\overline{u}_L\gamma_\mu d_L + \sin\theta_C\,\overline{u}_L\gamma_\mu s_L, \\ J_\mu^- &= (\overline{u}_L, \overline{d'}_L)\gamma_\mu \begin{pmatrix}0 & 0\\ 1 & 0\end{pmatrix}\begin{pmatrix}u_L\\ d'_L\end{pmatrix} = \overline{d'}_L\gamma_\mu u_L = \cos\theta_C\,\overline{d}_L\gamma_\mu u_L + \sin\theta_C\,\overline{s}_L\gamma_\mu u_L.\end{aligned} \tag{8}$$

In addition to charged currents, the third generator gives rise to a neutral current of the form:

$$J_\mu^0 = \overline{\psi_L}\gamma_\mu\tau^3\psi_L. \tag{9}$$

At the quark level, considering the Cabibbo mixing one has:

$$\begin{aligned}J_\mu^0 &= \frac{1}{2}(\overline{u}_L, \overline{d'}_L)\gamma_\mu \begin{pmatrix}1 & 0\\ 0 & -1\end{pmatrix}\begin{pmatrix}u_L\\ d'_L\end{pmatrix} \\ &= \frac{1}{2}\left[\overline{u}_L\gamma_\mu u_L - \overline{d'}_L\gamma_\mu d'_L\right] \\ &= \frac{1}{2}\underbrace{\left[\overline{u}_L\gamma_\mu u_L - \overline{d}_L\gamma_\mu d_L\cos\theta_C{}^2 - \overline{s}_L\gamma_\mu s_L\sin\theta_C{}^2\right]}_{\Delta S=0} \\ &\quad - \frac{1}{2}\underbrace{(\overline{s}_L\gamma_\mu d_L + \overline{d}_L\gamma_\mu s_L)\sin\theta_C\cos\theta_C}_{\Delta S=1}\end{aligned} \tag{10}$$

The last term corresponding to $\Delta S = 1$ neutral current is allowed, therefore, the Cabibbo theory alone does not explain the observed suppression of decays involving FCNC.

In conclusion, considering only the Cabibbo mixing hypothesis and having to assume the existence of the intermediate boson Z^0 necessary for the internal consistency of the theory, the problem is not yet solved.

The GIM mechanism The solution was proposed in 1970 by Glashow, Iliopoulos and Maiani who postulated the existence of a fourth up-type quark with charge $+2/3$, belonging to the second doublet [12], the charm quark c

$$\begin{aligned}
\begin{pmatrix} u \\ d' \end{pmatrix} &= \begin{pmatrix} u \\ d\cos\theta_C + s\sin\theta_C \end{pmatrix}, \\
\begin{pmatrix} c \\ s' \end{pmatrix} &= \begin{pmatrix} c \\ s\cos\theta_C - d\sin\theta_C \end{pmatrix}.
\end{aligned}$$

The introduction of this new quark implied that the quark d' and s' are connected to d and s through a unitary transformation:

$$\begin{pmatrix} d' \\ s' \end{pmatrix} = \begin{pmatrix} \cos\theta_C & \sin\theta_C \\ -\sin\theta_C & \cos\theta_C \end{pmatrix} \begin{pmatrix} d \\ s \end{pmatrix} \tag{11}$$

Assuming the existence of the charm quark, the flavour changing terms in the neutral current due to Z^0 exchange get exactly canceled and the relation in Eq. (12) is obtained, where the $\Delta S = 1$ part is equal to 0.

$$\begin{aligned}
J^0_\mu &= \frac{1}{2}(\overline{u}_L, \overline{d'}_L)\gamma_\mu \begin{pmatrix} 1 & 0 \\ 0 & -1 \end{pmatrix} \begin{pmatrix} u_L \\ d'_L \end{pmatrix} + \frac{1}{2}(\overline{c}_L, \overline{s'}_L)\gamma_\mu \begin{pmatrix} 1 & 0 \\ 0 & -1 \end{pmatrix} \begin{pmatrix} c_L \\ s'_L \end{pmatrix} \\
&= \frac{1}{2}\left[\overline{u}_L\gamma_\mu u_L - \overline{d'}_L\gamma_\mu d'_L + \overline{c}_L\gamma_\mu c_L - \overline{s'}_L\gamma_\mu s'_L\right] \\
&= \frac{1}{2}\underbrace{\left[\overline{u}_L\gamma_\mu u_L + \overline{c}_L\gamma_\mu c_L - (\overline{d}_L\gamma_\mu d_L + \overline{s}_L\gamma_\mu s_L)\cos\theta_C{}^2 - (\overline{d}_L\gamma_\mu d_L + \overline{s}_L\gamma_\mu s_L)\sin\theta_C{}^2\right]}_{\Delta S=0} \\
&\quad + \frac{1}{2}\underbrace{\left[(\overline{s}_L\gamma_\mu\, d_L + \overline{d}_L\gamma_\mu s_L - \overline{s}_L\gamma_\mu d_L - \overline{d}_L\gamma_\mu s_L)\sin\theta_C\cos\theta_C\right]}_{\Delta S=1} \\
&= \frac{1}{2}\left[\overline{u}_L\gamma_\mu u_L + \overline{c}_L\gamma_\mu c_L - (\overline{d}_L\gamma_\mu d_L + \overline{s}_L\gamma_\mu s_L)\cos\theta_C{}^2 - (\overline{d}_L\gamma_\mu d_L + \overline{s}_L\gamma_\mu s_L)\sin\theta_C{}^2\right]
\end{aligned} \tag{12}$$

The existence of the charm quark was later confirmed in 1974 in the so-called November revolution with the discovery of the J/ψ resonance at Brookhaven Lab [13] and SLAC [14].

However, before this experimental confirmation, starting from the ideas of Cabibbo and the GIM mechanism proponents, Kobayashi and Maskawa extended the framework of quark mixing to three doublets in order to include the CP violation into the Standard Model and formulated the CKM matrix [15].

1.3 The Standard Model Lagrangian

The Standard Model Lagrangian ($\mathcal{L}_{\text{SM}}$) satisfies the gauge invariance with respect to the symmetry group previously introduced in Eq. (1) and can be viewed as the sum of a kinetic term and an interaction term between the gauge bosons ($\mathcal{L}_g$), a kinetic and interaction term for fermions ($\mathcal{L}_f$), the Higgs boson term ($\mathcal{L}_H$) and finally the Yukawa term, responsible for the masses of the fermions ($\mathcal{L}_Y$). The SM Lagrangian is expressed as [16]

$$\mathcal{L}_{\text{SM}} = \mathcal{L}_g + \mathcal{L}_f + \mathcal{L}_H + \mathcal{L}_Y \tag{13}$$

A brief description of the different contributions is provided in the following.

The gluon term reads

$$\mathcal{L}_g = -\frac{1}{4}(G^a_{\mu\nu}G^{\mu\nu}_a + W^b_{\mu\nu}W^{\mu\nu}_b + B_{\mu\nu}B^{\mu\nu}), \tag{14}$$

where G^μ_a, W^μ_b and B^μ are the gauge fields for the eight gluons, for the three weak bosons and for the hypercharge boson, respectively.

The fermionic term $\mathcal{L}_f$ can be written as

$$\mathcal{L}_f = \sum_{fields} i\bar{\psi}\gamma_\mu D^\mu \psi, \tag{15}$$

where γ_μ are the Dirac matrices and ψ and $\bar{\psi}$ represent the field and its adjoint spinor.

The Higgs term reads

$$\mathcal{L}_H = (D^\mu \phi^\dagger)(D_\mu \phi) + \mu^2 \phi^\dagger \phi - \frac{\lambda^2}{2}(\phi^\dagger \phi)^2, \tag{16}$$

where λ and $\mu = v\sqrt{\lambda}$ are real positive parameters. The Higgs field is described by a weak isospin doublet,

$$\phi = \begin{pmatrix} \phi^+ \\ \phi^0 \end{pmatrix}, \tag{17}$$

and assumes a non-zero vacuum expectation value:

$$\langle 0|\phi|0\rangle = \frac{1}{\sqrt{2}}\begin{pmatrix} 0 \\ v \end{pmatrix}, \qquad \text{where } v \approx 246 \text{ GeV}. \tag{18}$$

This description allows the spontaneous symmetry breaking (SSB) [17].

Finally, the Yukawa term describing the interaction between fermions and the scalar Higgs field is reported below:

$$\mathcal{L}_Y = -Y^d_{ij}\overline{Q}_{L,i}\phi d_{R,j} - Y^u_{ij}\overline{Q}_{L,i}(i\sigma_2\phi^\dagger)u_{R,j} + h.c.\ , \tag{19}$$

and is further described in the following Section.

1.4 The CKM matrix

1.4.1 Theoretical considerations on the CKM matrix

In the SM the quark mass eigenstates do not take part as pure states in the weak interactions. These 2 bases of mass and weak eigenstates are connected by a unitary transformation: the CKM matrix.

The gauge group of electroweak interactions is $SU(2)_L \times U(1)_Y$. Left-handed quarks are in doublets of $SU(2)_L$, while right-handed component are in singlets of $SU(2)_L$.

The masses and mixing of quarks have a common origin in the SM since they both arise from the Yukawa interactions with the Higgs condensate,

$$\mathcal{L}_Y = -Y^d_{ij}\overline{Q^I_{Li}}\phi d^I_{Rj} - Y^u_{ij}\overline{Q^I_{Li}}\epsilon\phi^* u^I_{Rj} + h.c. \tag{20}$$

The Lagrangian reported in Eq. (20) [11] is the Yukawa Lagrangian where $Y^{u,d}$ are 3×3 complex matrices representing the Yukawa coupling for up-type and down-type quarks, ϕ is the Higgs field doublet, i and j are generations labels and ϵ is the 2×2 antisymmetric tensor. The fields represented by Q^I_L are left-handed quark doublets, while d^I_R and u^I_R are respectively right-handed down and up-type quark singlets, in the weak eigenstate basis. Moreover, ϕ^* is the complex conjugate of the Higgs field and $h.c.$ stands for hermitian conjugate, which ensure that the Lagrangian is hermitian [11].

In particular, the first term, $-Y^d_{ij}\bar{Q}^I_{Li}\phi d^I_{Rj}$, describes the interaction between the left-handed quark doublet Q^I_L, the Higgs field and the right-handed down-type quark d^I_R. When the Higgs field acquires a vacuum expectation value (vev), this interaction gives mass to the down-type quarks.

On the other hand, the second term, *i.e.* $-Y^u_{ij}\bar{Q}^I_{Li}\epsilon\phi^* u^I_{Rj}$, describes the interaction between the left-handed quark doublet $\bar{Q}^I_{Li}$, the conjugate of the Higgs field ϕ^* with the antisymmetric tensor ϵ (needed to ensure the invariance of the terms under the SU(2) gauge symmetry) and the right-handed up-type quark u^I_R. When the Higgs field acquires a vev, this interaction gives mass to the up-type quarks.

In particular, if $SU(2)_L \times U(1)_Y$ were an exact symmetry, then all quarks would be massless leading to indistinguishable interaction eigenbasis and mass eigenbasis [18]. However, this symmetry is broken. The breaking is spontaneous (SSB) due to a vacuum expectation value acquired by the Higgs field ϕ: $\langle\phi\rangle = (0, v/\sqrt{2})$. The physical states are obtained by diagonalizing $Y^{u,d}$ by four unitary matrices, $V^{u,d}_{L,R}$, as [11]:

$$M^u_{diag} = V^u_L Y^u V^{u\dagger}_R (v/\sqrt{2}) \quad \text{and} \quad M^d_{diag} = V^d_L Y^d V^{d\dagger}_R (v/\sqrt{2}). \tag{21}$$

The important feature of the Yukawa matrices is that they cannot be simultaneously diagonalized, so without loss of generality, one can choose to identify the up quark interaction eigenstates with the mass eigenstates ($u_{L,R} = u^I_{L,R}$) [18]. This means that, by convention, the charge $+2/3$ quarks (u, c and t) are chosen to be pure states and the flavour mixing is described in terms of a 3×3 matrix operating on the d, s and b quark states. Thus, the weak eigenstates, in analogy with the Cabibbo theory and the GIM hypothesis, are linked to the eigenstates of the strong interaction by the CKM matrix, Eq. (22).

$$\begin{pmatrix} d' \\ s' \\ t' \end{pmatrix} = V_{CKM} \begin{pmatrix} d \\ s \\ b \end{pmatrix}, \text{where } V_{CKM} \equiv V^u_L V^{d\dagger}_L = \begin{pmatrix} V_{ud} & V_{us} & V_{ub} \\ V_{cd} & V_{cs} & V_{cb} \\ V_{td} & V_{ts} & V_{tb} \end{pmatrix}. \tag{22}$$

As a result, the charged-current Lagrangian, describing the $W^\pm$ interaction coupling to the physical u_{Lj} and d_{Lk} quarks is given by Eq. (23) [11]:

$$\mathcal{L}_{CC} = \frac{-g}{\sqrt{2}} (\overline{u_L}, \overline{c_L}, \overline{t_L}) \gamma^\mu W^+_\mu V_{CKM} \begin{pmatrix} d_L \\ s_L \\ b_L \end{pmatrix} + h.c. \tag{23}$$

The CKM matrix is a unitary matrix. In general a $N \times N$ unitary matrix has $\frac{1}{2}N(N-1)$ real parameters (Euler angles) and $\frac{1}{2}(N-1)(N-2)$ phases. The $N = 2$ Cabibbo matrix contains only one real parameter and thus it cannot give rise to CP violation. In order to account for CP violation and incorporate it in the description of the SM, a complex number must appear in the Lagrangian, given by a phase in the matrix. Consequently, the minimum number of generators of the matrix is 3 [19].

The CKM matrix can be parameterized in several ways. Hereafter the standard and Wolfenstein parameterizations are reported.

1.4.2 Parameterizations of the matrix

The standard parameterization The standard parameterization [20, 21] utilizes 3 mixing angles $\theta_{12}, \theta_{23}, \theta_{13}$ and the CP-violating KM phase, $\delta_{13} = \delta$ [15],

$$\begin{aligned} V_{CKM} &= \begin{pmatrix} 1 & 0 & 0 \\ 0 & c_{23} & s_{23} \\ 0 & -s_{23} & c_{23} \end{pmatrix} \begin{pmatrix} c_{13} & 0 & s_{13}e^{-i\delta} \\ 0 & 1 & 0 \\ -s_{13}e^{i\delta} & 0 & c_{13} \end{pmatrix} \begin{pmatrix} c_{12} & s_{12} & 0 \\ -s_{12} & c_{12} & 0 \\ 0 & 0 & 1 \end{pmatrix} \\ &= \begin{pmatrix} c_{12}c_{13} & s_{12}c_{13} & s_{13}e^{-i\delta} \\ -s_{12}c_{23} - c_{12}s_{23}s_{13}e^{i\delta} & c_{12}c_{23} - s_{12}s_{23}s_{13}e^{i\delta} & s_{23}c_{13} \\ s_{12}s_{23} - c_{12}c_{23}s_{13}e^{i\delta} & -c_{12}s_{23} - s_{12}c_{23}s_{13}e^{i\delta} & c_{23}c_{13} \end{pmatrix} \end{aligned} \tag{24}$$

where $s_{ij} = \sin\theta_{ij}$ and $c_{ij} = \cos\theta_{ij}$.

The Wolfenstein parameterization Experimentally, it is observed that $s_{13} \ll s_{23} \ll s_{12} \ll 1$ [11], and it is convenient to underline this hierarchy switching to the Wolfenstein parameterization [22]. Let us define then

$$\begin{aligned} s_{12} = \lambda = \frac{|V_{us}|}{\sqrt{|V_{ud}|^2 + |V_{us}|^2}}, \quad s_{23} = A\lambda^2 = \lambda\frac{|V_{cb}|}{|V_{us}|}, \\ s_{13}e^{i\delta} = V_{ub}^* = A\lambda^3(\rho + i\eta) = \frac{A\lambda^3(\bar{\rho} + i\bar{\eta})\sqrt{1 - A^2\lambda^4}}{\sqrt{1-\lambda^2}[a - A^2\lambda^4(\bar{\rho} + i\bar{\eta})]}. \end{aligned} \tag{25}$$

It holds $\bar{\rho} + i\bar{\eta} = -\frac{(V_{ud}V_{ub}^*)}{(V_{cb}V_{cb}^*)}$, where the definitions of $\bar{\rho}$ and $\bar{\eta}$ are $\bar{\rho} = \rho(1 - \lambda^2/2 + \mathcal{O}(\lambda^3))$ and $\bar{\eta} = \eta(1 - \lambda^2/2 + \mathcal{O}(\lambda^3))$. The CKM matrix in the Wolfenstein parameterization, *i.e.* in terms of $\lambda,\ A,\ \bar{\rho}$ and $\bar{\eta}$, is unitary to all orders in λ [11].

The CKM matrix can be rewritten either in terms of $\bar{\rho}$ and $\bar{\eta}$ or, traditionally using the previous substitutions. Below we report the CKM matrix up to $O(\lambda^4)$:

$$V_{CKM} = \begin{pmatrix} 1-\lambda^2/2 & \lambda & A\lambda^3(\rho - i\eta) \\ -\lambda & 1-\lambda^2/2 & A\lambda^2 \\ A\lambda^3(1-\rho-i\eta) & -A\lambda^2 & 1 \end{pmatrix} + O(\lambda^4). \tag{26}$$

This formulation is quite interesting since it highlights the properties that differentiate this unitary matrix from a common one. Indeed, the CKM matrix is almost diagonal, with the diagonal elements which are close to unity, and the other elements decreasing in magnitude with increasing distance from the diagonal, according to a nearly symmetrical pattern. The latter statement indicates that the transitions between different families are suppressed by powers of λ, depending on the distance between them. Transitions between quarks of the same generation are called Cabibbo-favored and are described by tree-level Feynman diagrams. On the other hand, transitions between quarks of the first and second generation are called (single) Cabibbo-suppressed; and finally those between quark of the second and third generation are called doubly-Cabibbo suppressed.

Moreover, recalling that in order to account for CP violation there must be a phase in the matrix and considering Eq. (25), the following relation is found

$$\tan\delta_{13} = \frac{\eta}{\rho}. \tag{27}$$

Therefore, $\eta \neq 0$ is the CP symmetry-breaking condition in the Standard Model [19].

1.4.3 The unitarity triangle

The unitarity of the CKM matrix imposes that $\sum_i V_{ij} V^*_{ik} = \delta_{jk}$ and $\sum_j V_{ij} V^*_{kj} = \delta_{ik}$, with indices i, j and k representing the label for the quark generations [11]. Then one obtains the following relations, 9 in total

$$\begin{aligned}
|V_{ud}|^2 + |V_{us}|^2 + |V_{ub}|^2 &= 1, \\
|V_{cd}|^2 + |V_{cs}|^2 + |V_{cb}|^2 &= 1, \\
|V_{td}|^2 + |V_{ts}|^2 + |V_{tb}|^2 &= 1, \\
V^*_{ud} V_{cd} + V^*_{us} V_{cs} + V^*_{ub} V_{cb} &= 0, \\
V^*_{ud} V_{td} + V^*_{us} V_{ts} + V^*_{ub} V_{tb} &= 0, \\
V^*_{cd} V_{td} + V^*_{cs} V_{ts} + V^*_{cb} V_{tb} &= 0, \\
V^*_{ud} V_{us} + V^*_{cd} V_{cs} + V^*_{td} V_{ts} &= 0, \\
V^*_{ud} V_{ub} + V^*_{cd} V_{cb} + V^*_{td} V_{tb} &= 0, \\
V^*_{us} V_{ub} + V^*_{cs} V_{cb} + V^*_{ts} V_{tb} &= 0.
\end{aligned} \tag{28}$$

The first three conditions provide a way of testing the unitary condition [19]. The six vanishing equations can be represented as triangles in a complex plane ($\overline{\rho} - \overline{\eta}$), all of them having the same area, equal to half of the Jarlskog invariant J [23], which is a phase-convention-independent measure of CP violation [11], defined by

$$\Im\left[V_{ij} V_{kl} V^*_{il} V^*_{kj}\right] = J \sum_{m,n} \epsilon_{ikm}\, \epsilon_{jln}. \tag{29}$$

The unitary triangle most frequently considered originates from

$$V_{ud} V^*_{ub} + V_{cd} V^*_{cb} + V_{td} V^*_{tb} = 0. \tag{30}$$

Dividing by $V_{cd} V^*_{cb}$, the length of one side can be normalized to the real value of one

$$\begin{aligned}
1 + \frac{V_{td} V^*_{tb}}{V_{cd} V^*_{cb}} + \frac{V_{ud} V^*_{ub}}{V_{cd} V^*_{cb}} &= 0 \\
1 + \frac{V_{td} V^*_{tb}}{V_{cd} V^*_{cb}} &= (\rho + i\eta)(1 - \frac{\lambda^2}{2}) + O(\lambda^4).
\end{aligned} \tag{31}$$

Then, considering the definitions of $\bar{\rho}$ and $\bar{\eta}$, one can derive that the unitarity triangle has vertices $(0, 0)$, $(1, 0)$ and $(\overline{\rho}, \overline{\eta})$. Moreover, the angles are α, β and γ (sometimes called ϕ_1, ϕ_2 and ϕ_3), where the latter is equal to the phase δ_{13} of the canonical parameterization since $\gamma = \arctan \frac{\overline{\eta}}{\overline{\rho}} = \arctan \frac{\eta}{\rho} = \delta_{13}$ [19].

The unitarity triangle described above is shown in Fig. 2.

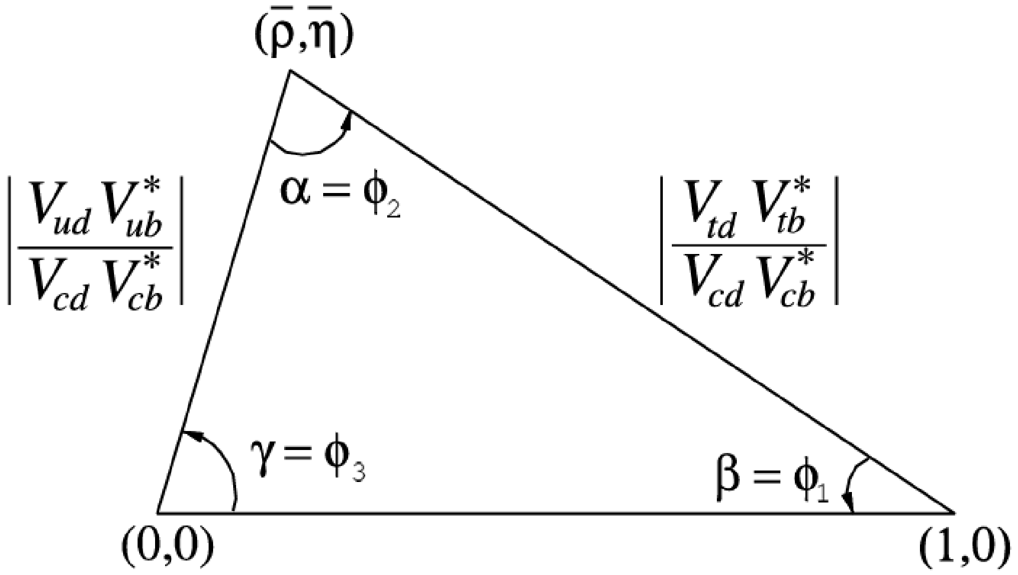

Figure 2: *The unitary triangle of the CKM matrix.*

1.4.4 Evaluation of the magnitudes of the CKM elements and phases

The values of the elements of the CKM matrix are not predicted by the model and so they need to be determined experimentally. In fact the values of the matrix elements are free parameters, constrained only by the requirement of unitarity. Here follows a brief description of the latest decays used to evaluate their magnitudes [11]. For each element of the matrix the decays and latest average results are hereafter reported:

- $|V_{ud}|$: Precise values have been obtained from super-allowed nuclear decays, neutron beta decay ($n \to pe^-\bar{\nu_e}$) and pion beta decays ($\pi^+ \to \pi^0 e^+ \nu_e$).
- $|V_{us}|$: The value is obtained considering semileptonic decay modes of kaon mesons $K_L^0, K_S^0, K^\pm$, such as $K_L^0 \to \pi e \nu$, and pion and kaon decays into a muonic lepton pair as $\pi^- \to \mu^- \bar{\nu_\mu}$.
- $|V_{cd}|$: Semileptonic decays as $D^+ \to \pi^0 \ell^+ \nu_\ell$ and leptonic decays as $D^+ \to \tau^+ \nu_\tau$ are used to provide an estimate of this element. It is noteworthy that earlier measurements comes also from neutrino scattering data on nucleon.
- $|V_{cs}|$: It is evaluated by means of decay rate measurements of leptonic and semileptonic decays of the D mesons, as $D_s^+ \to \mu^+ \nu_\mu$ and $D^+ \to K^0 \ell^+ \nu_\ell$. Additional evaluations of this matrix element come from W boson decays.

- $|V_{cb}|$: Its value cannot be measured directly, thus two decay processes are considered: the inclusive semileptonic decay of b-hadrons corresponding to the $b \to c\ell^- \bar{\nu}_\ell$ transitions and the exclusive channel $\overline{B^0_d} \to D^{*+}\ell^- \bar{\nu}_\ell$.
- $|V_{ub}|$: The determination of $|V_{ub}|$ is done from both inclusive and exclusive decays. Considering the inclusive $B \to X_u l \bar{\nu}$, specific phase space cuts are required to avoid the presence of significant backgrounds from $B \to X_c \ell \bar{\nu}_\ell$ decays.
- $|V_{td}|$ and $|V_{ts}|$: These CKM elements are not likely to be measurable in tree-level processes involving top quarks, thus they are determined via B-meson mixing processes and rare decays mediated by loops, as $B \to X_s \gamma$.
- $|V_{tb}|$: Its value is determined by decays of the top quark or by measuring the cross section for single top quark production.

The three angles α, β, and γ are related to the CKM matrix elements and can be expressed in the following way

$$\begin{aligned}\beta = \phi_1 = arg(-\frac{V_{cd}V_{cb}^*}{V_{td}V_{tb}^*}),\\ \alpha = \phi_2 = arg(-\frac{V_{td}V_{tb}^*}{V_{ud}V_{ub}^*}),\\ \gamma = \phi_3 = arg(-\frac{V_{ud}V_{ub}^*}{V_{cd}V_{cb}^*}).\end{aligned} \tag{32}$$

Since CP violation involves phases of CKM elements, generally the phase values and the $\bar{\rho}$, $\bar{\eta}$ parameters are determined using CP-violating observables of decays, as $b \to \bar{c}cs$ decays to CP eigenstates [11].

1.4.5 Global fit in the Standard Model

Unitarity verification Using the independently measured elements of the CKM matrix, it's possible to verify the unitarity of the matrix, which is a key property in the Standard Model of particle physics. The square of the CKM matrix elements V_{ij} (where $i, j = 1, 2, 3$) should sum up to one in each row and column of the matrix. Hereafter, we report the results [11] obtained in rows and columns not involving the τ quark. One obtains:

- First row unitarity: $|V_{ud}|^2 + |V_{us}|^2 + |V_{ub}|^2 = 0.9984 \pm 0.0007$
- Second row unitarity: $|V_{cd}|^2 + |V_{cs}|^2 + |V_{cb}|^2 = 1.001 \pm 0.0012$
- First column unitarity: $|V_{ud}|^2 + |V_{cd}|^2 + |V_{td}|^2 = 0.9971 \pm 0.0020$

- Second column unitarity: $|V_{us}|^2 + |V_{cs}|^2 + |V_{ts}|^2 = 1.003 \pm 0.0012$

In addition, the sum of the three angles of the unitarity triangle is consistent with the SM expectation, being: $\alpha + \beta + \gamma = (172 \pm 5)^\circ$ [11].

Global fit Although the possibility to directly determine the CKM matrix elements with the methods above listed, the most precise values are obtained through a global fit to all available measurements, imposing the constraints of the Standard Model (*i.e.* unitarity for three generations). This fit also relies on theoretical predictions for hadronic matrix elements, that can introduce significant uncertainties [11].

There are several techniques used to combine the experimental data. For instance, the CKMfitter collaboration [24, 25] employs a frequentist approach, while the UTfit collaboration [26, 27] uses a Bayesian method. In any case, both collaborations yield compatible results, that are reported using the Wolfenstein parameterization in Tab. 1.

Method	CKMfitter	UTfit
λ	0.22501 ± 0.00068	0.22497 ± 0.00070
A	$0.826^{+0.016}_{-0.015}$	0.839 ± 0.0011
$\bar{\rho}$	0.1591 ± 0.0094	0.1581 ± 0.0092
$\bar{\eta}$	$0.3523^{+0.0073}_{-0.0071}$	0.3548 ± 0.0072

Table 1: *Values of the CKM matrix parameters in the Wolfenstein parameterization, as obtained from global fits.*

The parameters expressed according to the standard parameterization read

$$\begin{aligned} \sin\theta_{12} &= 0.22501 \pm 0.00068, & \sin\theta_{13} &= 0.003732^{+0.000090}_{-0.000085}, \\ \sin\theta_{23} &= 0.04183^{+0.00079}_{-0.00069}, & \delta &= 1.147 \pm 0.026. \end{aligned}$$

The fit results for the magnitudes of all 9 CKM elements are reported below [11]

$$|V_{CKM}| = \begin{pmatrix} 0.97435 \pm 0.00016 & 0.22501 \pm 0.00068 & 0.003732^{+0.000090}_{-0.000085} \\ 0.22487 \pm 0.00068 & 0.97349 \pm 0.00016 & 0.04183^{+0.00079}_{-0.00069} \\ 0.00858^{+0.00019}_{-0.00017} & 0.04111^{+0.00077}_{-0.00068} & 0.999118^{+0.000029}_{-0.000034} \end{pmatrix}, \tag{33}$$

while the Jarlskog invariant value is $J = (3.12^{+0.13}_{-0.12}) \times 10^{-5}$.

Finally, in Fig. 3 one can see the constraints on the $\bar{\rho}$, $\bar{\eta}$ plane from various measurements, and the global fit result.

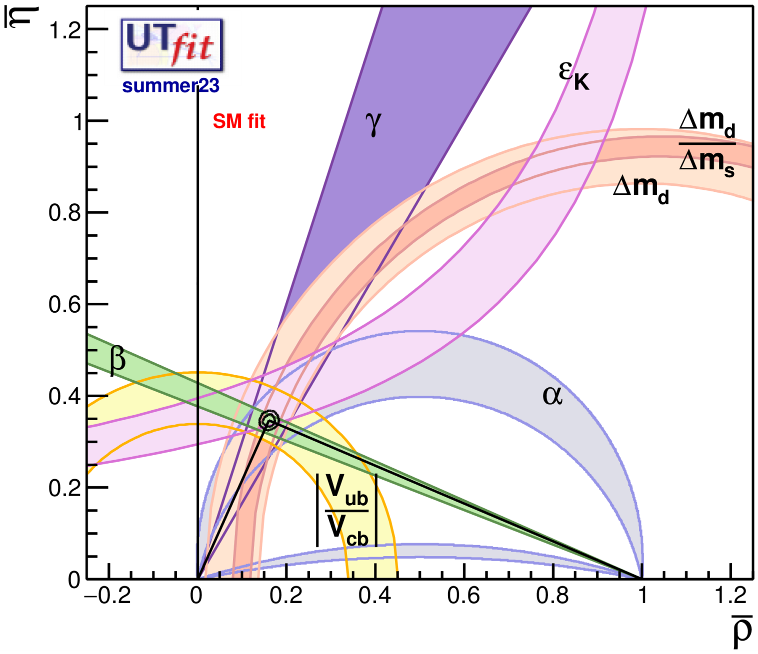

Figure 3: *Unitarity triangle and constraints on the* $\bar{\rho}$, $\bar{\eta}$ *plane [28].*

1.5 Flavor Changing Neutral Currents

Flavour-changing neutral-current processes are governed by the GIM mechanism [12], which guarantees their natural suppression, as it is observed experimentally and explained in Sec. 1.2.2. Consequently, no FCNC processes occur at the tree-level and the leading contributions result from one-loop diagrams: penguin and box diagrams, as shown in Fig. 4 [29]. Examples of these processes are particle-antiparticle mixing, some rare decays, CP-violating decays and others. Consequently, processes involving FCNC transitions constitute powerful probes for physics beyond the Standard Model.

However, it should be noted that strong interaction effects must be taken into account when calculating branching ratios for hadron decays. The effective QCD coupling at short distance is small and the gluonic contributions at scales $\mathcal{O}(M_W, M_Z, m_t)$ can be calculated within the perturbative framework. On the other hand, since mesons are $q\bar{q}$ bound states, we need to consider also QCD at long distance, which relies on non-perturbative methods [29].

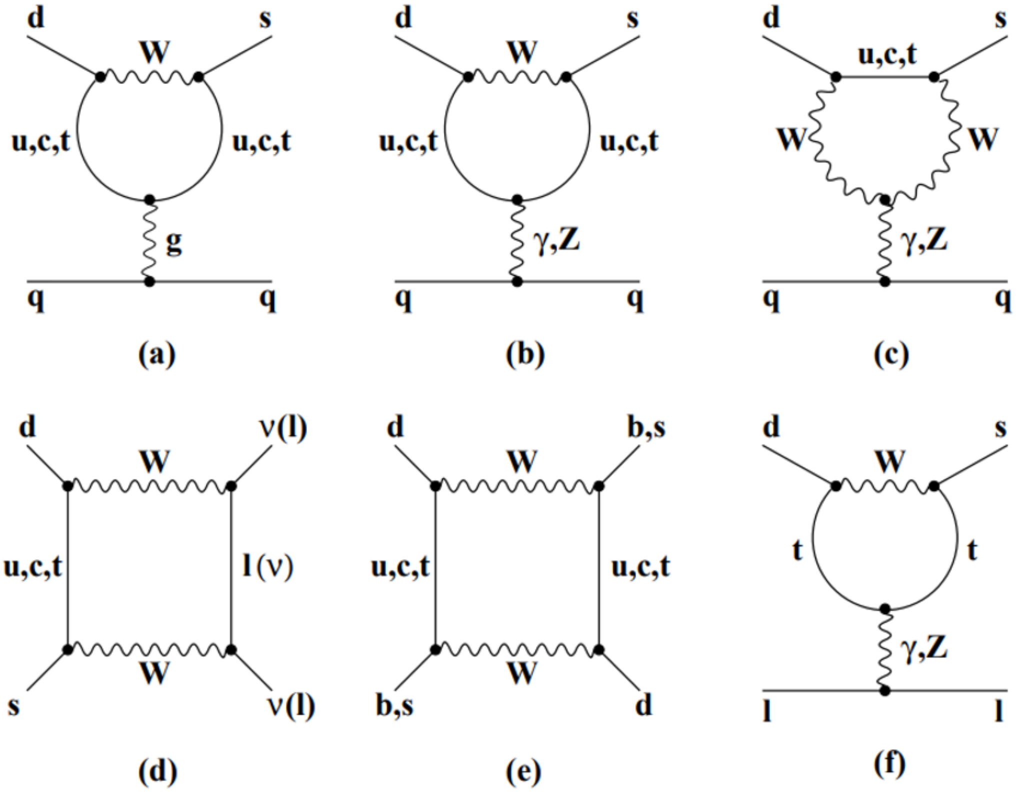

Figure 4: *Typical Penguin and Box Diagrams for FCNC processes [29].*

1.6 Rare charm decays

Rare charm decays offer a unique possibility to investigate flavour-changing neutral-currents in the up-sector within the Standard Model and beyond. Indeed, rare decays of flavored mesons containing s, c or b quarks are sensitive to heavy degrees of freedom at mass scales higher than that currently available at present colliders and new or unknown particles could modify the rate of a given process, change the angular distributions of the decay products or constitute new sources of CP violation [30]. In this context, rare charm decays, which are sensitive to $|\Delta c| = |\Delta u| = 1$ transitions, play a crucial role even though for long time they were considered less promising due to the presence of regions dominated by resonant contributions, that are difficult to describe in a consistent theoretical framework.

Analyzing deeper the theoretical framework of these decays, the leading contribution to $|\Delta c| = |\Delta u| = 1$ appears at 1-loop level, a possible transition of which is displayed in Fig. 5.

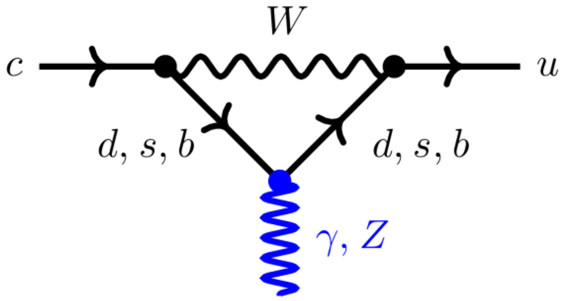

Figure 5: *SM electroweak penguin topology contributing to* $|c| = |u| = 1$ *transitions [30].*

These are called short-distance contributions and arise from quantum effects involving virtual particles, primarily through electroweak penguin or box topologies. The amplitude of this diagram can be expressed as a weighted sum over the internal quark contribution, that reads [30]

$$\mathcal{A}(c \to u) = \sum_{i=d,s,b} V_{ci}^* V_{ui} f_i. \tag{34}$$

The term $V_{ci}^* V_{ui}$, sometimes referred to as λ_i, accounts for the dependence on the CKM matrix and thus includes the CP violating phenomena. Each quark's contribution is suppressed by a function $f_i \equiv f(x_i) \sim \frac{x_i}{(4\pi)^2}$ which parametrizes the quantum effects via the variable $x_i \equiv \frac{m_i^2}{M_W^2}$, where m_i are the masses of the down-type quarks and m_W is the mass of the W boson [30]. Since m_d and m_s are much lighter than m_W, their contributions are negligible compared to that of the b quark.

The unitarity condition of the CKM matrix, specifically $\sum_{i=d,s,b} V_{ci}^* V_{ui} = 0$, allows to remove the dependence of the amplitude on $\lambda_d = V_{cd}^* V_{ud}$. Thus one obtains

$$\mathcal{A}(c \to u) = \lambda_s[f_s - f_d + \xi_b(f_b - f_d)], \tag{35}$$

where $\xi_b \equiv \lambda_b/\lambda_s$ (with $\lambda_b = V_{cb}^* V_{ub}$ and $\lambda_s = V_{cs}^* V_{us}$). The relation shown in Eq. (35) emphasizes that branching fractions for rare $c \to u$ transitions are suppressed via the GIM mechanism (first term) and CP asymmetries are CKM-suppressed through $\xi_b \sim 10^{-3}$ (second term) [30]. This makes these channels particularly promising for indirect New Physics searches.

In these processes, as already stated, both short-distance and long-distance contributions occur. Thus, in the most general form the rare $|\Delta c| = |\Delta u| = 1$ transitions are described by an effective Hamiltonian which helps in dividing these 2 types of contribution. The effective Hamiltonian obtained with the Operator Product Expansion (OPE) [31] is reported in Eq. (36) [30]. This approach allows the factorization between the matrix elements of local operators $\mathcal{O}_i$, that represent the long-distance physics, and the Wilson coefficients $\mathcal{C}_i$, that encodes the short-distance effects.

$$\mathcal{H}_{eff} = -\frac{4G_F}{\sqrt{2}}\frac{\alpha_e}{4\pi}\left[\sum_{i\neq T,T5}(\mathcal{C}_i(\mu)\mathcal{O}_i(\mu) + \mathcal{C}'_i(\mu)\mathcal{O}'_i(\mu)) + \sum_{i=T,T5}\mathcal{C}_i(\mu)\mathcal{O}_i(\mu)\right] \tag{36}$$

where

$$\begin{aligned}
\mathcal{O}_7 &= \frac{m_c}{e}\left(\bar{u}_L\sigma_{\mu\nu}c_R\right)F^{\mu\nu}, &\qquad \mathcal{O}_8 &= \frac{m_c g_s}{e^2}\left(\bar{u}_L\sigma_{\mu\nu}T^a c_R\right)G_a^{\mu\nu},\\
\mathcal{O}_9 &= \left(\bar{u}_L\gamma_\mu c_L\right)\left(\bar{\ell}\gamma^\mu\ell\right), &\qquad \mathcal{O}_{10} &= \left(\bar{u}_L\gamma_\mu c_L\right)\left(\bar{\ell}\gamma^\mu\gamma_5\ell\right),\\
\mathcal{O}_{S(P)} &= \left(\bar{u}_L c_R\right)\left(\bar{\ell}(\gamma_5)\ell\right), &\qquad \mathcal{O}_{T(T5)} &= \frac{1}{2}\left(\bar{u}\sigma_{\mu\nu}c\right)\left(\bar{\ell}\sigma^{\mu\nu}(\gamma_5)\ell\right).
\end{aligned} \tag{37}$$

In Eq. (37), one can observe local dimension-six operators relevant for this description. The operators T and $T5$ are respectively the tensor operator and the chiral tensor operator. They are kept separately in the sum since they do not have a chiral version as usually defined by switching $L \leftrightarrow R$. On the other hand, the other operators present both their chiral versions: $\mathcal{O}_i$ and $\mathcal{O}'_i$. Moreover, $q_{L,R} = \frac{1}{2}(1 \mp \gamma_5)q$ are chiral quark fields, T^a the generator for $SU(3)_C$ and g_s is the strong coupling. Finally, $\sigma^{\mu\nu} = \frac{i}{2}[\gamma^\mu, \gamma^\nu]$ and $F^{\mu\nu}, G_a^{\mu\nu}$ ($a = 1, ..., 8$) are the electromagnetic and gluonic field strength tensor, respectively [30].

The expansion depends on the renormalization scale μ. The operators in Eq. (37) are constructed with light fields (masses below $\mu < m_b$), while fields with masses above the normalization scale are removed as dynamical degrees of freedom and their effects are encoded in the Wilson coefficients. Hence, if experimental deviations are observed for these coefficients from the SM prediction, it is an indication for BSM physics [30].

The calculation of the Wilson coefficients occurs in a two-step matching: firstly, at the high scale M_W and subsequently when the bottom-threshold is crossed (going down to the charm mass). Therefore, also the bottom mass m_b has to be integrated out [32]. In the SM, the transitions of interest are driven via the exchange of a W boson, as in Fig. 6(a). At high energies but below the electroweak symmetry breaking, QCD corrections are small and the W boson can be integrated out, Fig. 6(b). As the energy scale decreases below m_W, gluonic corrections from QCD become increasingly relevant and must be taken into account, Fig. 6(c). Finally, at $\mu > m_b$, light quarks can be treated as massless, resulting in a fully effective GIM mechanism that cancels out penguin contributions. However, integrating out the bottom quark introduces effective penguin-type operators, as shown in Fig. 6(d) [30].

To fully assess the decay amplitude of rare $c \to u\ell^+\ell^-$ transitions, the determination of hadronic matrix elements $\mathcal{O}_i(\mu)$, that encode the non-perturbative dynamics at low energies, is also required. The evaluation of these matrix elements is non-trivial, since QCD becomes non-perturbative at energies around the charm mass ($\Lambda_{QCD} \sim$

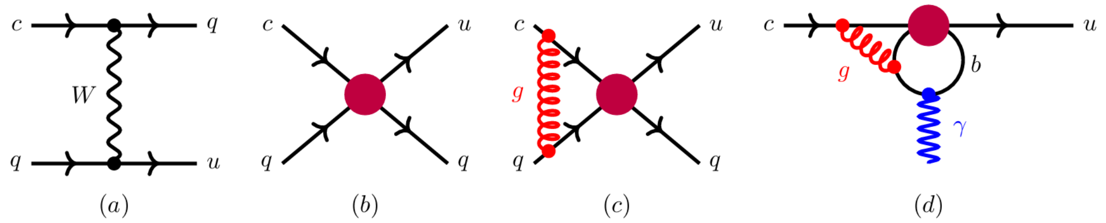

Figure 6: *Representation of contributions to $\Delta c = \Delta u = 1$ transitions at different energy scales [30].*

m_c) [30]. Form factors (FFs) arise when we parametrize the hadronic matrix elements $\langle h_c|O_i|F\ell^+\ell^-\rangle$, where h_c is a charm hadron and F the finale state. They cannot be calculated perturbatively, and must be determined using alternative methods as lattice QCD, experimental fits and others. In addition, in many charm decays the dilepton pair can be produced via intermediate resonances. These resonances are modeled using Breit-Wigner distributions and their impact is usually encoded into modified Wilson coefficients, that are function of q^2 and in turn depends on parameters as the mass and the width of the resonance m_M and Γ_M, and the complex amplitude and strong phase of each resonance a_M and δ_M.

1.7 $D^0 \to \pi^-\pi^+e^-e^+$ and $D^0 \to K^-K^+e^-e^+$ decays

Rare semi-leptonic four-bodies charm decays of the form $D^0 \to h^-h^+e^-e^+$, where h^-h^+ are a pair of two oppositely charged hadrons, specifically kaons or pions, can proceed via both long-distance (LD) and short-distance (SD) interactions. The relevant Feynman diagrams are shown in Fig. 7.

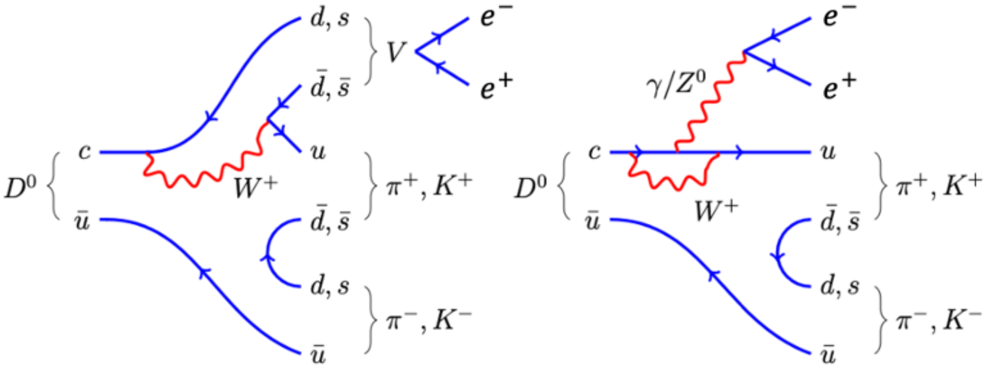

Figure 7: *Feynman diagrams of $D^0 \to \pi^+\pi^-e^+e^-$ and $D^0 \to K^-K^+e^+e^-$ processes. The LD diagram (left) and the electroweak penguin transition (right) are shown [33].*

LD interactions are mediated by meson vector or scalar resonances ($D \to XY(\to \ell^+\ell^-)$) and usually dominate over the SD ones, spanning the entire dilepton-mass spectrum. On the contrary, SD proceed via FCNC transitions and thus are highly suppressed in the Standard Model by the GIM mechanism. Consequently, the expected total branching ratios are $\mathcal{B}(D^0 \to K^-K^+e^-e^+) \sim 10^{-7}$ and $\mathcal{B}(D^0 \to \pi^-\pi^+e^-e^+) \sim 10^{-6}$, respectively for the kaon channel and for the pion channel. However, SD contributions are expected to play a role only at the level of $\sim 10^{-9}$ [30]. Therefore, any observed deviation from these SM expectations may be indicative of New Physics, potentially arising from non-SM amplitudes interfering with the decay process [34]. However, accessing the SD contributions of interest requires both large data sets and the use of complementary observables that are sensitive to short- and long-distance processes [35]. In addition to their sensitivity to beyond standard model physics, these decays provide a valuable test of lepton flavor universality (LFU), by comparing the decay rates of final states containing electrons with those of the corresponding muonic modes. In fact, the LHCb experiment has successfully observed for the first time the rare muonic $D^0 \to h^+h^-\mu^+\mu^-$ decays [36], measuring their BFs and performing the CP and angular analysis [37].

The final goal of the analysis is the first observation and the branching fraction measurement of the kaon channel ($D^0 \to K^-K^+e^-e^+$) and a more precise measurement of the branching ratio of the pion channel ($D^0 \to \pi^-\pi^+e^-e^+$). This procedure relies on comparison with the normalization channel $D^0 \to K^-\pi^+e^-e^+$, which is a Cabibbo-favored decay, as explained in detail earlier in this chapter.

1.8 Lepton Flavour Universality

Lepton flavour universality, also referred to as LFU, is a fundamental principle of the Standard Model, stating that the electroweak interactions of charged leptons (e, μ, τ) are identical, up to small corrections due to their mass differences. This means that in the SM, the coupling constants of the gauge bosons $(W^\pm, Z^0, \gamma)$ to the different lepton flavours are universal, implying the equality of decay rates of electroweak processes involving different lepton generations. Being an accidental symmetry of the SM, it can be examined to challenge its validity and any departure from this identity would be a clear sign that virtual NP particles contribute to SM decays. Experimental measurements used as precise tests of LFU are for instance those concerning the decays at the Z pole, $Z \to \ell^+\ell^-$, where $\ell = e, \mu, \tau$, whose values for the ratio of the leptonic partial-widths are reported in Eq. (38) [38], or decays as $W^\pm \to \ell^\pm\nu_\ell$, with results in Eq. (39) [39]

$$\begin{aligned} \frac{\Gamma_{\mu\mu}}{\Gamma_{ee}} &= \frac{\mathcal{B}(Z \to \mu^-\mu^+)}{\mathcal{B}(Z \to e^-e^+)} = 1.0009 \pm 0.0028, \\ \frac{\Gamma_{\tau\tau}}{\Gamma_{ee}} &= \frac{\mathcal{B}(Z \to \tau^+\tau^-)}{\mathcal{B}(Z \to e^-e^+)} = 1.0019 \pm 0.0032, \end{aligned} \tag{38}$$

$$\frac{\Gamma_{\tau\tau}}{\Gamma_{\mu\mu}} = \frac{\mathcal{B}(W \to \tau\nu_{\tau})}{\mathcal{B}(W \to \mu^{-}\nu_{\mu})} = 0.992 \pm 0.013. \tag{39}$$

These values are in agreement with the hypothesis of LFU (assuming massless leptons).

Beyond the above cited test, LHCb has recently performed measurements also in tree-level and loop level transitions involving hadrons, as $b \to c\ell^{-}\overline{\nu_{\ell}}$ and $b \to s\ell^{+}\ell^{-}$. As an example, here we report one of the latest result using b-hadrons decays into c-mesons [40]

$$R(D^{(*)}) = \frac{\mathcal{B}(B \to D^{(*)+}\tau^{-}\overline{\nu_{\tau}})}{\mathcal{B}(B \to D^{(*)+}\mu^{-}\overline{\nu_{\mu}})} \tag{40}$$

The results are consistent with the SM prediction and reads

$$\begin{aligned} R(D^{+}) &= 0.249 \pm 0.043 \pm 0.047, \\ R(D^{*+}) &= 0.402 \pm 0.081 \pm 0.085. \end{aligned} \tag{41}$$

Rare flavour-changing neutral current processes, as $D^0 \to h^{+}h^{-}\ell^{+}\ell^{-}$, described in the previous Section, allow for the investigation of the evidence for lepton flavour universality violation, specifically via the analysis of observables as the ratio between decays involving muons and electrons in the final state.

2 The LHCb experiment

2.1 The Large Hadron Collider at CERN

The CERN (European Organization for Nuclear Research) is the world's largest laboratory for particle physics, founded in 1954 and located on the border between Switzerland and France, near Geneva, where its biggest accelerator, the Large Hadron Collider (LHC), is placed [41]. The LHC is a two-ring-superconducting-hadron accelerator and collider installed inside the 26.7 km long tunnel which was previously hosting the Large Electron Positron collider (LEP), about 100 m underground with the lowest point at ~ 175 m. It is located under the Meyrin (Geneva) Swiss - French border and was built with the aim of discovering the Higgs particle and to study rare events with center of mass collision energies up to 14 TeV [42].

The LHC project has no precedent in terms of energy, luminosity, size and complexity of the experiments and human resources. Indeed, its design energy frontier is at $\sqrt{s} = 14$ TeV with an unprecedented luminosity of $\mathcal{L} \sim 10^{34}$ cm^{-2}s^{-1}. In practice, the highest energy achieved so far has been 13.6 TeV with the ongoing Run 3. The LHC is a particle-particle collider, with 2 rings with counter rotating beams. The original LEP tunnel hosted 8 points, flanked by long straight sections for RF cavities to compensate the high synchrotron radiation losses [43]. For the LHC the main limitation is not related to the energy loss per turn (which is ~ 7 keV, thus not relevant for protons), but is the bending power, indeed being the effective bending radius of ~ 2.7 km, the nominal LHC requires a magnetic field of 8.5 T.

To produce such an high B field, there are a total of 1232 dipoles 15 m long that guide the beams and 392 quadrupoles $5 - 7$ m long to focus the beams. Proton beams circulate along the LHC ring inside vacuum in two adjacent rings with counter-rotating beams in order to be able to collide protons in four crossing points where the major experiments are located:

- 2 general purpose detectors: ATLAS (A Toroidal LHC ApparatuS) and CMS (Compact Muon Solenoid);
- LHCb (Large Hadron Collider beauty), a detector optimized for precision studies of decays and CP violation measurements in hadrons containing b and c quarks;
- ALICE (A Large Ion Collider Experiment), designed to study the quark-gluon plasma with heavy ion collisions.

At the interaction points, the two beams are brought into collision using special X-shaped beam pipes, with a crossing angle of approximately $1.5°$.

The high instantaneous luminosity of the LHC enables the study of rare processes that occur with very small cross sections. Indeed, the number of events per second generated in the collisions (*i.e.* the rate R) depends on the machine luminosity and on the cross section of the process under study, Eq. (42)

$$R_{events} = \mathcal{L}\sigma_{process}. \tag{42}$$

The machine luminosity depends only on the beam parameters and can be written as

$$\mathcal{L} = \frac{N_b^2 n_b f_{rev}\gamma_r}{4\pi\varepsilon_n\beta^*}F \tag{43}$$

where N_b is the number of particles per bunch, n_b the number of bunches per beam, f_{rev} the revolution frequency, γ_r the relativistic gamma factor, ε_n the normalized transverse beam emittance, β^* the beta function at the collision point, and F the geometric luminosity reduction factor due to the crossing angle at the interaction point (IP) [42].

At LHCb, in proton-proton collision at $\sqrt{s} = 13$ TeV and in the range $0 < p_T < 8$ GeV/c and $2 < y < 4.5$, the cross-section for production of a charm meson is $2369 \pm 192\,\mu$b [44].

2.2 The LHCb detector

The LHCb experiment is dedicated to the study of b- and c-physics and it aims at searching for physics beyond the Standard Model via high-precision measurements of CP-violating observables and rare decays of beauty and charm-flavored hadrons [45]. It was primarily designed for precision measurements in heavy-flavor physics, but it has demonstrated excellent capabilities in many other domains, such as electroweak physics, heavy ion physics and fixed target experiments.

The LHCb detector operated between 2010 to 2018 during the LHC Run 1 (2010-2012) and Run 2 (2015-2018) data-taking period, collecting a total of 9 fb^{-1} of proton proton (pp) data, about 30 nb^{-1} of lead-lead and p-lead collisions and about 200 nb^{-1} of fixed target data [46]. The original LHCb design allowed to take data for most of Run 1 and Run 2 at the instantaneous luminosity of $\mathcal{L} = 4 \times 10^{32}$ cm^{-2}s^{-1}, while it was originally designed for half of the value. Although this dataset is one of the largest ever collected concerning b and c hadron decays, the precision on many of key flavour physics observables remains still statistically limited thus requiring larger datasets to probe the SM at the level of precision achieved by theoretical calculations.

Consequently, the LHCb upgrade has been designed to run at a nominal instantaneous luminosity $\mathcal{L} = 2 \times 10^{33}$ cm^{-2}s^{-1} and collect events at the LHC crossing rate of 40 MHz [46].

LHCb detector after Upgrade I The LHCb detector is a single arm spectrometer characterized by a forward detection geometry, due to the fact that $b-$ and $\bar{b}-$hadrons are mainly produced in the same forward or backward cone at high energies [45]. It covers the pseudorapidity range $2 < \eta < 5$, which allows for the study of particles produced at small angles with respect to the beam pipe. This structure is particularly effective since heavy-hadrons tend to be produced in the forward region. The LHCb experiment is located at interaction point number 8 on the LHC ring. The layout of the detector is shown in Fig. 8 [46].

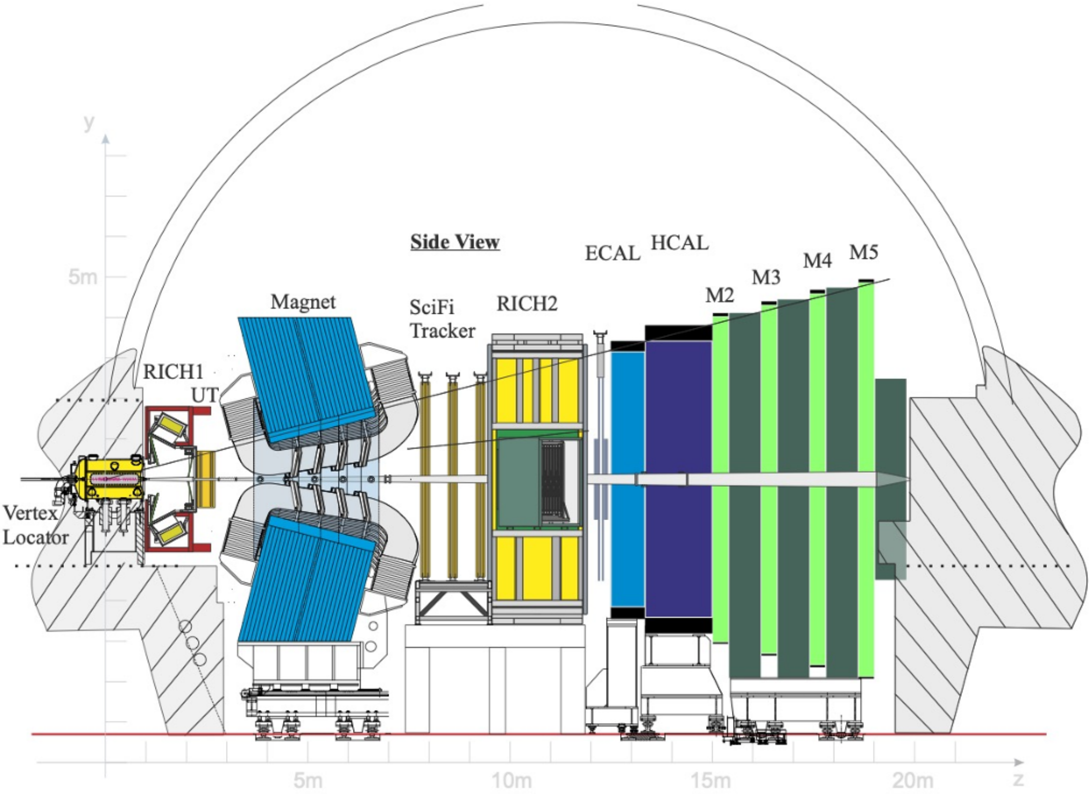

Figure 8: *Side view of the LHCb detector after the Upgrade I. The coordinate system has the origin in the* pp *interaction point, the* z *axis along the beam pointing the muon system, the* y *axis pointing vertically upward and the* x *axis defining a right handed system.*

2.3 Tracking and Vertexing

The particle tracking system was upgraded to comply with the 40 MHz read-out architecture and the increase in instantaneous luminosity. It is now composed of 3 subsystems:

- the VErtex LOcator (VELO), an array of pixel silicon detectors;

- the silicon-strip upstream tracker (UT);
- three scintillating fibre tracker (SciFi Tracker).

These tracking stations, combined with the magnetic field, allow particles' trajectory reconstruction and the determination of their momentum.

2.3.1 VErtex LOcator

The VELO is the closest sub-detector to the beam pipe, thus its primary aim is to detect tracks of ionizing particles coming from the beam collision region in order to measure the location of both interaction vertices and displaced decay vertices. Moreover, tracks reconstructed by VELO represent essential input information for the primary vertex and track reconstruction algorithms and for event selection. The VELO is made of pixel hybrid silicon detectors, arranged into modules and cooled by a microchannel cooler. The characteristics of the upgraded VELO are reported in Tab. 2 [46].

RF box inner radius (minimum thickness)	3.5 mm (150 μm)
Inner radius of active silicon detector	5.1 mm
Total fluence (silicon tip) [n_{eq}/cm^2]	$\sim 8 \times 10^{15}$
Sensor segmentation	square pixels
Total active area of Si detectors	0.12 m^2
Pitch (strip or pixel)	55 μm
Technology	n-on-p
Number of modules	52
Total number of channels	41 million
Readout rate [MHz]	40, zero suppressed
Whole-VELO data rate	$\sim$ 2 Tbit/s
Total power dissipation (in vacuum)	$\sim$ 2 kW

Table 2: *VELO detector parameters after Upgrade I.*

The layout of the VELO detector is shown in Fig. 9. It consists of two movable halves, each composed of 26 L-shaped silicon pixel detector modules, as shown in Fig. 10. This structure is necessary to keep the halves ~ 6 cm apart during the injection and beam adjustments to prevent damage to the detector's sensitive components. Each of the 52 modules is made by 12 VeloPix read-out ASICs. Each ASIC has a pixel array of 256×256. This structure implies a fine granularity which ensures a high spatial resolution. The detector is operated in vacuum, separated from the LHC vacuum by a thin aluminum alloy RF (Radio Frequency) foil to protect the front-end electronics [47].

A distinctive signature of b- and c-hadron decays at LHCb is due to tracks originating from secondary vertices that exhibit a large impact parameter[1] relative to all primary vertices. The impact parameter resolution σ_{IP} for the VELO [48] is a function of the transverse momentum p_T, the distance before the second measurement r_1, the distances from the point to the first and second measurements, Δ_i, and the position uncertainties σ_i, $i = 1, 2$:

$$\sigma_{\text{IP}}^2 \approx \underbrace{\left(\frac{r_1}{p_T\,[\text{GeV}/c]}\right)^2 \left(0.0136\,\text{GeV}/c\sqrt{\frac{x}{X_0}}\left(1 + 0.038\ln\frac{x}{X_0}\right)\right)^2}_{\text{multiple scattering}} + \underbrace{\frac{\Delta_2^2\sigma_1^2 + \Delta_1^2\sigma_2^2}{\Delta_{12}^2}}_{\text{extrapolation}} \tag{44}$$

To enhance vertex resolution, several design optimizations were implemented such as the pixel geometry, a minimization of the material traversed by the tracks, a shorter distance between the active silicon area and the interaction point, and an increased lever arm between measurement points. These improvements imply expected VELO performance significantly enhanced with respect to the original configuration. Indeed, the VELO hit efficiency is greater than 99% [49].

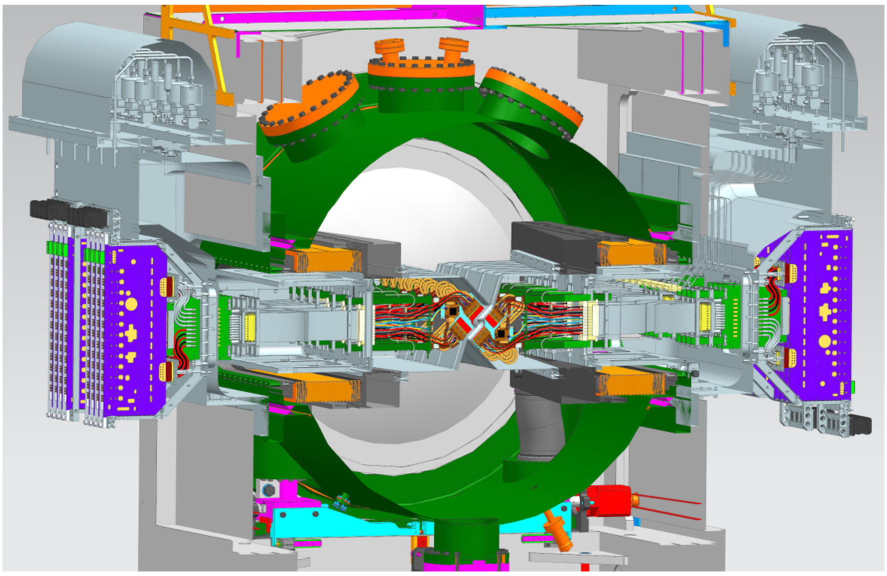

Figure 9: *A CAD model of the layout of the VELO Upgrade detector [47].*

---

[1] The impact parameter is defined as the shortest distance between a particle's reconstructed track and the primary vertex.

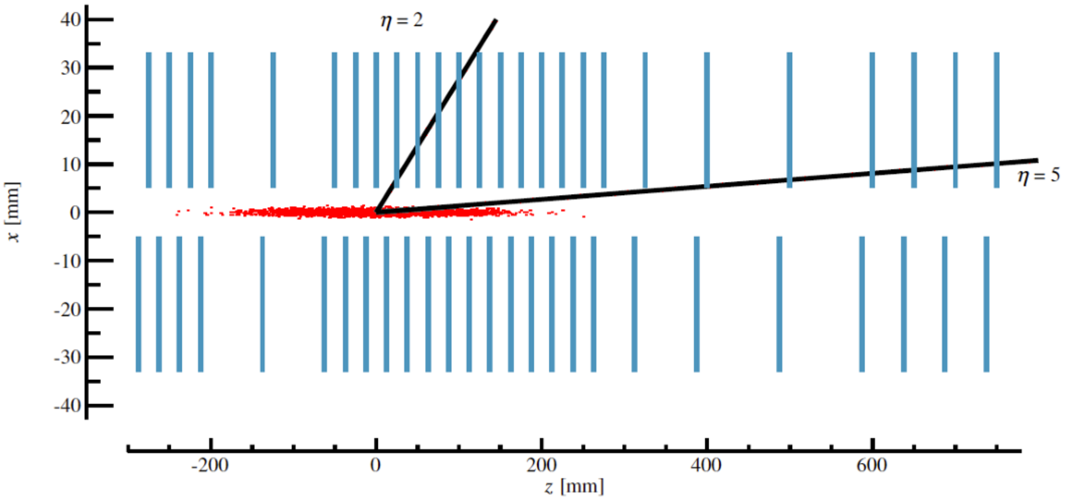

Figure 10: *Schematic cross-section at $y = 0$ with an illustration of the z-extent of the luminous region and the nominal LHCb acceptance [47].*

2.3.2 Upstream Tracker

The Upstream Tracker [46] is the new silicon strip tracking sub-detector, placed between the RICH1 detector and the dipole magnet. It is used for charged-particle tracking and it is an essential component for the first processing algorithm in the software trigger. Indeed, the UT hits in combination with the VELO tracks allow a first determination of the track momentum p with moderate precision ($\sim 15\%$). Moreover, tracks with $p_T > 0.2$ GeV are processed and an estimate of momentum and charge is performed to speed up the matching with the SciFi Tracker results. UT hit information also reduces the rate of fake tracks due to VELO and SciFi segments and provides measurements for long lived particles, that decay after the VELO.

To achieve all the above-cited physics goals, several requirements need to be fulfilled: no gaps in the coverage, a high hit efficiency (more than 99% of charged particles traversing the detector within the acceptance should leave hits), hit purity, the occupancy below a few percent, low material budjet and finally, it needs to be able to withstand a radiation level of the order of 1 kGy.

For the above reasons, the UT comprises 4 planes of silicon detectors organized in 2 stations. The silicon sensor are arranged on carbon fiber structures in vertical units, called staves. The first station is composed of an x-measuring layer (UTaX) and a stereo layer (UTaU), made of 16 staves each; while the second station is composed of a stereo layer (UTbV) and a vertical strips layer (UTbX), each made of 18 staves. In the central layers the strips are rotated with opposite inclination of ± 5. The sensors are arranged on both sides of the staves to obtain a vertical overlap and ensure full coverage. The layout can be observed in Fig. 11.

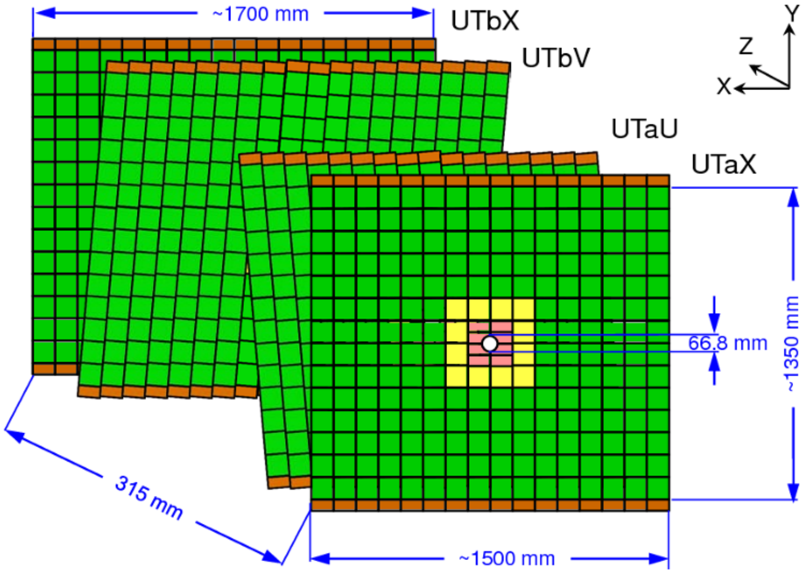

Figure 11: *Layout of the Upstream Tracker of LHCb for Run 3 [46].*

2.3.3 SciFi Tracker

The SciFi tracker is the last part of the detector which aims at particle tracking and momentum measurements. The new tracker is expected to provide a hit position resolution better than $100\ \mu$m in the magnet bending plane and single hit reconstruction efficiency better than 99%, good radiation hardness (able to maintain the desired performance over the complete lifetime of the experiment, which aims at collecting 50 fb^{-1} of integrated luminosity), while also having low material budget to limit multiple scattering and low occupancy [46].

For these reasons the choice was a tracker based on scintillating fiber technology with SiPM readout. Indeed, the detector is composed of 12 detection planes arranged in 3 stations (T1, T2 and T3) with 4 layers each in X-U-V-X configurations, that provide an acceptance ranging from ~ 20 mm from the edge of the beam pipe to ± 3186 mm and ± 2425 mm in the horizontal and vertical directions, respectively. The X layers, used to determine the deflection of the charged particle tracks caused by the magnetic field, have their fibers oriented vertically, while the inner U and V layers, have fibers rotated by $\pm 5°$.

The SciFi tracker modules consist of lightweight carbon-fibre sandwiches holding eight ~ 2.4 m long mats made of six staggered layers of scintillating fibres. Mirrors at fibres' end, located near the $y = 0$ plane, reflect light back to the readout side. Special shortened modules near $x = 0$ accommodate the beam pipe. Finally, the optical signals are detected by 128-channel SiPM arrays, bonded to 3D-printed titanium cooling bars. Initially, the light yield is 18–20 photoelectrons per perpendicular track near the mirrors. Radiation damage can reduce this by up to 40% in the most exposed regions, but still ensures > 10 photoelectrons—enough for a hit efficiency of 99% and $\sim 70\ \mu$m resolution for a single hit, suitable for tracking after the magnet [46]. The SciFi detector is represented in Fig. 12

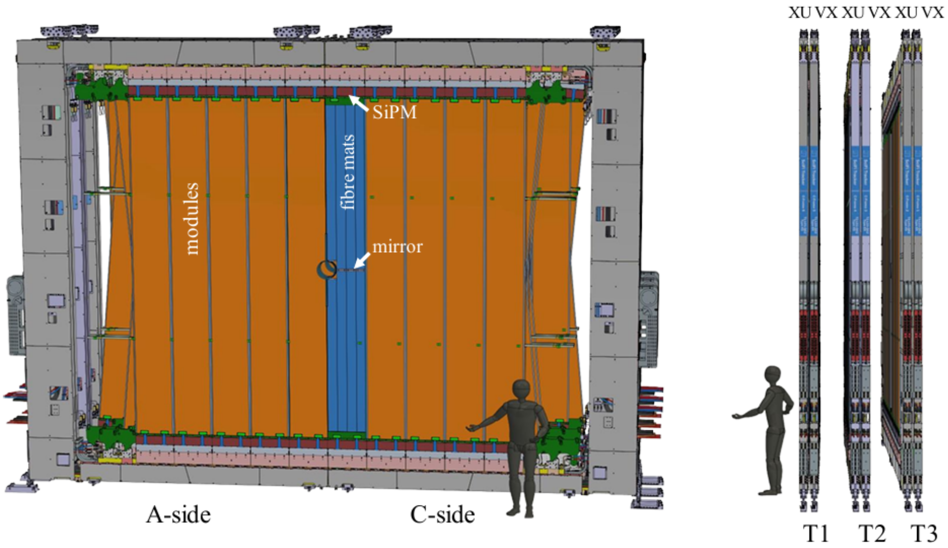

Figure 12: *Front and side views of the 3D model of the SciFi Tracker detector [46].*

2.3.4 The magnet

The bending magnet is an essential constituent of the detector since it contributes to the proper reconstruction of charged particles by bending their trajectory.

The magnet did not undergo an upgrade during the first shutdown thus it is unchanged with respect to Run 1 and Run 2 operations. It consists of 2 saddle-shaped coils in aluminum, each made of 15 mono-layer pancakes and placed mirror-symmetrically to each other in the magnet yoke, Fig. 13. The total weight of the yoke is 1500 tons and of the two coils is 54 tons [45]. It provides a vertical magnetic field with a bending power of $\int Bdl \simeq 4$ Tm, with a peak magnetic field intensity of approximately 1.1 T along the z axis, Fig. 14. The magnet polarity is regularly reversed during data taking (typically every few weeks) to collect dataset for both the configurations in order to reduce and control systematic biases related to charge-dependent detection effects [46].

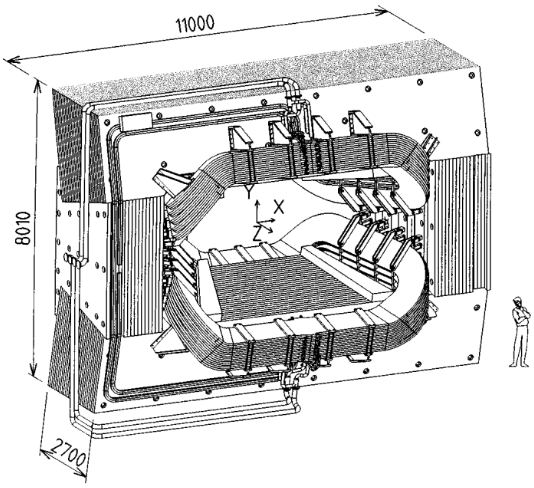

Figure 13: *Perspective view of the LHCb dipole magnet with its current and water connections. The interaction point lies behind the magnet. Length are expressed in mm [45].*

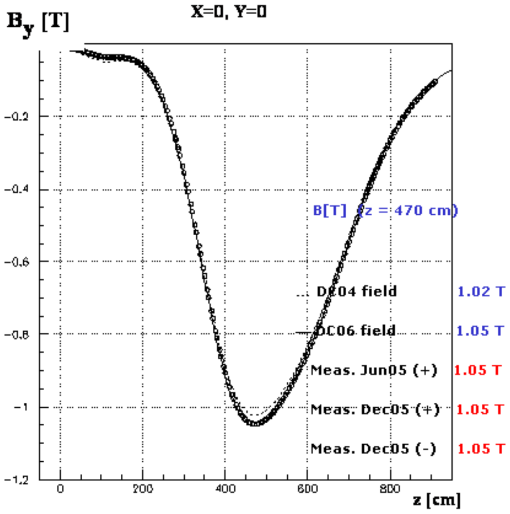

Figure 14: *Magnetic field profile along the z-axis of the LHCb experiment [50].*

2.4 Particle Identification

Particle IDentification (PID) is a fundamental requirement for the LHCb goals in order to study $b-$ and $c-$ hadron decays physics. It combines information from dedicated sub-detectors, *i.e.* the two RICH detectors, the calorimeter system, and the muon chambers, to achieve efficient separation of pions, kaons, protons, electrons, and muons over a wide momentum range.

2.4.1 Ring Imaging CHerenkov detectors

Ring Imaging CHerenkov detectors, usually referred to as RICH, are essential for the discrimination between pions, kaons and protons in LHCb. The RICH system allows to distinguish final states of identical topologies and provides also information at the HLT2 level to suppress combinatorial background. Their principle of operation is based on the detection of Cherenkov light. The Cherenkov radiation is the radiation emitted by a particle traversing a medium of refracting index n with a velocity higher than c/n, *i.e.* the velocity of the light inside that medium. It's due to the broken symmetry of the dipoles created by the polarization induced by the particle. The time variation of the dipole field emits the radiation. The Cherenkov radiation is emitted in a cone of angle θ, where $\cos\theta = \frac{1}{\beta n}$. The threshold for the emission of the Cherenkov radiation is $\beta > 1/n$.

The LHCb experiment is equipped with two RICH detectors [46], shown in Fig. 15:

- RICH1: It is located upstream of the dipole magnet and employs a C_4F_{10} gas radiator with refractive index $n = 1.0014$ for Cherenkov radiation of wavelength $\lambda = 400$ nm at STP (Standard Temperature and Pressure). It covers an angular acceptance from 25 to 300 mrad in the magnet bending plane and from 25 to 250 mrad in the vertical direction. It provides the PID in the momentum range $2.6 - 60$ GeV/c.

- RICH 2: It is located downstream the dipole magnet and uses CF_4 gas radiator with $n = 1.0005$ for $\lambda = 400$ nm at STP. It provides an angular acceptance from 15 to 120 mrad in the magnet bending plane and from 15 to 100 mrad in the vertical direction. Its design provides PID for momentum particles between 15 and 100 GeV/c.

The Cherenkov photons produced in the gaseous radiators are reflected by means of spherical and planar mirrors that focus them on the photon detector planes, creating the typical ring image. Here, the photons are detected by the multi-anode photomultiplier tubes (MaPMTs). The readout chain has been upgraded during the first shutdown to cope with the high nonuniform occupancy expected for Run3 [46].

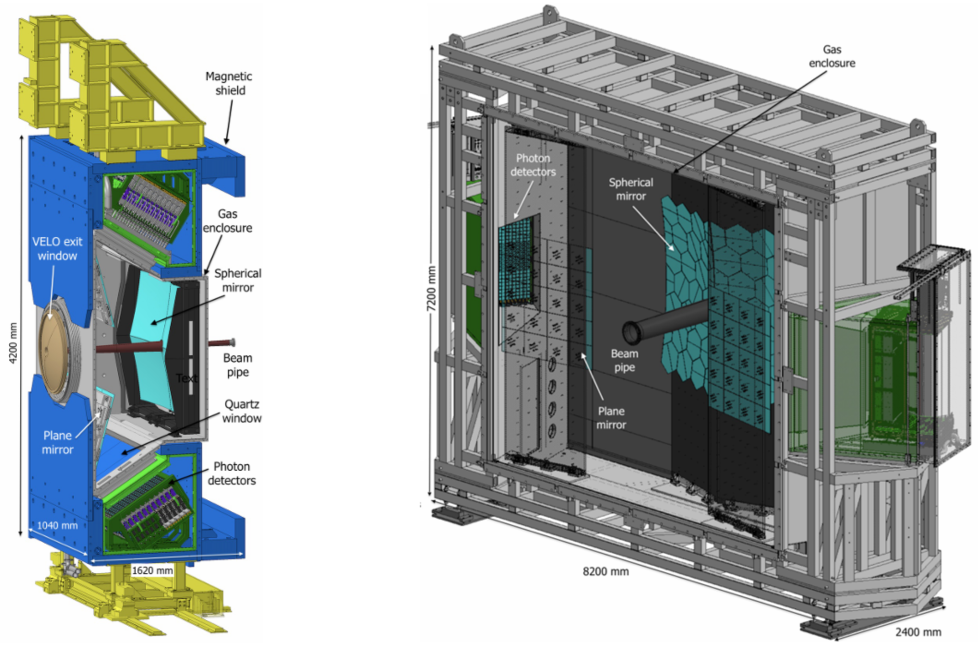

Figure 15: *Schematic view of RICH1 (left) and RICH2 (right) detectors [46].*

2.4.2 Calorimeters

The original calorimeter [45] was composed of 4 sub-modules: the Pad Detector (SPD), the PreShower (PS), the Electromagnetic calorimeter (ECAL) and the Hadronic calorimeter (HCAL). The first two in the list were removed before the first Upgrade since the introduction of the new all-software trigger reduced their role; while the ECAL and HCAL remained unchanged during the upgrade. Only the front-end (FE) and readout electronics were replaced to cope with the new readout rates.

As already stated, the calorimeter system presents the classical structure of an electromagnetic one, followed by an hadronic one. Both the calorimeters are based on the same detection principle: the scintillation light from plastic scintillator is shifted in wavelength from the fibres and transmitted to the PMTs for the collection [46].

ECAL The ECAL [46] is essential for the identification of electrons, positrons and photons, reconstructed via their electromagnetic showers. The typical radiation length of the detector materials implies that a thickness of 25 radiation lengths was necessary for the full containment of the shower. The ECAL is segmented laterally in 3 regions of increasing dimensions from the beam pipe, see Fig. 16. The ECAL cells have a *shashlik* structure with alternated layers of scintillator and lead, shown in Fig. 17. The energy resolution of a given cell has been measured with a test electron beam and is parametrized as [51]

$$\frac{\sigma(E)}{E} = \frac{(9.0 \pm 0.5)\%}{\sqrt{E}} \oplus (0.8 \pm 0.2)\% \oplus \frac{0.003}{E \sin\theta}, \tag{45}$$

where E is the particle energy in GeV, θ is the angle between the beam axis and the line from the LHCb interaction point to the center of the ECAL cell. Miscalibrations, nonlinearities and energy leakage are included via the second term of the equation. Finally, the third term accounts for electronic noise.

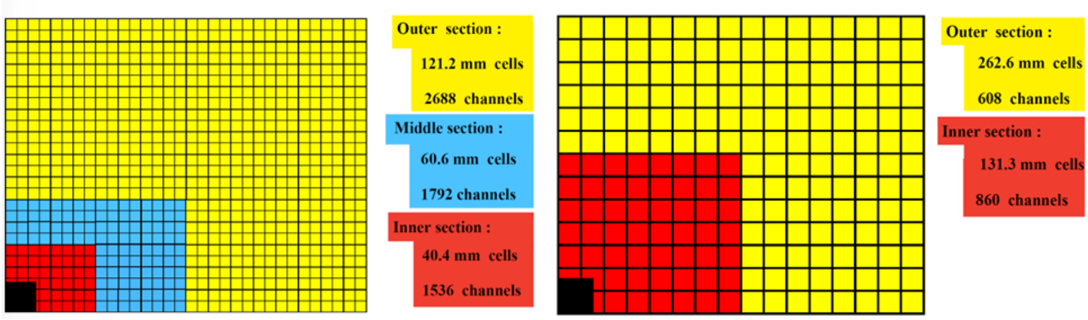

Figure 16: *Lateral segmentation of the ECAL on the left and the HCAL on the right. A quarter of the detector front face is shown [46].*

HCAL The HCAL [46] is a sampling tile calorimeter with a thickness of 5.6 interaction lengths. It is made of alternated tiles of staggered iron and plastic scintillator, set parallel to the beam axis, see Fig. 18. It is segmented in 2 regions with larger granularity with respect to the ECAL, Fig. 16. The energy resolution is parametrized as

$$\frac{\sigma(E)}{E} = \frac{(67 \pm 5)\%}{\sqrt{E}} \oplus (9 \pm 2)\%, \tag{46}$$

where E is the deposited energy in GeV.

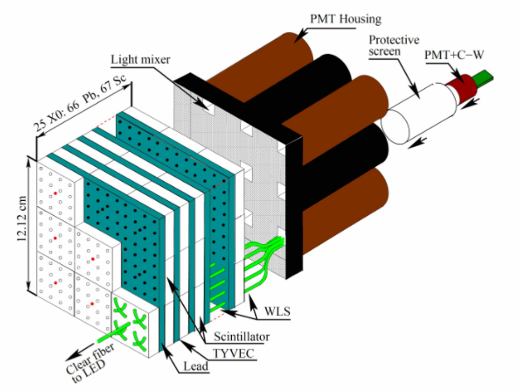

Figure 17: *Schematic of an ECAL cell [46].*

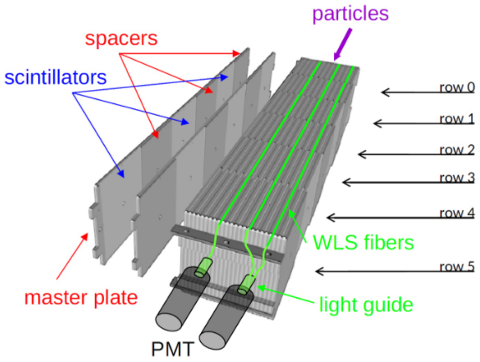

Figure 18: *Schematic of an HCAL cell [46].*

2.4.3 Muon chambers

The LHCb muon system after the first upgrade consists in four stations, M2 to M5, comprising 1104 multi-wire proportional chambers (MWPC) for a total area of 385 m^2 and located downstream of the calorimeter system [46]. To filter low energy particles, 80 cm thick iron absorbers are present. The M1 station, previously located upstream of the calorimeters [45], was removed since it was used in the hardware L0 trigger and is therefore no longer needed in the upgraded system. The old configuration is reported in Fig. 19. Each station is divided into 4 regions, R1 to R4, sketched in Fig, 20, whose area and segmentation scale moving from the central beam axis outwards to uniformly distribute the particle flux and occupancy.

2.5 Trigger

Working at high energy and luminosity results in the production of an enormous amount of data. The trigger system is designed to reduce this flow from 4 TB/s (at the nominal $\mathcal{L}$ in pp collisions) to about 10 GB/s, which can then be stored offline [46]. Achieving such a reduction is highly non-trivial. The process is sketched in Fig. 21.

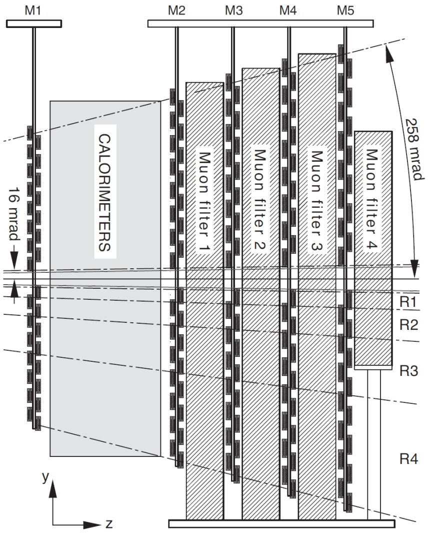

Figure 19: *Configuration of the muon stations before the first upgrade of the LHCb detector [45]. The new system maintains the same configuration of the M2 to M5 stations and removes the first one, namely M1.*

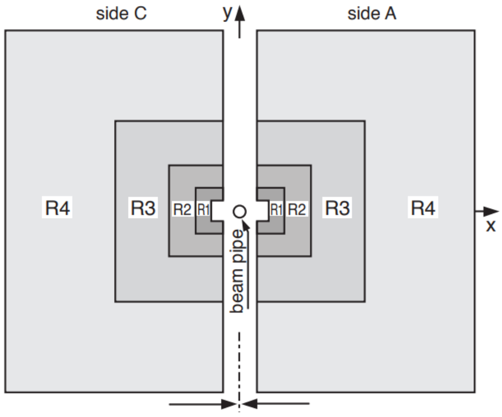

Figure 20: *The station layout with the four regions, R1–R4.*

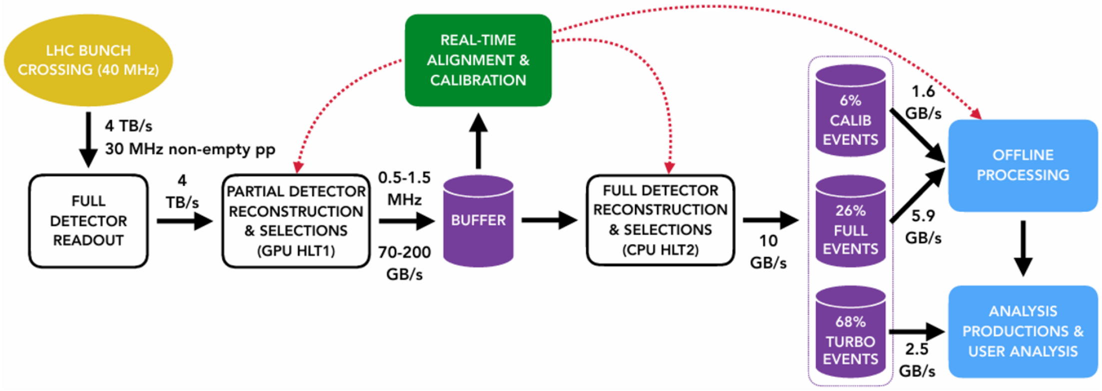

Figure 21: *LHCb data flow [52, 46].*

At LHCb, unlike in other experiments, the physics channels of interest cannot be efficiently selected using only generic signatures; instead, they require full reconstruction and identification. This strategy, known as the *real-time analysis* approach, necessitates performing offline-quality reconstruction directly within the trigger system. Consequently, the trigger is organized into two stages: HLT1 and HLT2.

It is noteworthy that the trigger underwent a fundamental upgrade during the shutdown. In Runs 1 and 2, it consisted of three levels: L0 - a hardware-based trigger - followed by HLT1 and HLT2. After the Upgrade I, the trigger is entirely software-based, which makes it possible to fully exploit the higher luminosity, especially for electronic and hadronic channels. The new trigger has already demonstrated increased efficiencies, as illustrated, for example, in Fig. 22.

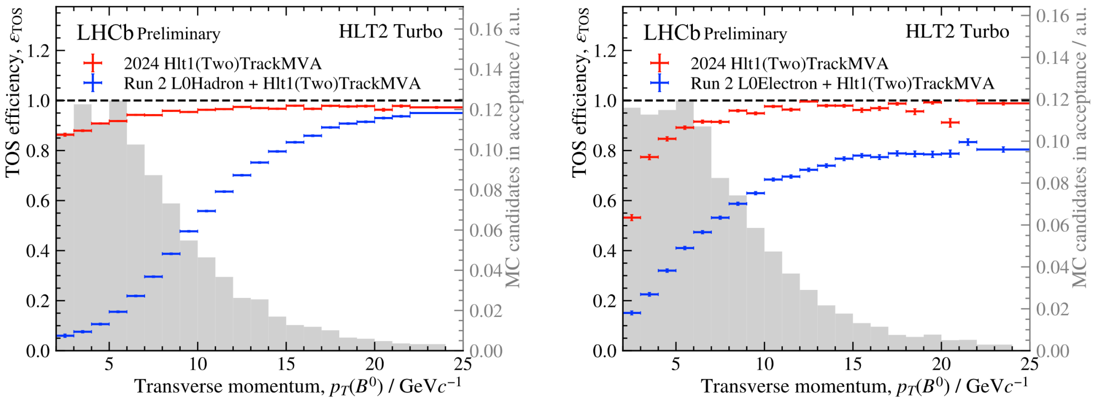

(a) $B_d \to D\pi$, where $D \to K\pi\pi$.

(b) $B_d \to J/\psi\, K^*$, $J/\psi \to ee$ decay.

Figure 22: *Comparison between efficiencies during Run 2 and after the upgrade (2024 data) [53].*

2.5.1 HLT1

The HLT1 is the first level trigger. It is implemented in GPUs and focuses on finding the trajectories of charged particles originating in the LHCb vertex detector and traversing the tracking system. More specifically, it measures the momentum of the particles at percent-level precision, then it associates each particle to the respective primary vertex (PV), measuring the impact parameter with respect to it. Finally, it performs lepton identification [46].

It is based on a two-stages process: reconstruction and selection. The reconstruction sequence is sketched in Fig. 23.

As can be observed, several algorithms are run inside the HLT1 to perform a first event reconstruction [46]:

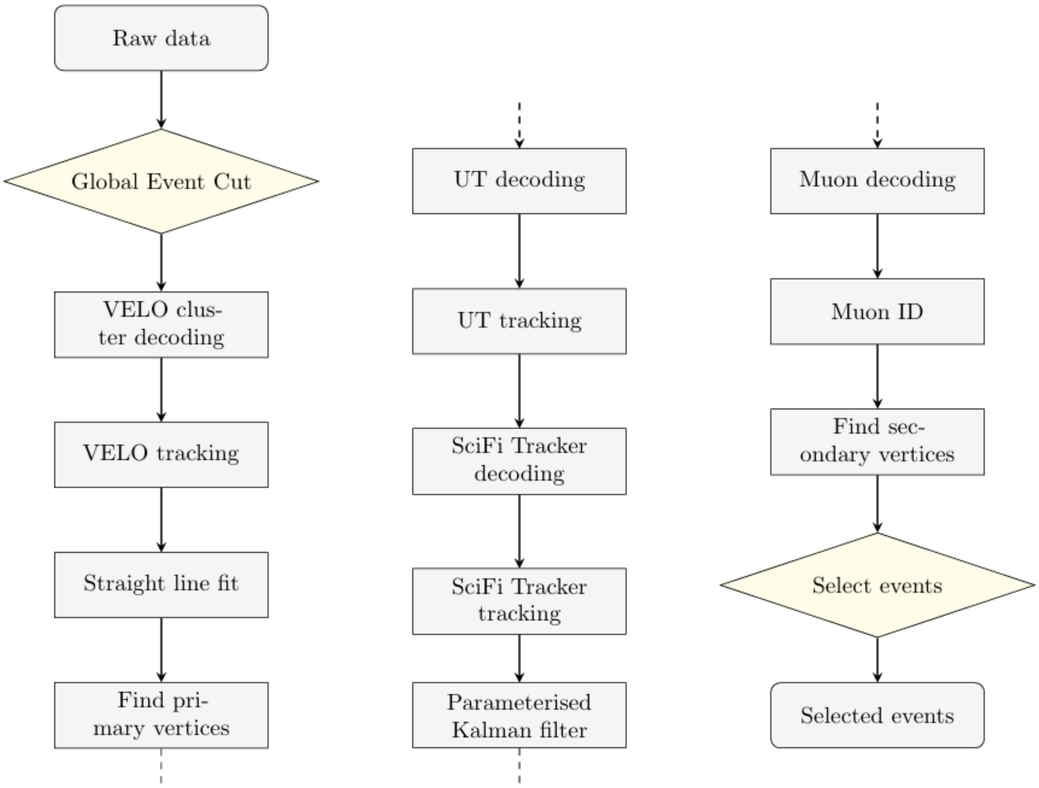

Figure 23: *Baseline HLT1 sequence [54]. ”Rhombi” represent algorithms reducing the event rate, while ”rectangles” represent algorithms processing data [46]. It is worth noting that the Global Event Cut is not applied in the current implementation and the electron identification was also added.*

1. tracks are primarily reconstructed in the VELO and used to find the PV positions;
2. tracks are extrapolated to the other tracking sub-detectors (UT and SciFi);
3. the momentum information is passed to the Kalmar fitter, which estimates the position at the beam line;
4. tracks are identified as leptons/non-leptons.

The HLT1 selection stage is divided into four main categories: inclusive selections, selections for calibration for data-driven performance studies, dedicated triggers for specific physics signatures, and technical triggers for monitoring, luminosity determination, and alignment. The inclusive triggers include:

- a two-track vertex trigger,
- a displaced single-track trigger,
- a displaced single-muon trigger,
- a displaced dimuon trigger,
- a displaced dielectron trigger,
- a high-mass dimuon trigger,
- a very high-p_T muon trigger.

2.5.2 HLT2

After the LHCb Upgrade I, the High Level Trigger 2 (HLT2) plays a central role in the experiment's real-time data processing strategy. It is implemented in CPUs and performs a full offline-quality reconstruction of each event using the information provided by the real-time alignment and calibration [46]. This reconstruction includes all main components: charged particle pattern recognition, calorimeter clustering, particle identification, and a Kalman fit to refine track parameters with higher precision and accuracy.

Unlike the first-level trigger HLT1, which uses inclusive selections, HLT2 applies a large set of $\mathcal{O}(1000)$ dedicated selection algorithms, each optimized for specific final states or physics signatures. These algorithms decide not only whether to retain an event, but also which parts of it should be saved to disk.

3 Analysis of the $D^0 \to K^-\pi^+e^-e^+$ decay

The focus of this thesis is the study of the $D^0 \to K^-\pi^+e^-e^+$ decay channel. Although this mode has already been observed, its importance here lies in the fact that it serves as the normalization channel for the measurement of the branching ratios of the rare decays $D^0 \to K^-K^+e^-e^+$ and $D^0 \to \pi^-\pi^+e^-e^+$. This Section begins with a discussion of the rare channels, in order to provide the context and clarify the role of the normalization channel within the overall analysis framework. Hence, the state of art and the analysis strategy pursued for the search for the rare decays are illustrated in Sec. 3.1 and Sec. 3.2 respectively. Once the framework is introduced, the description of the data analysis for the $D^0 \to K^-\pi^+e^-e^+$ normalization channel begins in Sec. 3.3, where the preliminary selection applied to data in order to reject background and select signal candidates is exposed. Then, a simulation framework named RapidSim is used to generate invariant mass models to describe the background sources that affect the analysis. The validation steps needed to ensure that the simulated events are suitable to describe the data are highlighted in Sec. 3.4. Finally, the fit model used to extract the signal yields for the $D^0 \to K^-\pi^+e^-e^+$ mode is presented in Sec. 3.5, together with the results obtained. This allows us to study the performance of the new detector and to provide an estimate of the expected number of events for the rare channels.

3.1 State of art of the measurements and LHCb Run 2 results for the rare channels $D^0 \to \pi^-\pi^+e^-e^+$ and $D^0 \to K^-K^+e^-e^+$

As previously explained in Sec. 1.7, $D^0 \to h^-h^+e^-e^+$ decays, where h is either a kaon or a pion, can proceed via long-distance (LD) or short-distance (SD) interactions, which makes them sensitive to searches for New Physics. Experimentally, these modes have been investigated by the E791 [55] and BESIII [56] experiments, and more recently by the LHCb collaboration [35]. Hereafter, the focus is placed on the LHCb measurement, as it represents the most recent study of these decay modes and forms the basis of the following analysis, based on data collected by the upgraded LHCb detector.

The analysis of data collected during the LHC Run 2 [35], recorded by LHCb between 2015 and 2018 at a center-of-mass energy of 13 TeV and corresponding to an integrated collected luminosity of 6 fb^{-1}, has led to the first observation of the rare charm decay $D^0 \to \pi^-\pi^+e^-e^+$. In contrast, for the $D^0 \to K^-K^+e^-e^+$ channel, only an upper limit on the branching fraction has been established. The analysis was performed in bins of the di-lepton mass, distinguishing between regions dominated by difference resonances. The decay with pions in the final state was observed when the two electrons are required to be consistent with that coming from the decay of a ϕ or a ρ^0/ω meson.

The results are reported in Tab. 3 [35].

$m(e^-e^+)$ region	$m(e^-e^+)$ [MeV/c^2]	$\mathcal{B}[10^{-7}]$
$\boldsymbol{D^0 \to \pi^+\pi^-e^-e^+}$		
Low mass	$2m_\mu - 525$	$< 4.8\,(5.4)$
η	$525 - 565$	$< 2.3\,(2.7)$
ρ^0/ω	$565 - 950$	$4.5 \pm 1.0 \pm 0.7 \pm 0.6$
ϕ	$950 - 1100$	$3.8 \pm 0.7 \pm 0.4 \pm 0.5$
High mass	< 1100	$< 2.0\,(2.2)$
Total		$13.3 \pm 1.1 \pm 1.7 \pm 1.8$
$\boldsymbol{D^0 \to K^+K^-e^-e^+}$		
Low mass	$2m_\mu - 525$	$< 1.0\,(1.1)$
η	$525 - 565$	$< 0.4\,(0.5)$
ρ^0/ω	> 565	$< 2.2\,(2.5)$

Table 3: *Branching fractions of the $D^0 \to K^+K^-e^-e^+$ and $D^0 \to \pi^+\pi^-e^-e^+$ decays in different ranges of di-electron mass, where the uncertainties are statistical, systematic and due to the limited knowledge of the branching fraction of the normalization channel, respectively. The reported upper limits correspond to 90$\%$ (95$\%$) confidence level [35].*

As far as what regards the lepton flavor universality violation search, the LHCb study on Run 2 data did not report any discrepancy with the LFU hypothesis.

3.2 Analysis strategy

The final goal of the analysis is the evaluation of the branching ratio $\mathcal{B}$ for the rare channels $D^0 \to K^-K^+e^-e^+$ and $D^0 \to \pi^-\pi^+e^-e^+$.

To evaluate the branching ratio of these signal channels, it is necessary to study the decays in comparison with a normalization channel, in order to cancel the majority of the systematic uncertainties. The decay chosen for this purpose is the Cabibbo-favored $D^0 \to K^-\pi^+e^-e^+$, since it is a topologically similar decay but it is expected to be dominated by SM amplitudes and thus not sensitive to NP. The final $\mathcal{B}$ is then evaluated via Eq. (47):

$$\frac{\mathcal{B}(D^0 \to h^-h^+e^-e^+)}{\mathcal{B}(D^0 \to K^-\pi^+[e^-e^+]_{\rho^0/\omega})} = \frac{N(D^0 \to h^-h^+e^-e^+)}{N(D^0 \to K^-\pi^+[e^-e^+]_{\rho^0/\omega})} \times \frac{\epsilon(D^0 \to K^-\pi^+[e^-e^+]_{\rho^0/\omega})}{\epsilon(D^0 \to h^-h^+e^-e^+)} \tag{47}$$

where N are the yields extracted from maximum likelihood fits to the D^0 candidate mass distributions, operated on both the normalization and signal channels, while the

ϵ takes into account the total efficiencies, specifically the trigger, reconstruction and offline selection efficiency.

The normalization channel branching fraction is taken as an external input from a previous BaBar measurement [57]. This channel was measured only in the ρ^0/ω dilepton mass region, corresponding to $m(e^-e^+) \in [675, 875]$ MeV[2], and the final result obtained was

$$\mathcal{B}(D^0 \to K^-\pi^+[e^-e^+]_{\rho^0/\omega}) = (4.0 \pm 0.5 \pm 0.2 \pm 0.1) \times 10^{-6} \tag{48}$$

The large relative error of this measurement ($\sim 13.7\%$) propagates linearly in the final result of the branching ratio and thus it is one of the most significant contributors to the overall measurement uncertainty. This systematic uncertainty is treated separately from the other systematics, so that it can be updated if a more precise measurement becomes available.

For the reasons previously explained in Sec. 1.7, recalling that these decays can proceed via both long-distance and short-distance interactions, the dataset is divided in regions of the di-lepton mass, in order to be more sensitive to the short-distance contributions and so to be more sensitive to possible BSM physics. These regions are reported in Tab. 4.

bin $m(e^-e^+)$ [MeV]	very low (only e^-e^+) < 211.32	low mass 211.32 - 525	η 525 - 565	ρ/ω 565 - 950	ϕ 950 - 1100	high mass $>$ 1100
$D^0 \to \pi^+\pi^-e^-e^+$	[✓]	✓	✓	✓	✓	✓
$D^0 \to K^+K^-e^-e^+$	[✓]	✓	✓	✓		

Table 4: *Dilepton mass bins considered for the analysis. The last 2 bins are not kinematically available for the $D^0 \to K^-K^+e^-e^+$ decay. The very low region is available only for the electron modes, thus it's not possible to compare this region with the corresponding muon channels.*

In addition, to compare the results with the corresponding muon channels and to provide a test for LFU, the bin $m(e^-e^+) \in (675, 875)$ MeV is also studied. Regarding the normalization channel, which is the focus of this work, the yield is evaluated only in this region, as it must match the di-electron window for which the BaBar measurement of $\mathcal{B}$ [57] is available.

In searches for rare decays, the signal is typically subject to several sources of background. These include both physical backgrounds, arising from processes that mimic the signal (e.g. partially reconstructed decays or misidentification), and combinatorial background, originating from random combinations of tracks. In order to mainly

---

[2] From now on, we are working in natural units so $c = 1$ and $[E] = [M]$.

reduce the combinatorial one, the analysis relies on D^0 mesons originating from a D^{*+} decay, $D^{*+} \to D^0\pi_s^+$, where the parent D^{*+} is produced in the primary pp collision vertex and π_s^+ is a soft pion[3]. A sketch of the event topology is shown in Fig. 24. This requirement allows to introduce a selection cut on the Δm variable, defined as $\Delta m = m(D^{*+}) - m(D^0)$, essential to reject background.

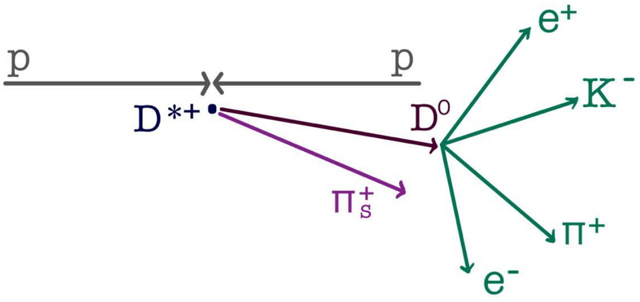

Figure 24: *Event sketch for the normalization channel* $D^0 \to K^-\pi^+e^-e^+$. *The proton proton collision generates the* D^{*+} *particle, which decays promptly into a* D^0 *meson and a soft pion* π_s^+.

Due to the different shapes of the signal mass distribution, and different level of the background sources, the dataset is divided according to the bremsstrahlung emission, identified in the so-called ”brem category”:

- brem 0: events where neither of the two electrons have a reconstructed photon associated;
- brem 1: events where at least 1 bremsstrahlung photon is reconstructed and associated to one of the 2 electrons.

The invariant-mass distribution for simulated D^0 candidates belonging to the two categories is shown in Fig. 25. It is worth noting that the reconstruction and proper association of the emitted photon to the electrons is a difficult task in LHCb. Indeed, while electrons are reconstructed thanks to the tracks left in the tracker and to the electromagnetic shower induced in the ECAL, photons can be reconstructed only by means of the cluster reconstruction in the ECAL. Moreover, electrons, unlike photons, are deviated by the magnet. Consequently the proper association of photons to the emitting electron and the proper reconstruction of the D^0 energy require a careful analysis. Indeed, analyzing Fig. 25, one can observe that for brem 1 category the distribution is broaden and smeared on both sides, where the right side is due to one or more electrons associated to wrong (and too energetic) photons, implying reconstructed masses higher

---

[3] The soft pion is so called because of its low momentum, corresponding to the difference between the masses of the charmed mesons D^{*+} and D^0, which is around ~ 145 MeV.

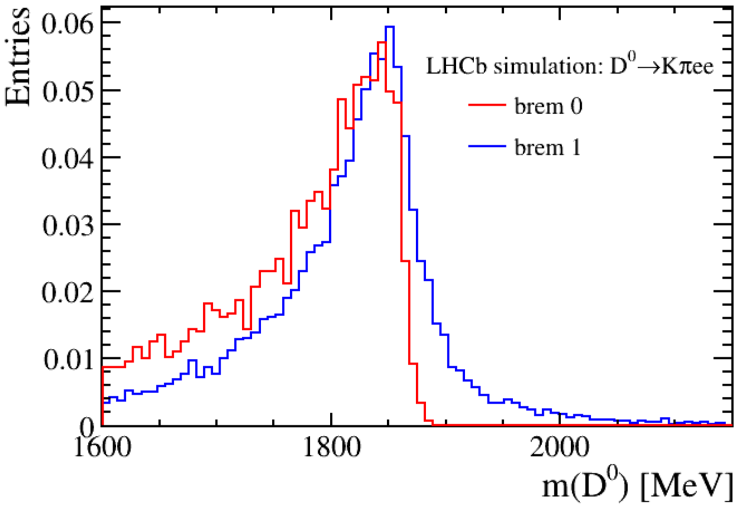

Figure 25: *The distributions of the D^0 mass candidates for both brem categories is shown. The plot shows data from the official LHCb MC simulation. In blue one can observe the brem 1 category, while in red the brem 0 one.*

than that expected for the D^0 meson. The tail on the left side is smaller compared to that of brem 0 thanks to the brem recovery algorithm, which helps in mitigating the energy loss. In contrast, the brem 0 category is characterized by a sharp cut-off after the expected D^0 mass value and a much longer tail on the left, due to the possibility of underestimating the energy by failing to reconstruct one or more photons.

3.3 Selection applied to $D^0 \to K^-\pi^+e^-e^+$ data

In this Section the first analysis steps performed on the normalization channel $D^0 \to K^-\pi^+e^-e^+$ are reported. In particular, the preselection cuts applied to the data and the multivariate selection used to suppress the combinatorial background are described in detail. The final goal is to reduce the background in order to be able to estimate the yield for the normalization channel, necessary to evaluate the final branching ratios of the rare channels.

3.3.1 Data samples

The following analysis is performed using data collected by the LHCb detector during Run 3. The proton-proton collision are carried out at a center of mass energy of $\sqrt{s} = 13.6$ TeV. The dataset used corresponds to 2024 data. Generally, data are divided into *blocks* corresponding to different data taking periods. The *blocks* used are numbers 1,2,5,6,7 and 8, corresponding to a total integrated luminosity of 5.1 fb^{-1}. *Blocks* numbers 3 and 4 are excluded in this analysis since they were collected during an unstable data-taking phase for the LHCb upgrade detector and need further and more complex studies in order to be exploited.

3.3.2 Trigger lines selection

The trigger selection is part of the LHCb online data acquisition system. Events are selected in real time through a two-stage software-only trigger. The first level (HLT1) is implemented as a set of different inclusive lines, each optimized for specific decay signatures or topologies. In particular, for this analysis the events are categorized according to the following criteria:

- The primary inclusive HLT1 trigger lines are based on a neural network architecture and select a single track with significant transverse momentum and displacement from any primary collision, denoted `Hlt1TrackMVA`; or a two-track vertex whose constituent parts satisfy analogous criteria, denoted `Hlt1TwoTrackMVA`. We refer to them as `TrackMVAs`.

- Dedicated HLT1 lines for electrons: `Hlt1TrackElectronMVA`, which implements the same type of selection as the `Hlt1TrackMVA` line but applies electron identification; and `Hlt1TDiElectronDisplaced`, that reconstructs a pair of electrons, which have significant displacement from any primary collision. These lines benefit from the fact that in Run 3 HLT1 is able, for the first time, to implement both a full calorimeter reconstruction and a calorimeter-only electron identification. We refer to them as `Only E`.

- events passing both of the above selections, referred to as `AND`.

It is worth noting that the three sub-datasets are mutually exclusive and the analysis will be performed separately for each of them to optimize the data selection.

3.3.3 Preselection cuts

The first selection applied to candidates fulfilling the trigger requirements is reported in Tab. 5. The variables used for this selection are:

- `TRACKGhostProb`, a multivariate discriminator trained on quantities relying on the LHCb tracking system, necessary to reduce the amount of ghost tracks, *i.e.* tracks that are not produced by real particles;

- `PROBNN_K` and `PROBNN_PI`[4] are PID variables based on the information provided by the RICH, ECAL and MUON detectors, on which strong cuts are applied to suppress cross-feed due to hadron mis-identification;

---

[4] `PROBNN` stands for *probability evaluated by the neural network.*

- `OWNPV_IP_CHI2`, which represent the impact parameter χ^2 with respect to the associated primary vertex and helps removing part of the combinatorial background.

Particle	Cut	Total efficiency
π_s^+, K^-, π^+, e$^\pm$	TRGHOSTPROB < 0.3	78%, 88%, 95%, 86%
K^-	PROBNN_K > 0.7	38%
π^+	PROBNN_PI > 0.7	84%
D^0	OWNPV_IP_CHI2 < 9	67%

Table 5: *Cuts applied to each particle and their efficiencies obtained from signal simulated events.*

An additional cut is performed on the Δm variable, since its distribution is helpful in rejecting background. The $\Delta m \doteq m_{DTF}(D^{*+}) - m_{DTF}(D^0)$ is evaluated after refitting the full decay chain, requiring the D^{*+} decay vertex and the primary vertex (PV) to be the same, using the `DecayTreeFitter` [58] algorithm. The requirement imposed is 144 MeV $< \Delta m < 147$ MeV. As can be observed in Fig. 26, where the requirement is highlighted by 2 pink lines, the selection of this region allows us to retain mostly signal events.

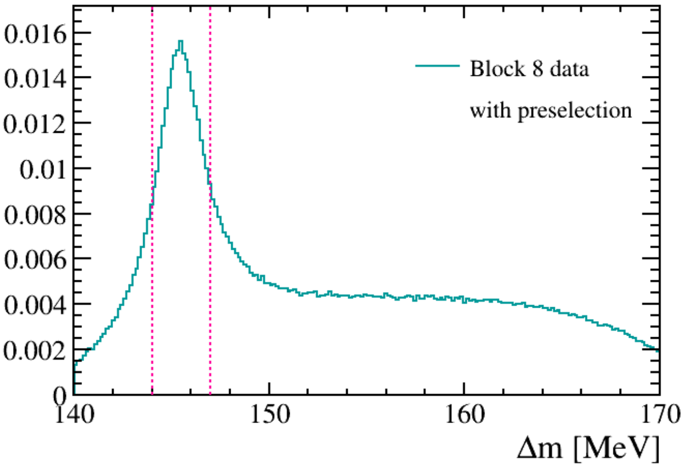

Figure 26: *The distribution of the Δm variable, defined as the difference between $m(D^{*+})$ and $m(D^0)$ after the* DTF *evaluation, is shown. The dataset corresponds to block 8, without distinction in brem category, and after the application of all preselection cuts except the cut on Δm. The pink lines indicate the cut "144 MeV $< \Delta m < 147$ MeV".*

Applying selection cuts allows us to reject background with little signal loss. The comparison between data without preselection and after the preselection applied can be observed in Fig. 27. However, not all the background is rejected, thus it is useful to perform a multivariate selection.

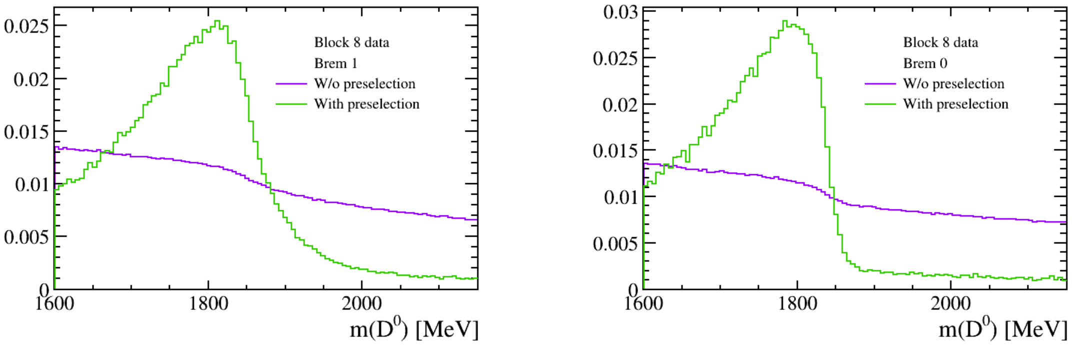

(a) *Brem 1 filtered data.* (b) *Brem 0 filtered data.*

Figure 27: *The plots show the comparison between data with and without the preselection cuts applied. Data corresponds to block 8 only (because of the large amount of statistics). In purple histograms represent data without cuts, where a small peak can be slightly observed; while histograms in green are after the selection. On the left brem 1 (a), on the right brem 0 (b). No dilepton filter is applied.*

3.3.4 Multivariate selection

The last step to reject combinatorial background events is performed by means of a Boosted Decision Tree (BDT) method. This machine learning algorithm is implemented in the TMVA (Toolkit for MultiVariate Analysis) ROOT framework [59].

More specifically, the BDT selection is carried out by training the classifier on a set of input variables that exhibit a good discriminating power between signal and background events. During the training, the algorithm assigns weights to each input variable and learns how to optimally separate the two classes of events, providing an output BDT response distribution. The best cut on the BDT variable is evaluated via the maximization of a chosen Figure of Merit (FoM) in order to optimize background rejection. Finally, during the application phase, weights are applied to data, the BDT output variable is evaluated for each event and the best cut is applied, rejecting events that do not satisfy the BDT requirement. Hereafter, the above cited steps are described in details.

Training and BDT variables The classifier should be trained using samples that are representative of the signal mode and of the combinatorial background. Hence, the samples provided, filtered for trigger line and integrated over the whole di-lepton mass region, are:

- sample for signal: events from the LHCb official simulation, after the application of truth matching [5], without distinction between bremsstrahlung categories;
- sample for background: data sideband corresponding to the $m(D^0) > 1900$ MeV region for the brem 0 category, considering all data *blocks* except *block* 3 and 4.

The decision to train the classifier without distinction between brem categories for the signal sample is due to the limited available statistics from the official LHCb simulated samples at the time of this analysis. As a cross-check, the distributions of the variables provided to the BDT classifier were compared between brem 1 and brem 0 categories and they did show a good agreement. This comparison is reported in Appendix A. On the other hand, the choice of the background sideband, requiring events corresponding only to brem 0 category, is driven by the the fact that in the high-mass region of the D^0 distribution only combinatorial background is present, with no signal contribution, as can be observed in Fig. 25.

The variables used for the BDT training are the following:

- Dst_DTF_CHI2: χ^2 of the kinematic constraint (`DecayTreeFitter` [58]) applied to the entire D^{*+} decay chain;
- Dst_HEAD_LongTrackIso_0_5_PTASY: transverse momentum asymmetry between the D^{*+} candidate and long tracks within a cone of radius $\Delta R = 0.5$ around the D^{*+} direction;
- Dst_MAXDOCA: maximum distance of closest approach between the daughter tracks of the D^{*+} particle, *i.e.* π_s^+ and D^0 tracks;
- Dst_OWNPVFDCHI2: χ^2 of the flight distance, *i.e.* the distance between the particle's decay vertex and its associated production vertex, of the D^{*+} with respect to its own primary vertex;
- Dst_OWNPVIP: impact parameter, *i.e.* the minimum distance between a particle's trajectory and a reference vertex, of the D^{*+} candidate with respect to its associated primary vertex.
- Dst_OWNPVIPCHI2: χ^2 of the impact parameter of the D^{*+} candidate with respect to its associated primary vertex.

---

[5] The process of truth matching consists in verifying that the reconstructed candidate, after the reconstruction step, is indeed the generated one. This is made possible by the record of the true identity of the particles produced by the event generator.

- Dst_p: momentum p of the D^{*+};
- Dst_p$_\mathrm{T}$: transverse momentum p_T of the D^{*+};
- D0_MAXDOCA: maximum distance of closest approach between any pair of daughter tracks of the D^0 particle;
- D0_OWNPVFD: flight distance of the D^0 particle with respect to its own primary vertex;
- D0_OWNPVIP: impact parameter of the D^0 candidate with respect to its associated primary vertex.
- D0_OWNPVIPCHI2: χ^2 of the impact parameter of the D^0 with respect to its own primary vertex;
- log_abs_D0_OWNPVDIRA: logarithm of the absolute direction angle of the D^0, evaluated as the cosine of the angle between the reconstructed momentum and its flight vector from its associated primary vertex;
- spip_ETA: pseudorapidity η of the slow pion π_s^+, *i.e.* the angle of the particle with respect to the beam axis.
- spip_OWNPVIP: impact parameter of the π_s^+ candidate with respect to its associated primary vertex.
- Km_p$_\mathrm{T}$: transverse momentum p_T of the K^-;
- pip_p$_\mathrm{T}$: transverse momentum p_T of the π^-;
- lp_p$_\mathrm{T}$: transverse momentum p_T of the e^+;
- lm_p$_\mathrm{T}$: transverse momentum p_T of the e^-;
- dilepton_ENERGY: total energy of the di-lepton system;
- dilepton_MAXDOCA: maximum distance of closest approach for the di-lepton system;
- dilepton_OWNPVFDCHI2: χ^2 of the flight distance of the dilepton system with respect to its own primary vertex;
- dilepton_OWNPVIP: impact parameter of the dilepton system with respect to its associated primary vertex.
- dilepton_p$_\mathrm{T}$: transverse momentum p_T of the e^-e^+ system;

Their distributions are reported in Fig 28 and Fig 29 [6]. It has been verified that these variables are uncorrelated with the D^0 mass variable, to avoid biases in the selection. The plots showing the correlation can be found in Appendix B. The multivariate selection is performed separately for the three trigger lines since the variables' distributions are observed to show discrepancies between each other (distributions are reported in Appendix C). This approach allows a better optimization of the BDTs.

BDT response Once the training of the BDT is concluded, the classifier provides the BDT response as output, allowing for the comparison of the distributions of the training and test samples. Indeed, during the training phase of the BDT, the dataset is typically split into a training sample and a test sample. The former is used to build the model, while the latter to evaluate the model's performance. This approach is necessary to prevent overtraining, which occurs when the method adapts too closely to the specific features of the training sample, reducing its ability to distinguish signal from background in independent data. These distributions are reported in Fig. 30, for the `AND`, `Only E` and `TrackMVAs` trigger lines, together with their corresponding Receiver Operating Characteristic (ROC) curves. ROC curves show the signal efficiency versus the background rejection for different possible cut points of a classifier [59]. If the classifier has no discriminating power, signal and background completely overlap, and the ROC curve reduces to a diagonal line, corresponding to an area under the curve of about 0.5 - no better than random guessing. In contrast, for a good classifier with strong separation between signal and background, the curve approaches the upper right corner of the plot, corresponding to an area under the curve close to 1.

The FoM which is maximized in order to determine the best cut on the BDT variable is the Significance:

$$\mathcal{S} = \frac{S}{\sqrt{S+B}}, \tag{49}$$

where S and B are the expected number of signal and background events, respectively. To provide an estimate of these values a preliminary fit to the data is required. The present BDT optimization helps to suppress the background to a reasonable level. In the final analysis, which focuses on the rare channels $D^0 \to K^-K^+e^-e^+$ and $D^0 \to \pi^-\pi^+e^-e^+$, a dedicated BDT will be trained and applied on top of the existing one to further suppress the background. Since these channels are not observed in all di-lepton mass bins, the optimization will be carried out using the Punzi figure of merit [60].

The optimization of the BDT cut is performed estimating the number of events on the brem 1 sample, which offers higher statistical power, and the same cut is then applied to the brem 0 sample. This choice is motivated by the fact that, in the final anal-

---

[6] The data samples used to show the behavior of these variables comprises data of all three trigger categories sub-datasets, since the aim is to show the different distributions for the variables between signal and background samples.

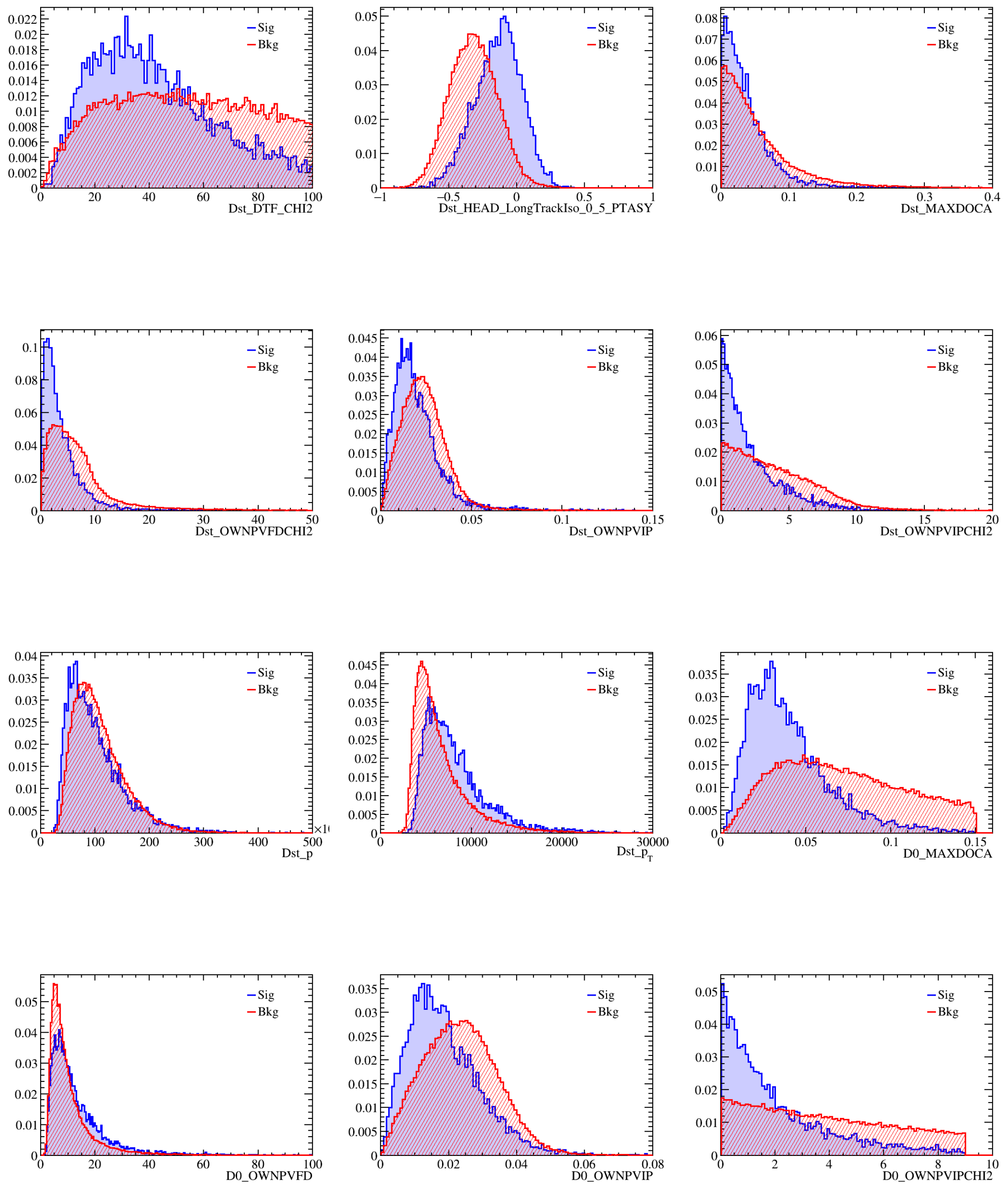

Figure 28: *Input variables for the BDT training. Distributions of signal in blue and background in red.*

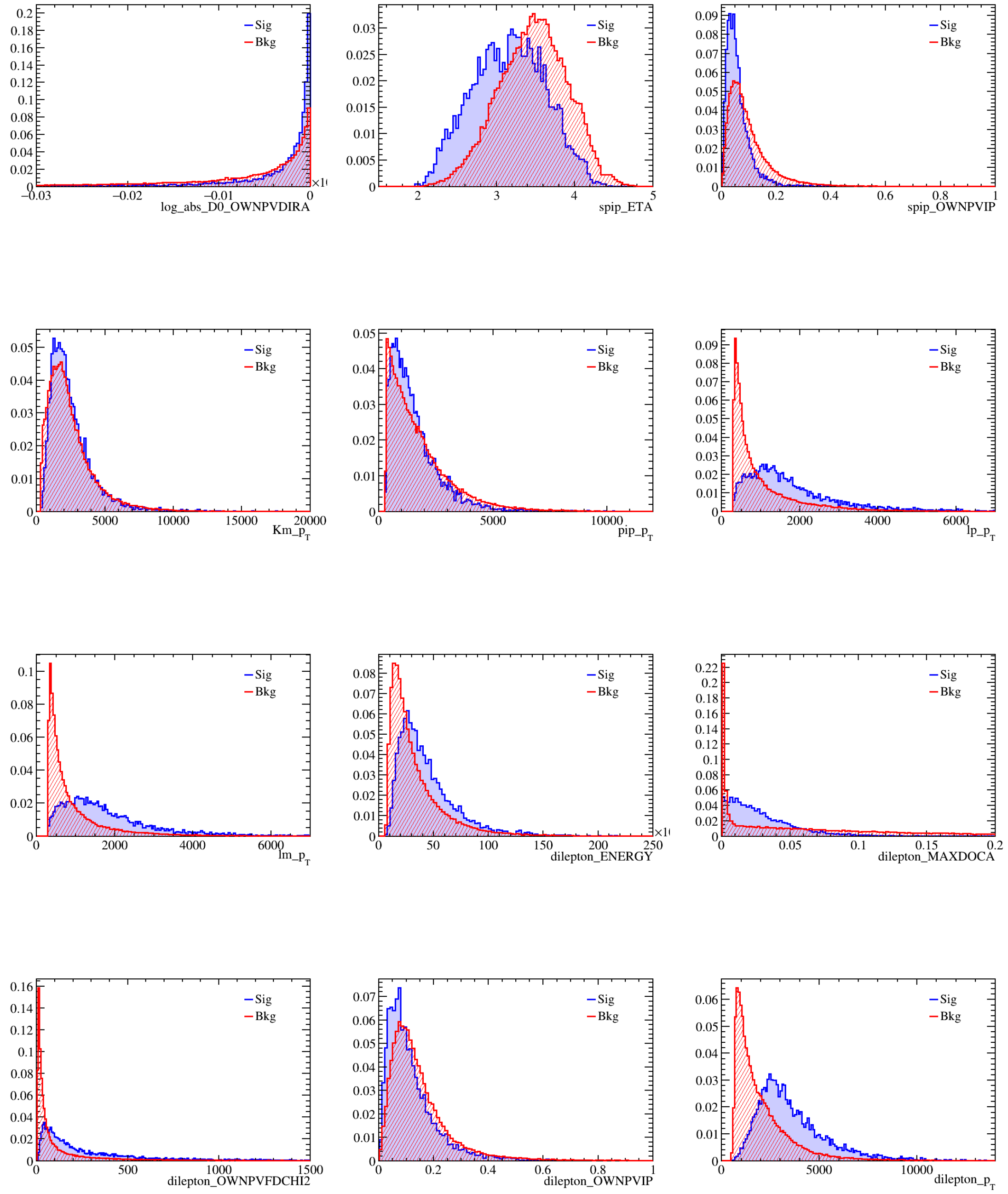

Figure 29: *Input variables for the BDT training. Distributions of signal in blue and background in red.*

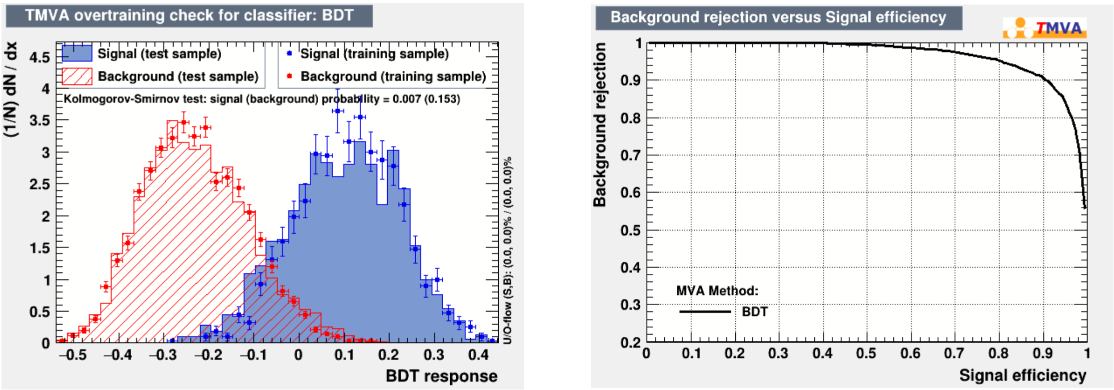

(a) `AND` trigger line.

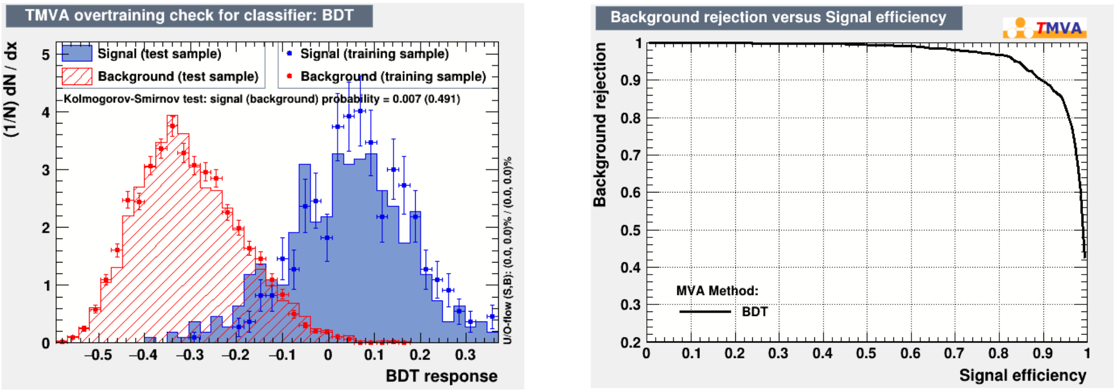

(b) `Only E` trigger line.

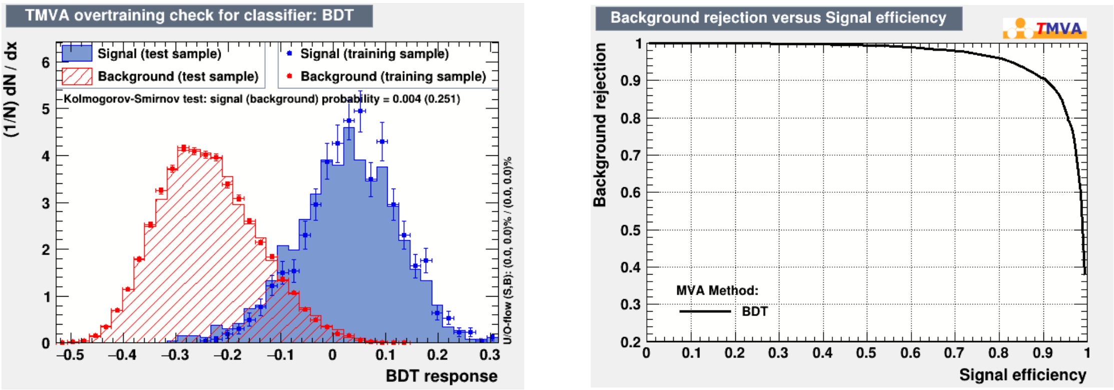

(c) `TrackMVAs` trigger line.

Figure 30: *The BDT response for the training and test sample (left) and the ROC curve (right) are reported. The plots in each row correspond to the trigger lines categories.*

ysis, the yield of the misidentified background component ($D^0 \to K^-\pi^+\pi^-\pi^+$) in the brem 1 category is estimated from its ratio to the brem 0 data; therefore, it is important to apply a consistent cut to both samples.

In order to estimate the number of signal and background events to maximize $\mathcal{S}$, a fit to the data needs to be performed. The model chosen to describe the signal component has been studied on a sample of simulated events. The fitting function is a Johnson PDF, Eq. (50) [61]

$$\text{PDF[Johnson } S_U] = \frac{\delta}{\lambda\sqrt{2\pi}} \frac{1}{\sqrt{1+\left(\frac{x-\mu}{\sigma}\right)^2}} \exp\left[-\frac{1}{2}\left(\gamma + \delta \sinh^{-1}\left(\frac{x-\mu}{\sigma}\right)\right)^2\right]. \tag{50}$$

It is described by four parameters: mean (μ) and sigma (σ), that represent the peak position and width; gamma (γ) and delta (δ), that parametrize the tails. In Fig. 31 the results of a fit to the simulated events D^0 invariant-mass distribution in the interval $m(e^-e^+) \in [675, 875]$ MeV are shown. The parameters' values are reported in Tab. 6. When fitting real data, the tail parameters are constrained to the values obtained from simulated events.

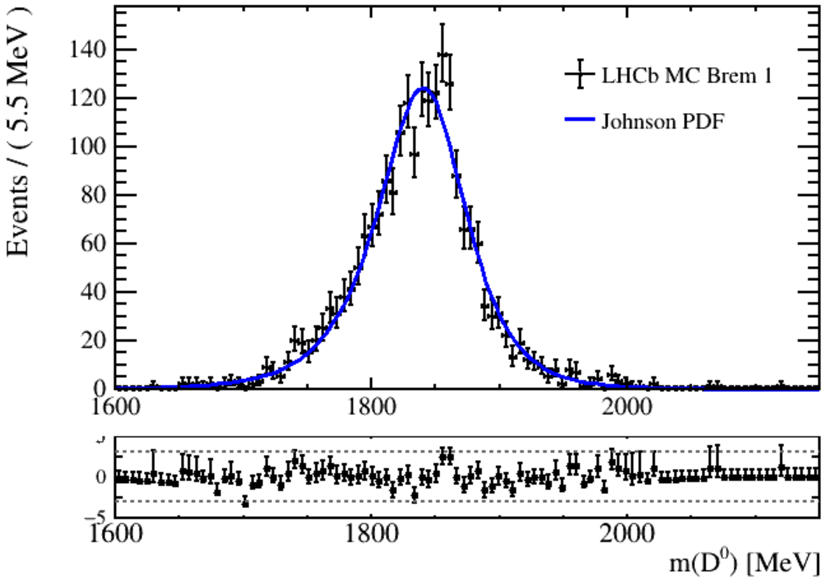

Figure 31: *Distribution of the D^0 invariant mass in MC data for the brem 1 category (black) with the fit function overlayed (blue). The pull distribution is also shown underneath.*

The data samples used to maximize the significance corresponds to data of all *blocks* except 3 and 4, filtered for brem 1 category and $m(e^-e^+) \in (675,\ 875)$ MeV, divided

Johnson parameters	Fit results
μ	1846.5 ± 1.2
σ	48.7 ± 1.8
γ	0.20 ± 0.06
δ	1.42 ± 0.09

Table 6: *Parameters of the brem 1 signal PDFs evaluated on official LHCb MC sample of $D^0 \to K^-\pi^+e^-e^+$, brem 1, filtered for di-lepton mass bin $m(e^-e^+) \in [675, 875]$ MeV.*

according to the three trigger lines. The fits are shown in Fig. 32a, Fig. 32b and Fig. 32c, respectively. The combinatorial background is described using a second order Chebychev polynomial. The measured number of signal and background events in the signal region, i.e. $[1700, 2000]$ MeV, for the three categories is reported in Tab. 7. Using these numbers in the BDT optimization procedure, the best cut values are extracted. The results are reported in Tab. 7 and can be observed in Fig. 33a, Fig. 33b and Fig. 33c. As previously explained, these cuts are applied to data in both brem 1 and brem 0 categories.

Trigger line	Signal events	Background events	Best BDT cut
`AND`	2807	4549	-0.0650
`Only E`	1016	4162	-0.0728
`TrackMVAs`	3033	10422	-0.0656

Table 7: *Estimate number of signal and background events in $[1700, 2000]$ MeV, extracted from the preliminary fit to data. The corresponding best BDT cut is also listed.*

3.4 RapidSim Setup

3.4.1 Motivation

The search for rare decays requires a thorough understanding of the expected distributions for both the signal and background sources, in order to be able to provide some constraints in the fit to data samples. Usually, the signal fit model and the main sources of background for a specific channel are studied via the analysis of simulated events produced by the official LHCb simulation framework. This approach should have been pursued in our case too.

Unfortunately, at the time of this analysis, simulated events were available only for the normalization channel $D^0 \to K^-\pi^+e^-e^+$, consisting of 16538 events after truth matching. However, the need to extract information on the background distributions as

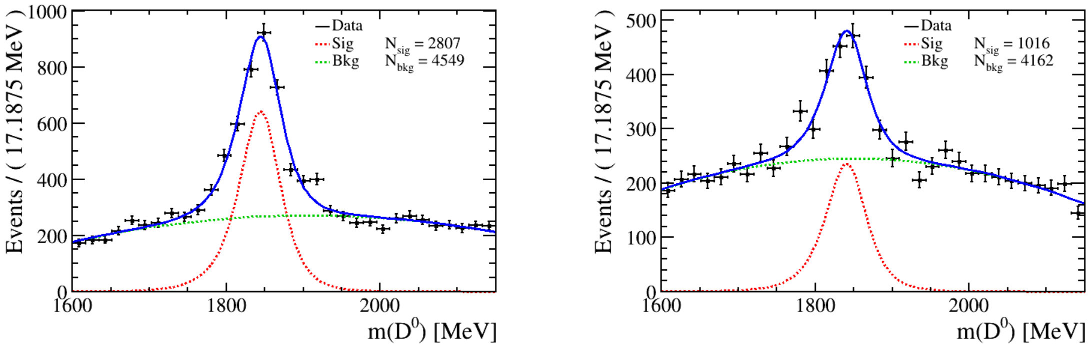

(a) `AND` trigger line.

(b) `Only E` trigger line

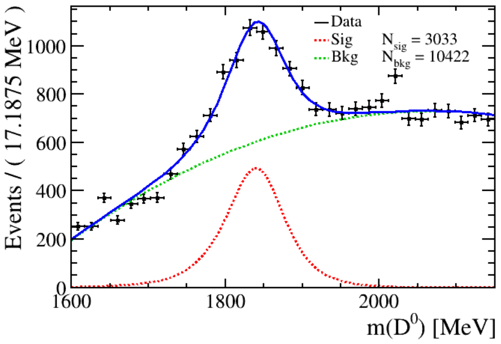

(c) `TrackMVAs` trigger line

Figure 32: *The three plot show the preliminary fit to the data performed to extract the number of signal and background events in the signal region defined between* 1700 *MeV and* 2000 *MeV. The samples used corresponds to data of all blocks (besides 3 and 4), filtered brem 1 and for* $m(e^-e^+) \in [675, 875]$ *MeV, divided according to trigger line. The total fit is displayed in blue, while the signal and the background fit components are respectively in red and green.*

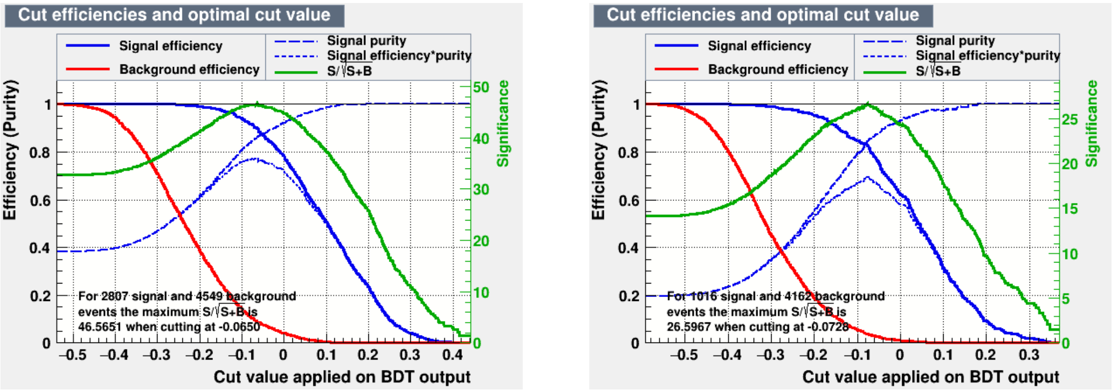

(a) `AND` *trigger line*

(b) `Only E` *trigger line*

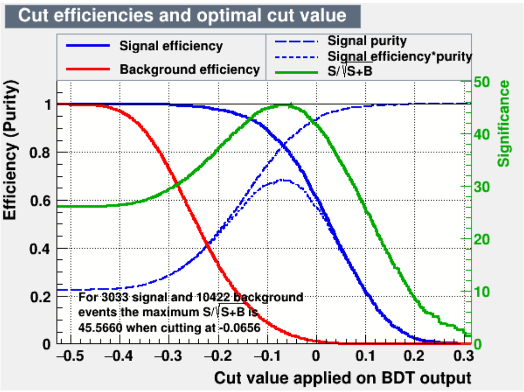

(c) `TrackMVAs` *trigger line*

Figure 33: *The plots show signal purity in blue, the background efficiency in red and the significance* $\mathcal{S} = \frac{S}{\sqrt{S+B}}$ *in green. Setting the number of events for the signal and background categories, it is possible to infer the best BDT cut value corresponding to the maximization of the significance.*

well required finding an alternative approach. Background data were simulated using the RapidSim framework [62] in conjunction with EvtGen [63], a Monte Carlo event generator that simulates the decays of heavy flavour particles.

Before blindly relying on RapidSim and using it for our studies, it is essential to validate the simulator. This is achieved by using official LHCb simulated samples of the $D^0 \to K^-\pi^+e^-e^+$ decay as input to RapidSim, with the setup tuned to reproduce the corresponding kinematic distributions. The validation is performed individually on the two brem categories since the distributions show differences, as already stated, and RapidSim does not provide us with a variable which allows for the discrimination between bremsstrahlung emission or not. Consequently, it is necessary to run separate generations and for this reason the setup steps performed for the validation and described from Sec. 3.4.3 to Sec. 3.4.8 are followed separately for the two categories.

3.4.2 What is RapidSim?

RapidSim is a fast Monte Carlo generator for the simulation of heavy-quark hadron decays. It uses the TGenPhaseSpace class from the ROOT application to generate b or c quark hadron decays and FONLL to externally provide fixed-order next-to-leading-logarithm calculations, that are used to boost the initial beauty and charm hadrons to the appropriate energy corresponding to the production environment of interest. More specifically, FONLL calculate differential cross sections for charm or bottom quark production at pp (or $p\bar{p}$) colliders, with cuts on p_T and y or η [62]. RapidSim also provides the opportunity to smear particle momenta by means of user-defined resolutions and to impose cuts on daughter particle properties. Moreover, it is possible to set alternative mass hypothesis, to study the distributions of decays where mis-identification occurs, and to set the status of a particle as invisible, to produce partially reconstructed decays.

Event Gen EvtGen is a Monte Carlo event generator used in several computing framework in high-energy physics to simulate the decays of heavy hadrons [64]. It contains many detailed decay models, that correspond to separate modules implementing the dynamics of a specific decay type. For each node in the decay tree, the framework uses the corresponding amplitude to simulate the entire decay chain [63]. The external dependency PHOTOS is used in our simulation to reproduce the final-state radiation (FSR). Several models are implemented in EvtGen [65], some examples are:

- VSS, which decays a vector particle into two scalars (e.g. $D^{*+} \to D^0\pi^+$ or $\overline{K^{0*}} \to K^-\pi^+$);
- PHSP, a generic phase space to n-bodies, where all spins of particles in the initial and final states are averaged (e.g. $D^0 \to K^-\pi^+e^-e^+$);
- VLL, to simulate the decay of a vector particle of spin 1 into two leptons (e.g. $\omega \to e^-e^+$);
- SVV_HELAMP, to decay a scalar particle to two vector particles by specifying their helicity amplitudes (e.g. $D^0 \to \overline{K}^{0*}\rho^0$).

Many other decay modules are implemented, but not used for our simulations and therefore not reported here.

3.4.3 Decay descriptor and configuration files

In order to generate each decay, RapidSim requires two files:

- a decay file, with a `.decay` extension, containing the description of the decay and of the full decay chain;

- a configuration file, with a `.config` extension, containing the setting options to provide to the simulator.

For the $D^0 \to K^-\pi^+e^-e^+$ channel, the decay descriptor reads:

`D*+ -> {D0 -> K- pi+ e+ e-} pi+.`

It is worth noting that this decay descriptor implies that no resonances are generated. However, the distributions for the validation are produced taking into consideration the complete decay model, further described in Sec. 3.4.4.

The configuration file sets the acceptance and the geometry of the detector, the center of mass energy of the collisions, the desired distributions for both stable and decaying particles and the (user-defined) smearing options for stable particles. In addition, it enables EvtGen (for which PHOTOS use is required). For the decays that proceed without resonances, the $\overline{K}^{*0}$ and di-lepton distributions are evaluated as the sum of the K^-, π^+ and e^-, e^+ ones respectively.

For the sake of an example, in the *Appendix* D both the decay and configuration files for a decay proceeding via resonance and for one proceeding without generating resonances are reported.

3.4.4 Decay model

The $D^0 \to K^-\pi^+e^-e^+$ decay may proceed via intermediate resonances or directly without them. It is not possible to provide RapidSim with the complete decay model and obtain a unique generation according to it, so an alternative strategy was used. Several generations, one for each specific decay model, were produced and then mixed together according to the proportions used in the official LHCb simulation framework, reported in the so-called `decfiles`. The decay model used is the same for the two brem categories. The possible decay channels and the number of events generated for the normalization channel $D^0 \to K^-\pi^+e^-e^+$ are reported in Tab. 8.

3.4.5 MC sample for the setup

The following Sections will describe the setup of the parent D^{*+} particle kinematics and the smearing options for the daughters. The dataset used to produce the input distributions for RapidSim is the official LHCb simulated sample for the normalization channel, truth-matched, without preselection cuts, and including both reconstructed and truth-level distributions. The brem filter is applied, so the dataset consists of:

- 12633 events for brem 1 category;
- 3905 events for brem 0 category.

Even though the validation will be performed in the dilepton region $[675, 875]$ MeV, for the setup this di-lepton filter is not applied to have more statistics.

Decay descriptor	Number of generated events
$D^{*+} \to (D^0 \to K^-\pi^+e^-e^+)\pi^+$	10^6 events
$D^{*+} \to (D^0 \to K^-\pi^+(\omega \to e^-e^+))\pi^+$	10^6 events
$D^{*+} \to (D^0 \to K^-\pi^+(\rho \to e^-e^+))\pi^+$	10^6 events
$D^{*+} \to (D^0 \to (\overline{K}^{*0} \to K^-\pi^+)e^-e^+)\pi^+$	10^6 events
$D^{*+} \to (D^0 \to (\overline{K}^{*0} \to K^-\pi^+)(\omega \to e^-e^+))\pi^+$	10^6 events
$D^{*+} \to (D^0 \to (\overline{K}^{*0} \to K^-\pi^+)(\rho \to e^-e^+))\pi^+$	10^6 events

Table 8: *Resonant and non-resonant decays simulated for the normalization channel* $D^0 \to K^-\pi^+e^-e^+$.

3.4.6 D^{*+} setup

RapidSim generates the entire decay chain while enforcing energy–momentum conservation, which makes it impossible to reweight the kinematic distributions of all particles a posteriori to match those from the official LHCb simulation. Instead, an alternative approach was adopted: the D^{*+} kinematics were used as input to the RapidSim generation, ensuring proper energy–momentum conservation across the full decay chain. The distributions from which the D^{*+} kinematics are sampled are:

- 2D distribution of $p_T - \eta$,
- 1D distribution of ϕ angle.

The distributions are reported in Fig. 34 and Fig. 35, respectively for brem 1 and brem 0 categories. In this case only TRUE distributions were used, since RapidSim applies a user defined smearing to all the final-state particles and then propagates its effects back to the parent particle.

3.4.7 Hadrons' setup

For the final state particles, so those that do not decay and thus are stable, it is possible to provide user-defined smearing options. There are two possibilities to provide resolution functions:

- a Gaussian distribution with a p-dependent width approach - making the width of the resolution vary continuously in different p ranges;
- a histogram-based approach: provide directly one (or several) histograms that describe the resolution in different p-ranges. In this way it is possible to account for asymmetric effects in the resolution.

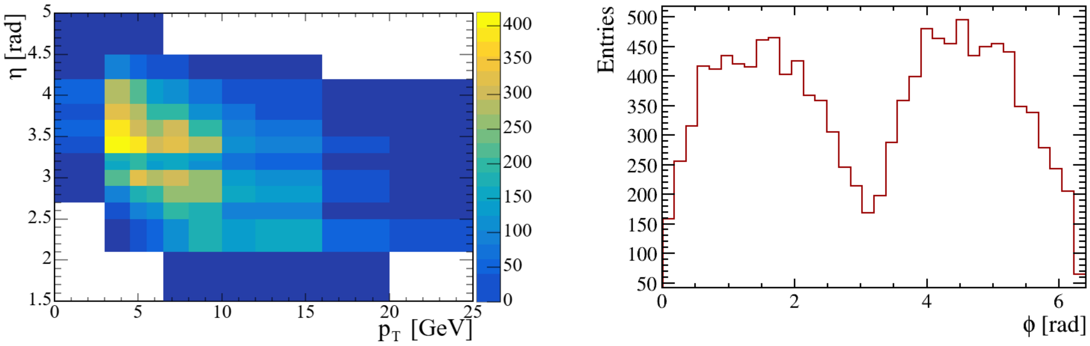

(a) *2D plot of $p_T - \eta$ variables. The binning is chosen in order to have a similar number of events in each bin.*

(b) *Distribution of the ϕ angle. 36 bins are used.*

Figure 34: *The distributions of the D^{*+} used as input for the RapidSim simulation of the brem 1 category are shown. The dataset used consists of 12633 events.*

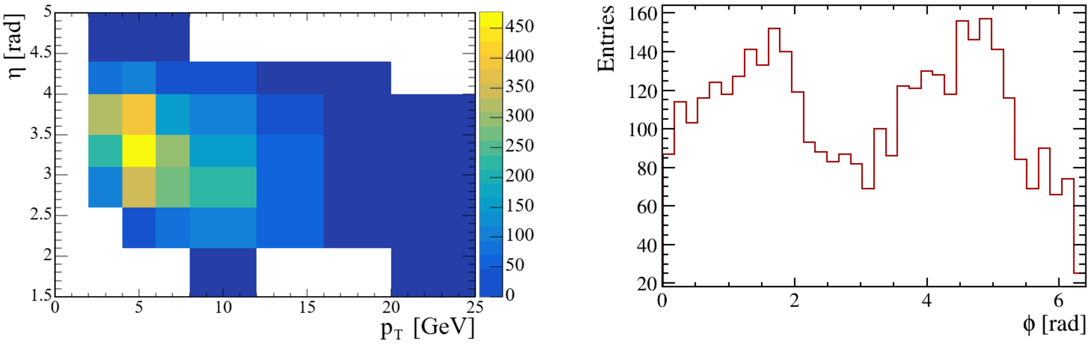

(a) *2D plot of $p_T - \eta$ variables. The binning is chosen in order to provide a similar number of events in each bin.*

(b) *Distribution of the ϕ angle. 36 bins are used.*

Figure 35: *The distributions of the D^{*+} used as input for the RapidSim simulation of the brem 0 category are shown. The dataset used consists of 3905 events.*

RapidSim allows to provide smearing for the momentum p distributions and for the impact parameter IP distributions. Hereafter the focus is placed on the p-distribution, since the IP-smearing was not observed to have a large impact on the invariant-mass output distributions. Thus only the p-smearing was applied. The solution chosen for the hadrons, *i.e.* the slow pion π_s^+ from the D^{*+} decay and the final state particles π^+ and K^-, is the former described, since their momentum resolution showed a Gaussian pattern. For each simulated event, the smearing is applied to the momentum as a shift (positive or negative), randomly extracted from the Gaussian distribution centered at 0 and with width determined by the provided function. More specifically, for each particle, the following steps were followed:

1. The dataset was divided into 5 (3) different sub-datasets for the brem 1 (0) category, according to the momentum value p, each containing approximately the same number of events;
2. For each sub-dataset, the distribution describing the smearing of the momentum, i.e. $\frac{p-p_{true}}{p_{true}}$, was considered;
3. Each sub-dataset was fitted with a Gaussian distribution. The fitted sigma value and its error were extracted and associated to the mean value of the p-range;
4. Finally, a `TGraphError` is constructed considering the extracted sigmas and the momentum ranges.

The resolution functions provided to RapidSim are reported separately for π_s^+, K^- and π^+ in Fig. 36, Fig. 37 and Fig. 38 for brem 1 category and in Fig. 39, Fig. 40 and Fig. 41 for brem 0 category, respectively. Appendix E contains the distributions used to evaluate the resolution together with the fit results for all the particles mentioned above.

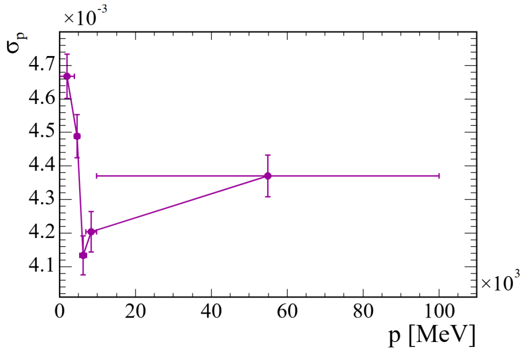

Figure 36: *TGraph representing the resolution associated to each momentum range for the π_s^+, brem 1 category.*

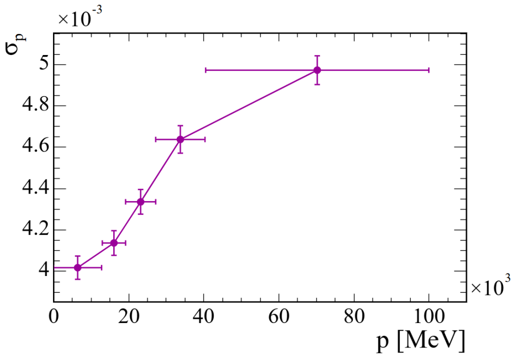

Figure 37: *TGraph representing the resolution associated to each momentum range for the K^-, brem 1 category.*

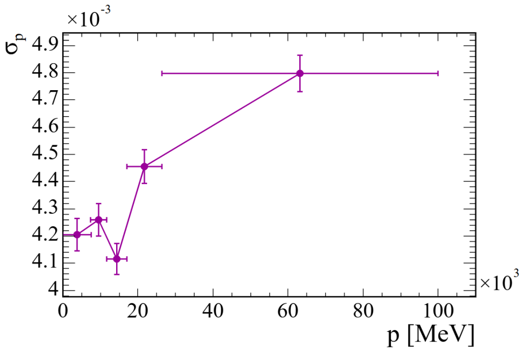

Figure 38: *TGraph representing the resolution associated to each momentum range for the π^+, considering brem 1 category.*

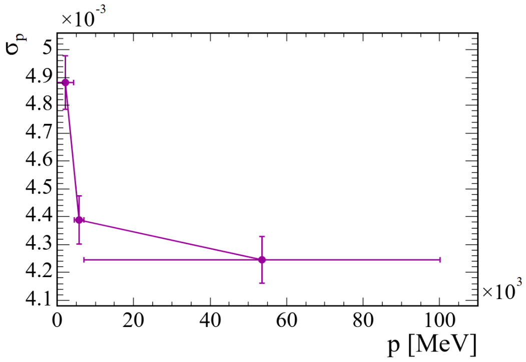

Figure 39: *TGraph representing the resolution associated to each momentum range for the π_s^+, considering brem 0 category.*

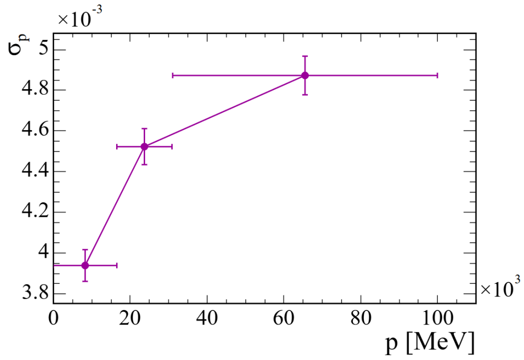

Figure 40: *TGraph representing the resolution associated to each momentum range for the K^-, considering brem 0 category.*

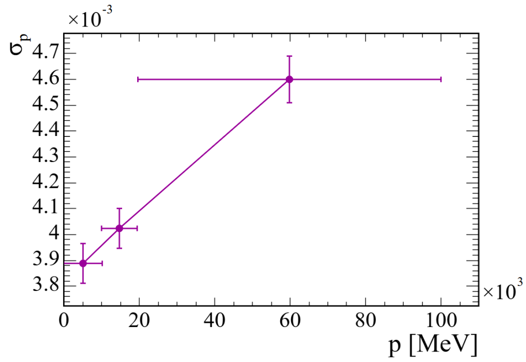

Figure 41: *TGraph representing the resolution associated to each momentum range for the π^+, considering brem 0 category.*

3.4.8 Leptons' setup

Leptons are treated similarly to hadrons, since a smearing option is also provided. However, in this case, recalling that electrons can emit bremsstrahlung radiation, the distributions for the smearing are not Gaussian, showing asymmetric tails that need to be taken into account. Consequently, for electrons, the second approach based on histograms and described in the previous Section is followed.

For both the leptons, e^- and e^+, the histograms of $\sigma_p = \frac{p-p_{true}}{p_{true}}$ are provided as input for RapidSim. In Fig. 42 and Fig. 43 one can observe the distributions for the brem 1 and brem 0 category respectively.

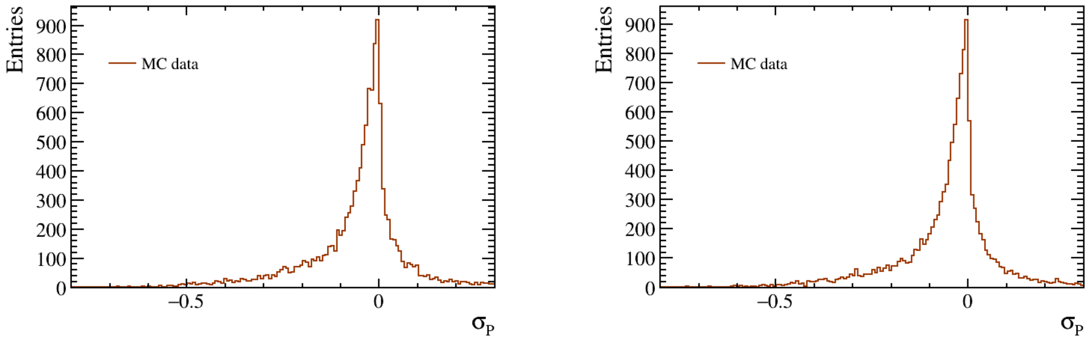

(a)

(b)

Figure 42: *Smearing histograms for positron (a) and electron (b), brem 1 category.*

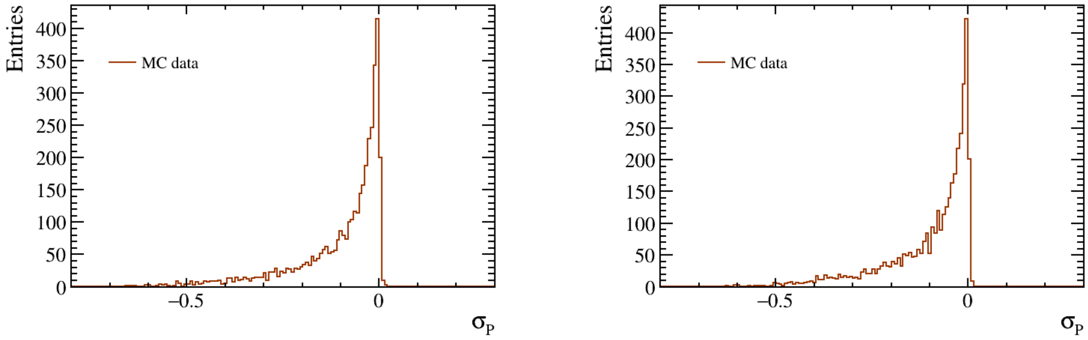

(a)

(b)

Figure 43: *Smearing histograms for positron (a) and electron (b), brem 0 category.*

3.4.9 Validation

Once all the previously explained steps are performed to set the input information in RapidSim, simulated events can be generated. The generation is run separately for brem categories and considering all the different decay modes, according to Sec. 3.4.4. Once all channels are produced, data are merged in a unique dataset, consisting in $\sim 6 \times 10^6$ events for each brem category. These datasets are compared with the official LHCb simulation, filtered for brem 0 or brem 1. For the validation only the dilepton mass region within $[675, 875]$ MeV is considered, corresponding to $\sim 2.7 \times 10^6$ events. In Fig. 44a and Fig. 44b it is possible to observe the comparison between the RapidSim generation and the official LHCb simulated sample for the D^0 invariant-mass distributions for brem 1 and brem 0 categories, respectively. As an example, the distributions for the dilepton invariant mass are also reported in Fig. 45a and Fig. 45b. This variable is of interest as it is the one used to divide the dataset. The agreement between the official LHCb simulation and the generated RapidSim samples is excellent. In addition, the distributions of several kinematic variables, as m, p, p_T, η and ϕ, and the topological variable IP were compared to ensure the validity of the simulation. Their plots are reported in Appendix F and Appendix G, respectively for brem 1 and brem 0 categories. Also in this case, a good agreement has been achieved.

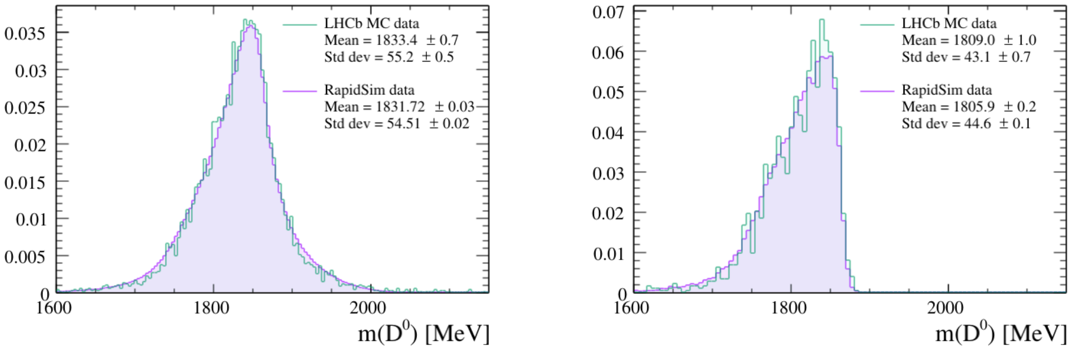

(a) D^0 *invariant mass distribution for the brem 1 category.*

(b) D^0 *invariant mass distribution for the brem 0 category.*

Figure 44: *The normalized distributions of the invariant mass of the* D^0 *meson are shown. In purple, the distribution obtained from the simulation with RapidSim, compared with the official dataset in green. Both brem categories are validated, brem 1 (a) and brem 0 (b).*

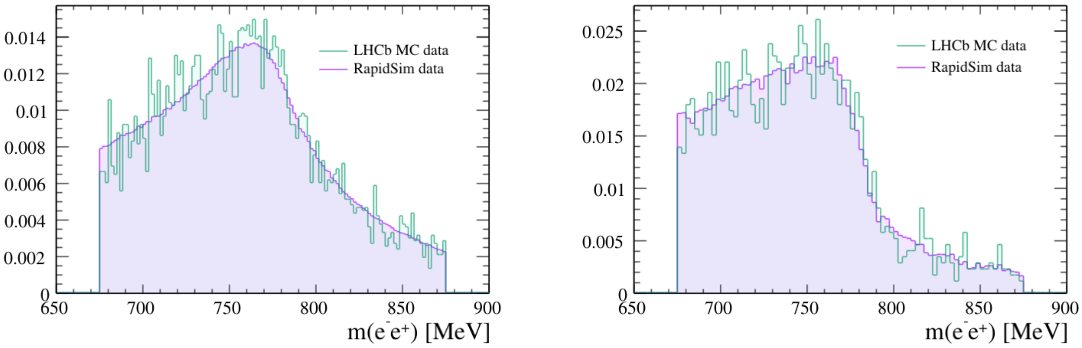

(a) *Dilepton mass distribution for brem 1.*

(b) *Dilepton mass distribution for brem 0.*

Figure 45: *The normalized distributions of the dilepton invariant mass* $m(e^-e^+)$ *are shown for brem 1 (a) and brem 0 (b) categories. The application of the dilepton filter (*$m(e^-e^+) \in [675, 875]$*) MeV is evident. It is possible to observe the peak around* $775/780$ *MeV due to the* ρ/ω *resonances.*

3.5 Fit model for $D^0 \to K^-\pi^+e^-e^+$ data

The evaluation of the branching ratio requires an estimate of the number of events for the decay under study, as expressed in Eq. (47). The yield for each channel (signals and normalization) is obtained via a maximum likelihood fit to the D^0 mass candidates distribution. The fits are performed independently for brem categories and for dilepton mass regions. As far as what concerns the normalization channel, its branching ratio is available from the BaBar measurement [57] only in the dilepton mass region $[675, 875]$ MeV, thus the yield for this channel is evaluated in this specific region.

To extract the yield, a fit is performed to the data samples. To improve the fit stability it is necessary to constrain some parameters to be able to recognize the signal and background events. For this reason, a preliminary study on the signal and background sources is performed, using the official LHCb simulation - if available - or the data samples simulated with RapidSim. Besides the signal $D^0 \to K^-\pi^+e^-e^+$, the data sample is expected to be constituted of several sources of background:

- Combinatorial background, due to tracks of particles that are randomly combined together and emulate the signal event topology;
- Partially reconstructed background, which is caused by the failure of the detector in the reconstruction of one or more particles of the decay, thus the reconstructed invariant mass is lower than expected and for this reason this background dominates the low mass region of the D^0 invariant mass distribution;
- Mis-identified background, characterized by a mis-identification of one or more particles.

It is worth noting that all these sources of background can in principle be present in both brem categories but they have different impact on the final fit. More specifically, the mis-identified background is extremely relevant for brem 0 category, while it's not for the brem 1. Indeed, the mis-identification of a π into an electron is more unlikely if one requires the association to that particle of a photon emitted by bremsstrahlung radiation, recalling that the probability for a pion to emit a photon is well below the probability of an electron to do so. Consequently, the mis-identified background in this analysis is considered only for brem 0 category, even if it will be further studied and constrained also in the brem 1 fit. As far as the partially reconstructed background is concerned, the constraints are set only in the brem 1 category and not considered in the brem 0 one where it is much less relevant. Finally, the combinatorial background is present in both categories.

Hereafter, the fit on simulated samples for the signal and background studies and the final fit to data are reported. The samples analyzed corresponds to data of all *blocks* (besides 3 and 4), requiring the dilepton invariant mass to be in the $[675, 875]$ MeV region. Datasets are divided according to brem category and trigger line selection, for the reasons explained above. Also simulated samples (both RapidSim one and official LHCb one) are filtered for the di-lepton invariant mass in $[675, 875]$ MeV region.

3.5.1 Brem 1 data

Fit models The signal model, already studied in the context of the BDT optimization, is taken from the official LHCb sample. It is described by a Johnson probability density function (PDF), introduced in Eq. (50) and characterized by four parameters: mean, sigma, gamma, and delta. The fitted distribution was shown in Fig.31, and the parameter values were reported in Tab. 6.

To understand the model of the partially reconstructed background, different decays that could eventually emulate the signal were reproduced via RapidSim:

- $D^0 \to K^-\pi^+e^-e^+\gamma$,
- $D^0 \to K^-\pi^+\pi^-e^+\nu_e$,
- $D^0 \to K^-\pi^+e^-e^+\pi^0$,
- $D^0 \to K^-\pi^+\pi^0$,
- $D^0 \to K^-\pi^+\pi^0\pi^0$,
- $D^0 \to K^-\pi^+\pi^0\pi^0\pi^0$,
- $D^0 \to K^-\pi^+\pi^-\pi^+\pi^0$,

Among all the above reported decays, only the first 2 listed were observed to be characterized by a reconstructed invariant mass in the relevant region for this analysis, specifically $D^0 \to K^-\pi^+e^-e^+\gamma$, where the photon γ is not reconstructed, and $D^0 \to K^-\pi^+\pi^-e^+\nu_e$, where the π^- is mis-identified as electron and the neutrino involves missing energy. Thus, only their fit are performed and reported respectively in Fig. 46a and Fig. 46b. The fitting function is a Bukin PDF [66] in both cases. This function is described by five parameters: mean (μ) and width (σ) of the peak, asymmetry between the tails ($asymm$) and widths of the tails (ρ_L and ρ_R).

Since these two decays show similar distributions, only one Bukin PDF is considered in the fit to data to describe the partially reconstructed background. The parameters' results for the $D^0 \to K^-\pi^+e^-e^+\gamma$ are reported in Tab. 9.

Fit results The model for brem 1 category consists of:

- Johnson PDF for the signal, whose tail parameters are fixed from the previous study for the optimization of the BDT cut;

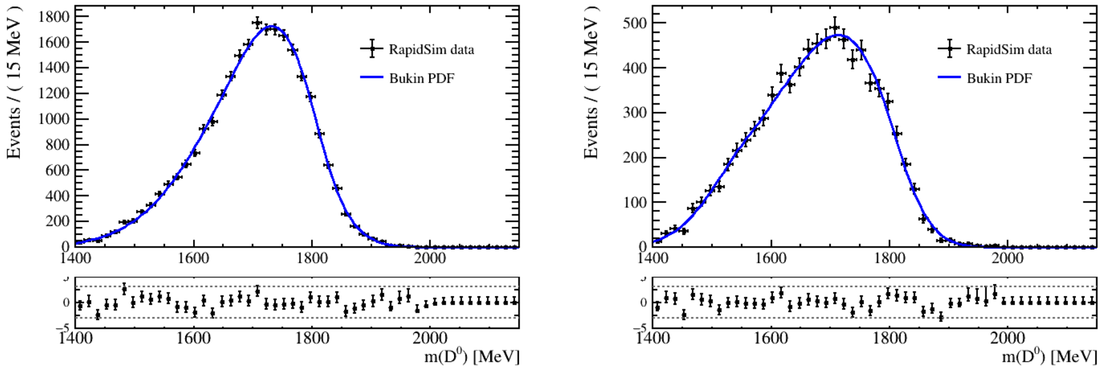

(a) *The D^0 invariant mass for the $D^0 \to K^-\pi^+e^-e^+\gamma$ decay is shown. The γ is not reconstructed.*

(b) *The D^0 invariant mass for the $D^0 \to K^-\pi^+\pi^-e^+\nu_e$ decay is shown. The ν_e is missed and the negative pion π^- is misidentified and reconstructed as an electron.*

Figure 46: *The invariant mass distribution of the D^0 meson for 2 channels is reported. Data points (in black) are produced by means of RapidSim, while the fit is performed with a Bukin PDF and displayed in blue.*

Bukin parameters	Fit results
μ	1731.5 ± 1.5
σ	85.7 ± 0.8
$asymm$	-0.191 ± 0.014
ρ_L	-0.39 ± 0.05
ρ_R	-0.70 ± 0.09

Table 9: *Parameters' results of the brem 1 partially reconstructed background $D^0 \to K^-\pi^+e^-e^+\gamma$, reproduced via RapidSim and filtered for dilepton mass bin $m(e^-e^+) \in [675, 875]$ MeV.*

- Bukin PDF, describing the partially reconstructed background, for which all the parameters are constrained;
- a first order polynomial for the combinatorial background, described by one parameter (left free to vary).

The extended maximum likelihood fits to data are shown in Fig. 47a, Fig. 47b and Fig. 47c, respectively for the `AND`, `Only E` and `TrackMVAs` decision. The fit results are reported in Tab. 10. It is noteworthy that for the `TrackMVAs` trigger line selection the partially reconstructed background is not present since it is overwhelmed by the combinatorial one and its addition makes the fit unstable.

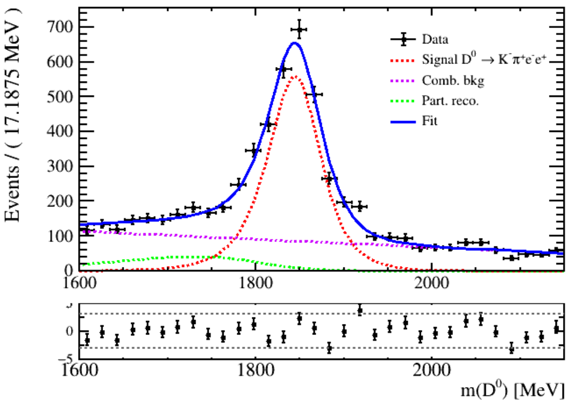

(a) `AND` trigger line.

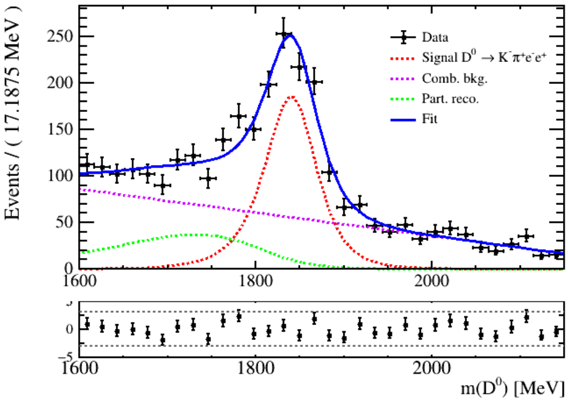

(b) `Only E` trigger line.

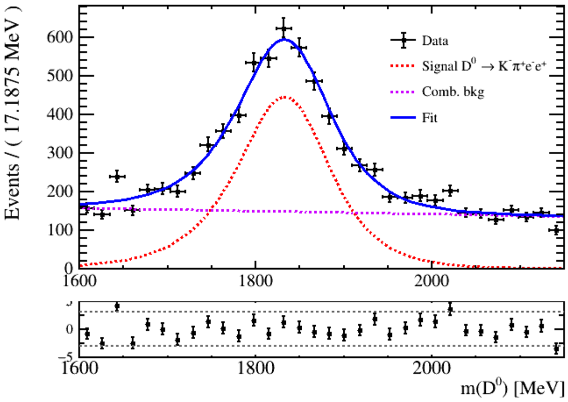

(c) `TMVAs` trigger line.

Figure 47: *Fit to brem 1 data. The total fit in blue is composed of three components: the signal in red, the partially reconstructed background in green (not present in the* `TMVAs` *trigger line), and the combinatorial background in purple.*

	`AND`	`Only E`	`TrackMVAs`
μ_{sig}	1848.6 ± 1.0	1844 ± 2	1840.3 ± 1.6
σ_{sig}	47.3 ± 1.7	46 ± 3	83 ± 4
γ_{sig}	0.20 [C]	0.20 [C]	0.20 [C]
δ_{sig}	1.42 [C]	1.42 [C]	1.42 [C]
μ_{bkg}	1731.5 [C]	1731.5 [C]	-
σ_{bkg}	85.7 [C]	85.7 [C]	-
$asymm_{bkg}$	-0.191 [C]	-0.191 [C]	-
$\rho_{L,bkg}$	-0.39 [C]	-0.39 [C]	-
$\rho_{R,bkg}$	-0.70 [C]	-0.70 [C]	-
c_{comb}	-0.38 ± 0.06	-0.67 ± 0.06	-0.07 ± 0.03
n_{sig}	2729 ± 79	889 ± 53	3771 ± 143
n_{comb}	2647 ± 147	1643 ± 109	4712 ± 146
$n_{part.\ reco}$	449 ± 123	404 ± 96	-

Table 10: *Fit results for the $D^0 \to K^-\pi^+e^-e^+$ decay, brem 1 category. Parameters signed with [C] are set to the value reported in the table during the fit.*

3.5.2 Brem 0 data

Fit models The study of the signal model for brem 0 category is performed using a sample produced via RapidSim. The official simulation is reproduced with the RapidSim framework due to the low available statistics of the brem 0 category sample once also the di-lepton filter is applied. The fitting function is a double-sided Crystal ball PDF, Eq. (51) [67], described by 7 parameters: mean of the gaussian peak (μ) and two sigmas corresponding to the widths of the Gaussian component on both sides (σ_R and σ_L); location of transition to a power law in standard deviations away from the mean (α_L and α_R) and exponent of the power-law tail (n_L and n_R) for both the left and right tails.

$$f(m;\,\mu,\sigma_L,\alpha_L,n_L,\sigma_R,\alpha_R,n_R) = \begin{cases} A_L\left(B_L - \frac{m-\mu}{\sigma_L}\right)^{-n_L}, & \text{for } \frac{m-\mu}{\sigma_L} < -\alpha_L, \\ \exp\left(-\frac{1}{2}\left[\frac{m-\mu}{\sigma_L}\right]^2\right), & \text{for } \frac{m-\mu}{\sigma_L} \leq 0, \\ \exp\left(-\frac{1}{2}\left[\frac{m-\mu}{\sigma_R}\right]^2\right), & \text{for } \frac{m-\mu}{\sigma_R} \leq \alpha_R, \\ A_R\left(B_R + \frac{m-\mu}{\sigma_R}\right)^{-n_R}, & \text{otherwise,} \end{cases} \tag{51}$$

where $A_i = \left(\frac{n_i}{|\alpha_i|}\right)^{n_i} \exp\left(-\frac{\alpha_i^2}{2}\right)$ and $B_i = \frac{n_i}{|\alpha_i|} - |\alpha_i|$.

The fit to the simulated sample is shown in Fig. 48 and the obtained parameters are reported in Tab. 11.

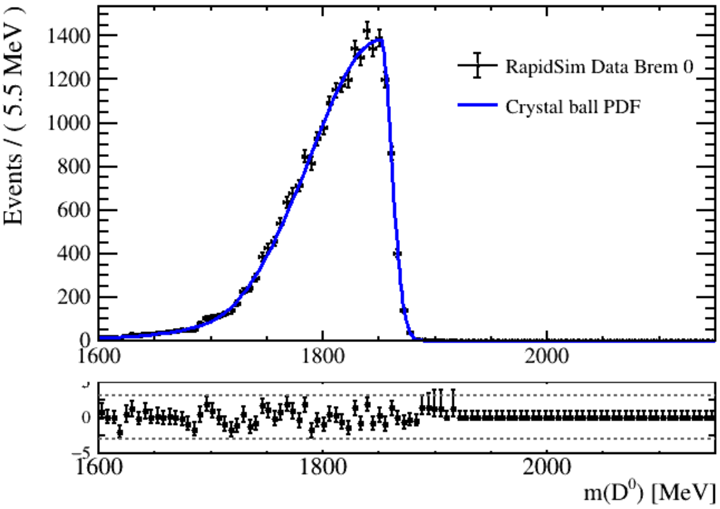

Figure 48: *The signal for* $D^0 \to K^-\pi^+e^-e^+$ *channel is displayed. The* D^0 *invariant mass distribution is fitted with a double-sided Crystal ball PDF.*

Double-sided crystal ball parameters	Fit results
μ	1851.3 ± 0.4
σ_L	63.7 ± 0.5
σ_R	9.8 ± 0.3
α_L	2.07 ± 0.08
n_L	3.0 ± 0.9
α_R	4.47 ± 0.13
n_R	0 [C]

Table 11: *Parameters of the brem 0 signal PDFs evaluated on RapidSim generated samples of* $D^0 \to K^-\pi^+e^-e^+$*, brem 0, filtered for dilepton mass bin* $m(e^-e^+) \in [675, 875]$ *MeV.*

As already explained, in this case is not yet possible to study the partially reconstructed background since it is overwhelmed by the mis-id one. In addition, the analysis of the mis-ID background from $D^0 \to K^-\pi^+\pi^-\pi^+$ decays requires a dedicated approach since the application of PID requirements distorts the D^0 mass distribution.

The PIDCalib2 package PID variables are evaluated by exploiting information from the RICH, ECAL and MUON detectors, and their performance depends on the particles' kinematics. Applying a PID cut to data alters the kinematic distributions of the particles, introducing a deformation in the invariant mass reconstructed under a different child particles mass hypothesis.

The PIDCalib2 package stands for "Particle IDentification Calibration" and is a set of tools helping in the computation of the efficiency of particle identification selection requirements. It is based on a data-driven approach because of the difficulties in simulating the detector PID response, which depends on several factors as the kinematics of the particles, the detector occupancy and alignments [68].

More into details, the aim of PIDCalib2 is to provide efficiency histograms for a specific PID requirement. However, to compute the efficiencies, it is necessary to know the number of signal events before and after the PID selection cut. Some decays, such as the $D^{*+} \to D^0(\to K^-\pi^+)\pi_s^+$ mode, can be correctly identified thanks to their particular topology without the need to apply PID requirements. These decays serve as ideal calibration samples to evaluate the PID efficiency. In addition, the PID response for particles is non-uniform and it is known to vary as a function of several variables, among the others the most important are the momentum p, the pseudorapidity η and the number of tracks N_{tracks} [68]. Therefore, assuming to have an available data sample obtained without the use of PID information, and assuming that the PID response can be fully parametrized by a set of variables (e.g. the momentum p), the sample is divided in sub-samples (where the PID variable does not vary significantly) and the efficiency ε_i is evaluated as

$$\varepsilon_i = \frac{N_{pass}}{N_{total}}, \tag{52}$$

where N_{total} is the total number of events in the subset before the PID cut is applied and N_{pass} is the number of events satisfying the PID requirement [68].

This way PIDCalib2 allows to obtain 3D efficiency histograms in bins of p, η and N_{tracks} that can be used to evaluate the PID efficiency on any given sample.

Since the effect of application of PID requirements is not reproduced well by RapidSim, an approach based on PIDCalib2 was developed to overcome this limitation. The following strategy is adopted:

1. Production of the sample $D^0 \to K^-\pi^+\pi^-\pi^+$ via RapidSim, requiring the misidentification of π^+ into e^+ and π^- into e^- (thus the reconstructed decay turns out to be $D^0 \to K^-\pi^+e^-e^+$);

2. Application of weights sampled from the PID efficiency maps produced by PIDCalib2 for the $\pi \to e$ mis-id probability to emulate the deformation of the D^0 mass under the $D^0 \to K^-\pi^+e^-e^+$ mass hypothesis due to the PID requirements.

The PIDcalib2 map applied in this analysis is produced with data of *block* number 8 from 2024 data and is reported in Fig. 49. It is a 2D map, in bins of p and η, and represents the $\pi \to e$ mis-id efficiency corresponding to the cut ”Delta Log Likelihood for the electron (DLL_e) greater than 3”. The DLLe is defined as $\log(\mathcal{L}_e) - \log(\mathcal{L}_\pi)$, where $\mathcal{L}$ is the likelihood for a track to be of a specific particle [69]. The efficiencies are applied to each generated event as weights. Specifically, in our case, we sample from the PIDCalib2 histograms the efficiency to the $\pi^+ \to e^+$ and $\pi^- \to e^-$. The efficiencies are extracted according to the values of momentum and pseudorapidity of the generated pions and the total efficiency for an event is evaluated as a product of these two. The distortion of the distribution after the application of the weights can be observed in Fig. 50, where the comparison between the original output sample provided by RapidSim and the modification introduced by the application of the weights is shown.

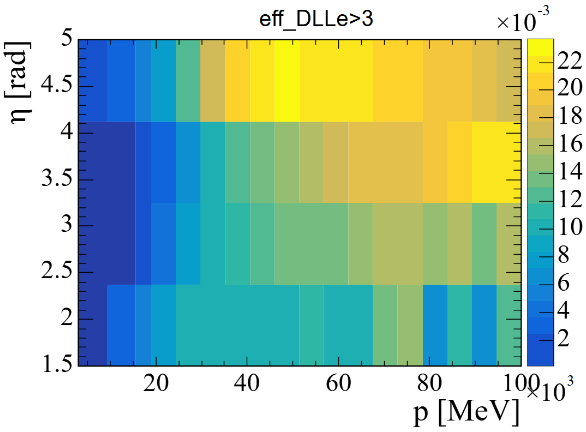

Figure 49: *2D plot showing the efficiency of the cut $DLL_e > 3$, according to the $p - \eta$ binning scheme.*

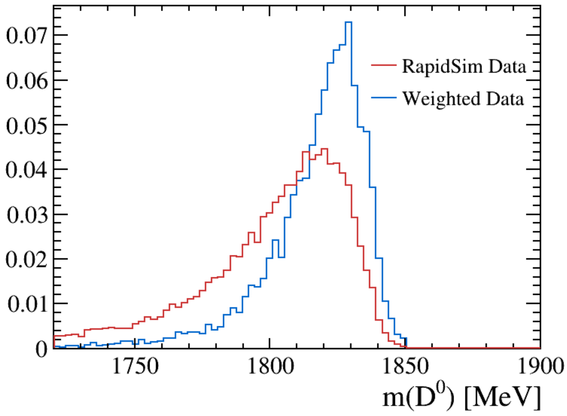

Figure 50: *The comparison between data simulated for the mis-id $D^0 \to K^-\pi^+\pi^-\pi^+$ decay produced via RapidSim (red) and after the PID map application (blue) is shown.*

The ”PID corrected” sample is fitted with a Bukin PDF [66]. The Bukin PDF is described by 5 parameters: position (μ) and width (σ) of the peak, grade of asymmetry of the peak ($asymm$) and tails parameters (ρ_L and ρ_R). The fit results are shown in Fig. 51 and the corresponding parameters are reported in Tab. 12.

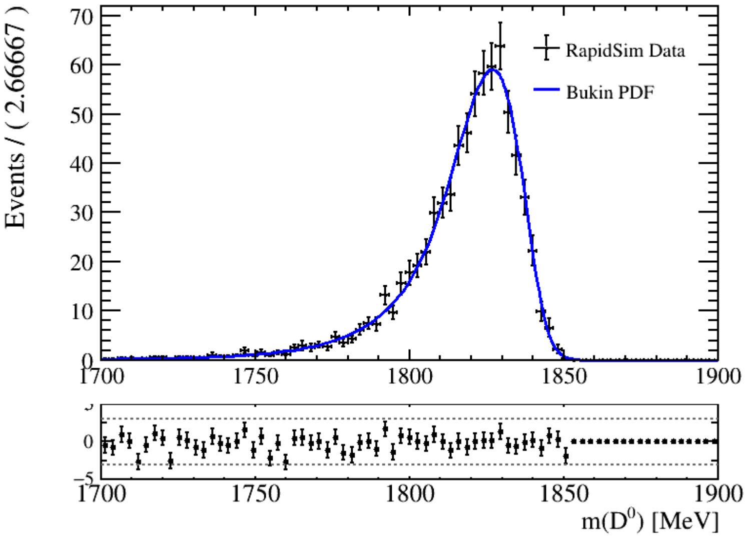

Figure 51: *The distribution of the D^0 invariant mass for the mis-identified background $D^0 \to K^-\pi^+\pi^-\pi^+$ reproduced via RapidSim is displayed. The fitting function is a Bukin PDF (blue).*

Bukin parameters	Fit results
μ	1826.8 ± 1.1
σ	12.2 ± 0.7
$asymm$	-0.21 ± 0.06
ρ_L	0.06 ± 0.02
ρ_R	-1.8 ± 1.2

Table 12: *Parameters' result of the brem 0 mis-id background $D^0 \to K^-\pi^+\pi^-\pi^+$, reproduced via RapidSim and filtered for dilepton mass bin $m(e^-e^+) \in [675, 875]$ MeV.*

Fit results The model for brem 0 category comprehends:

- double-sided crystal ball PDF for the signal, for which all parameters besides the mean of the gaussian are fixed;

- bukin PDF for the mis-identified background, fixing all parameters besides the position of the peak;
- a first order polynomial for the combinatorial background, described by one parameter left free to vary.

The extended maximum likelihood fits to brem 0 filtered data are shown in Fig. 52a, Fig. 52b and Fig. 52c, respectively for the `AND`, `Only E` and `TrackMVAs` trigger line decision. The fit results are reported in Tab. 13.

	`AND`	`Only E`	`TrackMVAs`
μ_{sig}	1861 ± 2	1856 ± 4	1852.6 ± 1.6
$\sigma_{L,sig}$	63.7 [C]	63.7 [C]	63.7 [C]
$\sigma_{R,sig}$	9.8 [C]	9.8 [C]	9.8 [C]
$\alpha_{L,sig}$	2.07 [C]	2.07 [C]	2.07 [C]
$n_{L,sig}$	3.0 [C]	3.0 [C]	3.0 [C]
$\alpha_{R,sig}$	4.47 [C]	4.47 [C]	4.47 [C]
$n_{R,sig}$	0.00 [C]	0.00 [C]	0.00 [C]
μ_{bkg}	1830 ± 0.3	1830 ± 0.7	1826 ± 0.4
σ_{bkg}	12.2 [C]	12.2 [C]	12.2 [C]
$asymm$	-0.21 [C]	-0.21 [C]	-0.21 [C]
$\rho_{L,bkg}$	0.06 [C]	0.06 [C]	0.06 [C]
$\rho_{R,bkg}$	-1.8 [C]	-1.8 [C]	-1.8 [C]
c_0	-0.64 ± 0.07	-0.79 ± 0.09	-0.18 ± 0.07
n_{sig}	412 ± 47	76 ± 24	642 ± 58
n_{comb}	514 ± 29	176 ± 17	825 ± 36
n_{misID}	2900 ± 66	452 ± 28	1869 ± 61

Table 13: *Fit results for the $D^0 \to K^-\pi^+e^-e^+$ decay, brem 0 category. Parameters signed with [C] are constrained during the fit.*

3.5.3 Results

The measured signal yields obtained by means of maximum likelihood fits performed on data for both bremsstrahlung categories are reported in Tab. 14. It is worth noting that the newly implemented trigger line on electrons provide an additional $\sim 10\%$ of signal events.

Considering that the final analysis aims to observe rare channels, we performed a preliminary back-of-the-envelope calculation using the normalization channel to estimate the yield of signal events also for the rare decays, by means of a comparison

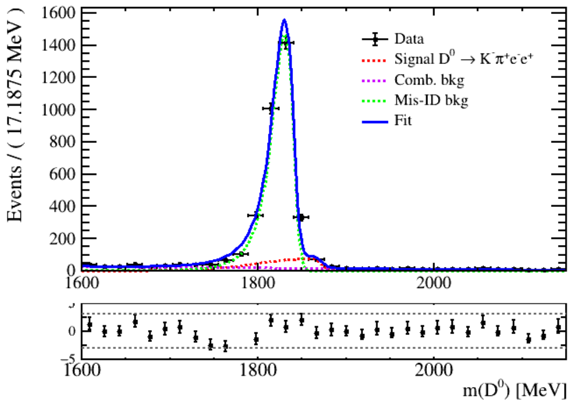

(a) *AND trigger line.*

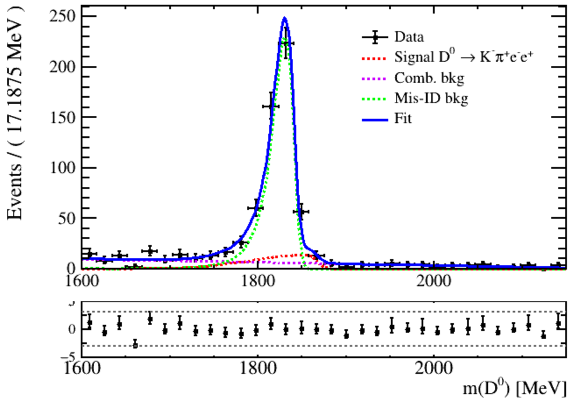

(b) *Only E trigger line.*

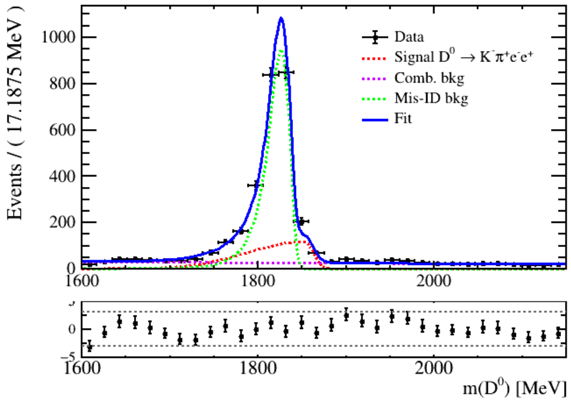

(c) *TMVAs trigger line.*

Figure 52: *Fit to brem 0 data. The total fit in blue is composed of three components: the signal in red, the mis-identified background in green and the combinatorial background in purple.*

$\boldsymbol{D^0 \to K^-\pi^+e^-e^+}$				
Number of signal events				
	`AND`	`Only E`	`TrackMVAs`	TOTAL
brem 1	2729 ± 79	889 ± 53	3771 ± 143	7389 ± 172
brem 0	412 ± 47	76 ± 24	642 ± 58	1130 ± 78

Table 14: *Yield results for the normalization channel* $D^0 \to K^-\pi^+e^-e^+$.

with Run 2 [35] results. In this context, we recall that the final analysis will employ - in addition to the selection described in this thesis - also a dedicated BDT for each rare channel. To cancel systematic uncertainties in the ratio of branching fractions, the same BDTs will be applied to the normalization channel too.

In particular, in order to compare with Run 2 results, it is necessary to have a similar background level. Therefore, we applied a tighter selection than the one described in this thesis to brem 1 data to achieve a similar background level as in the Run 2 analysis, obtaining ~ 2500 signal events for an integrated luminosity of ~ 5.1 fb^{-1}, thus ~ 500 events/fb^{-1} in the dilepton region dominated by ρ/ω resonances, $m(e^-e^+) \in [675, 875]$ MeV. For reference, the Run 2 analysis [35] yielded about ~ 465 events with ~ 4 fb^{-1} of data, i.e. ~ 120 events/fb^{-1} in the same region. This implies that we expect a factor of ~ 4 increase in the number of events per unit of integrated luminosity.

Assuming Lepton Flavor Universality,

$$\mathcal{B}(D^0 \to h^-h^+e^-e^+) \approx \mathcal{B}(D^0 \to h^-h^+\mu^-\mu^+), \tag{53}$$

and according to the results from the analysis of the muonic channels performed by the LHCb collaboration [36],

$$\frac{\mathcal{B}(D^0 \to \pi^-\pi^+\mu^-\mu^+)}{\mathcal{B}(D^0 \to K^-\pi^+\mu^-\mu^+)} \approx 0.23, \tag{54}$$

$$\frac{\mathcal{B}(D^0 \to K^-K^+\mu^-\mu^+)}{\mathcal{B}(D^0 \to K^-\pi^+\mu^-\mu^+)} \approx 0.04, \tag{55}$$

we can predict the expected number of events for the rare channels, provided that the three decay modes have roughly comparable reconstruction and selection efficiencies, which is approximately the case. In conclusion, we expect ~ 120 events/fb^{-1} signal events for the $D^0 \to \pi^-\pi^+e^-e^+$ channel and ~ 20 events/fb^{-1} signal events for the $D^0 \to K^-K^+e^-e^+$ one. This means that considering the dataset used in this thesis, corresponding to a integrated luminosity of 5.1 fb^{-1}, we expect

$$\begin{aligned} &\sim 600 \text{ events for } D^0 \to \pi^-\pi^+e^-e^+, \\ &\sim 100 \text{ events for } D^0 \to K^-K^+e^-e^+. \end{aligned} \tag{56}$$

Conclusions

Rare charm decays such as $D^0 \to \pi^-\pi^+e^-e^+$ and $D^0 \to K^-K^+e^-e^+$ are particularly promising in the search for possible contributions from New Physics, as they are dominated by loop diagrams where new particles or interactions could appear. A deviation of their measured branching fractions from Standard Model (SM) predictions would therefore provide a potential indication of physics beyond the SM. To access these channels, the decay $D^0 \to K^-\pi^+e^-e^+$ is employed as the normalization mode. This thesis reports the first analysis of this decay using data collected with the upgraded LHCb detector.

The analysis is based on proton–proton collision data recorded during Run 3 of the LHC in 2024, at a center-of-mass energy of $\sqrt{s} = 13.6$ TeV. The dataset corresponds to an integrated luminosity of 5.1 fb^{-1}. The dilepton region under study, $m(e^-e^+) \in [675, 875]$ MeV, was chosen to suppress contributions from combinatorial background and to match the di-lepton window for which the BaBar branching ratio measurement is available.

The analysis strategy focused primarily on optimizing the event selection in order to minimize background contamination. This was achieved through the application of selection requirements and the training of a Boosted Decision Tree (BDT). The data sample was further subdivided according to bremsstrahlung categories (depending on whether one or more photons were reconstructed and associated with the decay) and according to trigger selections, in order to enhance the overall optimization.

Background shapes required in the fit to data were studied with RapidSim, a fast simulation framework for heavy-hadron decays. The tool was first validated by tuning its input distributions and configuration parameters to reproduce official LHCb simulated samples. Once validated, the main background sources relevant to this analysis were generated and their fit models investigated. By constraining the shapes of signal and background models in the data analysis, the signal yield was extracted through unbinned maximum-likelihood fits to the invariant-mass distributions of D^0 candidates.

The measured yields of the signal channel in the dilepton region dominated by ρ/ω resonances, $m(e^+e^-) \in [675, 875]$ MeV, are 7389 ± 172 when at least one reconstructed photon is associated with the decay, and 1130 ± 78 when no photon is reconstructed.

Furthermore, the study of the normalization channel allowed a prediction of the expected yields for the rare decay modes, based on comparisons with LHCb Run 2 results. Under the assumption of lepton-flavour universality, the measured branching ratios of $D^0 \to h^+h^-\mu^+\mu^-$ decays can be used to estimate the yields expected in the 2024 dataset for the corresponding electron modes. For an integrated luminosity of 5.1 fb^{-1}, the expected yields are approximately 600 events for $D^0 \to \pi^-\pi^+e^-e^+$ and about 100 events for $D^0 \to K^-K^+e^-e^+$ in the ρ/ω-dominated region.

This work represents the first step towards the exploration of rare charm decays with Run 3 data, and the analysis will be further extended in forthcoming studies.

Acknowledgement

Per concludere questa tesi, vorrei ringraziare le persone che mi hanno accompagnato durante questo percorso.

Un sincero e profondo ringraziamento al Dott. Fabio Ferrari, alla Dott.ssa Marianna Fontana e al Dott. Alberto Bellavista, per la pazienza e la disponibilità dimostratami in questi mesi, per il tempo speso ad aiutarmi e per tutto ciò che mi è stato insegnato. Vorrei ringraziare anche tutto il gruppo LHCb di Bologna e in particolare il Prof. Angelo Carbone, per l'aiuto prezioso e non scontato.

Grazie alla mia mamma e al mio papà, per aver sempre creduto in me.
Grazie a Jack, per essere semplicemente Jack.
Grazie alla mia famiglia, enorme e caotica ma bellissima.
Grazie ai miei amici.
Infine, grazie a me :).

Appendix

A BDT variables: comparison between brem 1 and brem 0 categories

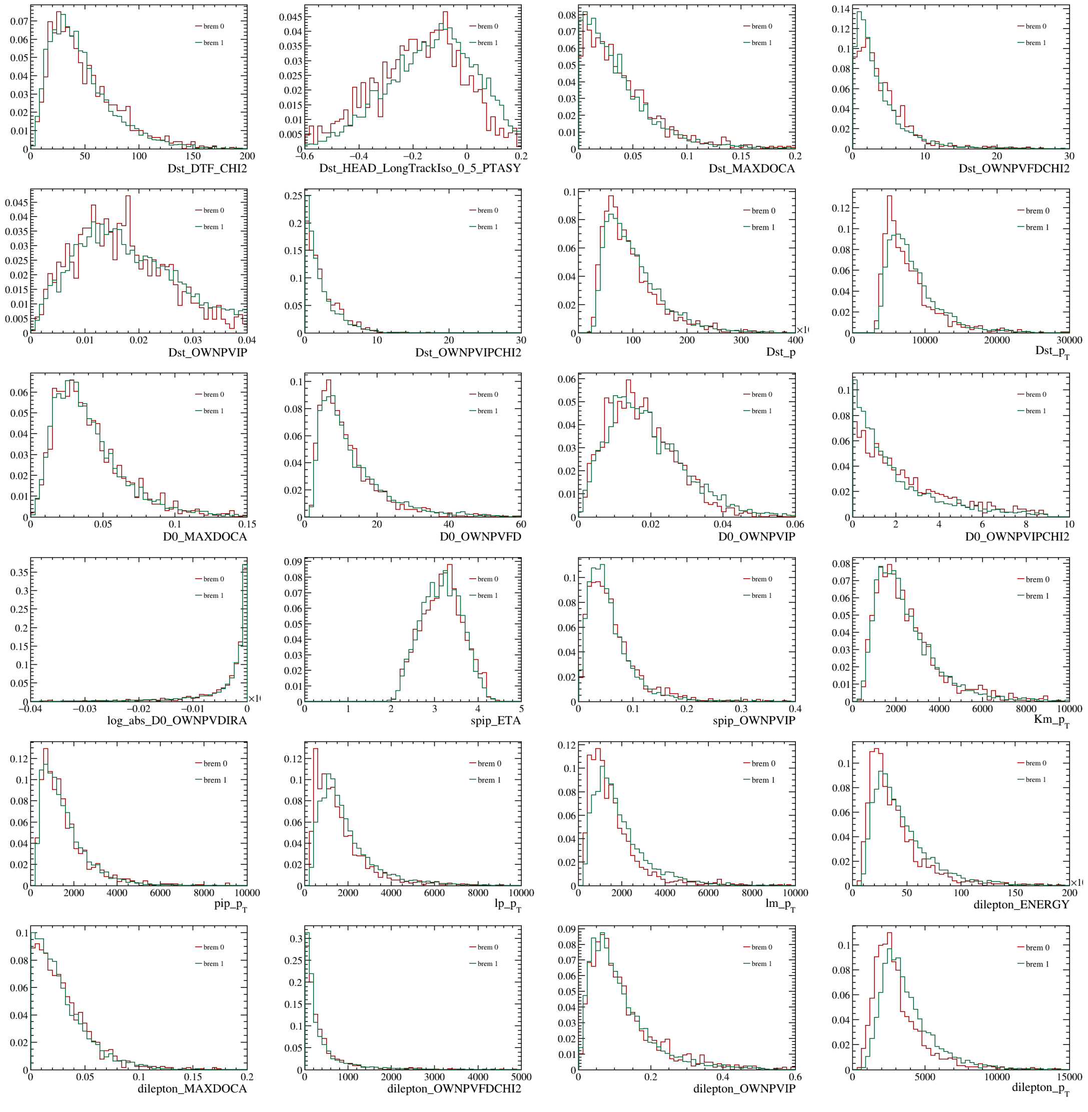

Figure 53: *Input variables for the BDT training. Comparison between brem 1 (green) and brem 0 (brown) distributions. The sample is not divided for trigger lines.*

B BDT variables: correlation with the D^0 mass

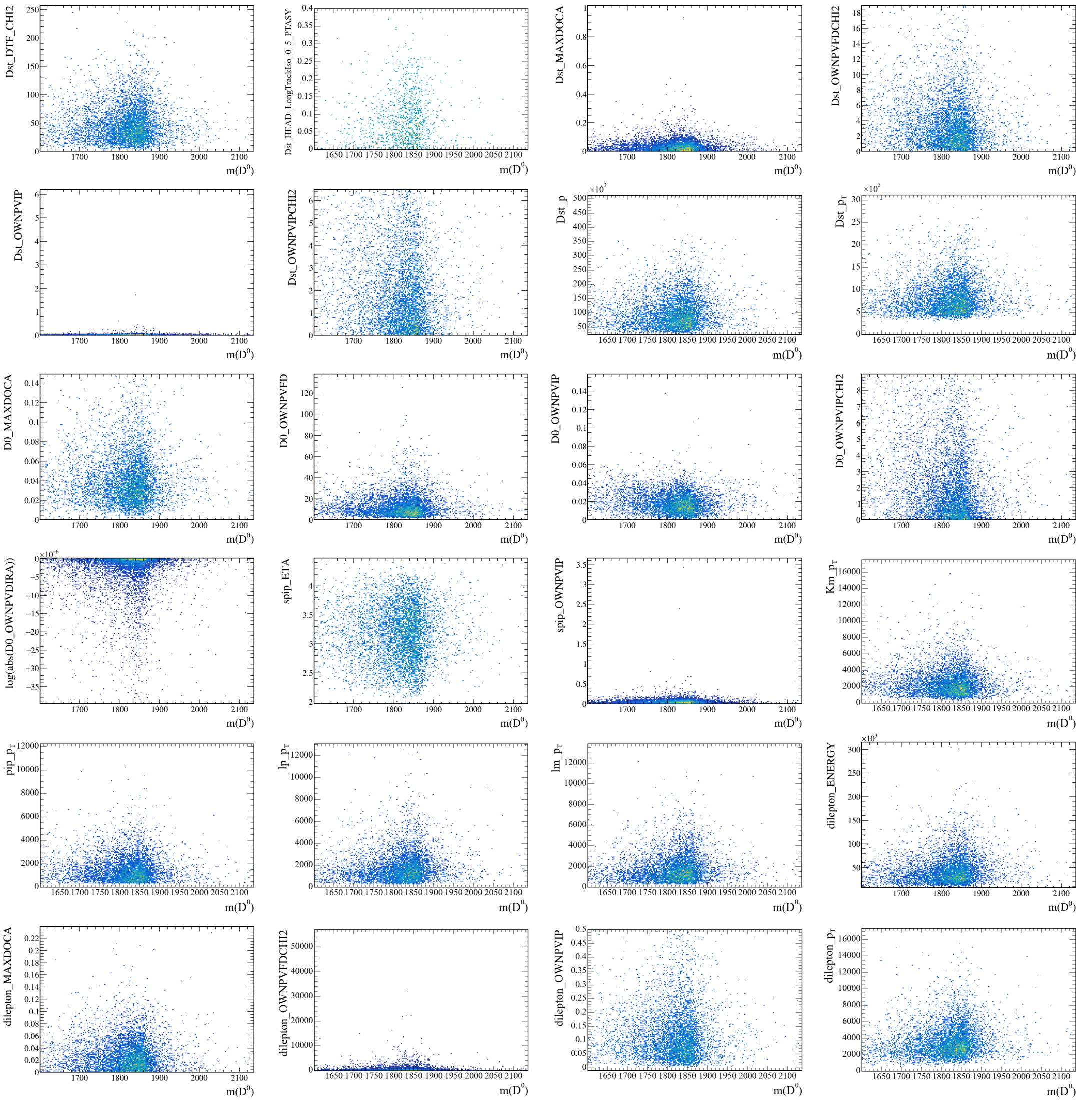

Figure 54: *Scatter plot of the input variables for the BDT training with respect to the D^0 mass. None of the variables show any correlation.*

C BDT variables: comparison between trigger lines

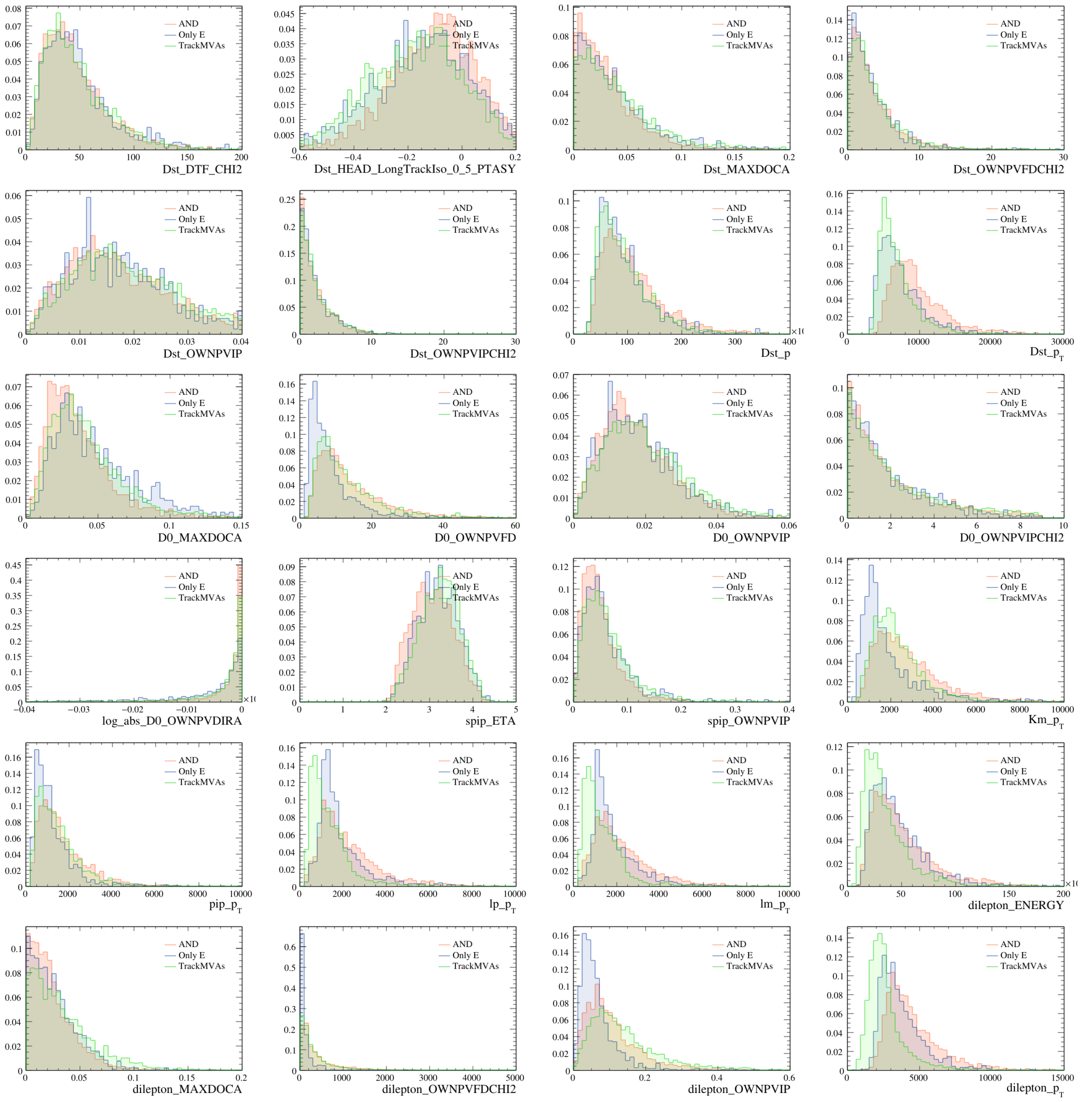

Figure 55: *Input variables for the BDT training. Comparison between trigger lines:* `AND` *in orange,* `Only E` *in blue and* `TrackMVAs` *in green.*

D Configuration files example

The decay file for the $D^0 \to K^-\pi^+e^-e^+$ decay proceeding without resonances is:

```
D*+ -> {D0 -> K- pi+ e+ e-} pi+
```

The configuration file used for the simulation reads:

```
acceptance : AllIn
geometry : LHCb
energy : 14
paramsDecaying : M, P, PT, eta, IP, phi
paramsStable : M, P, PT, eta, IP, phi
useEvtGen : TRUE
evtGenUsePHOTOS : TRUE
param : Kst_M M 3 4
param : Kst_M_TRUE M 3 4
param : Kst_P P 3 4
param : Kst_P_TRUE P 3 4
param : Kst_PT PT 3 4
param : Kst_PT_TRUE PT 3 4
param : Kst_eta eta 3 4
param : Kst_eta_TRUE eta 3 4
param : Kst_IP IP 3 4
param : Kst_IP_TRUE IP 3 4
param : Kst_phi phi 3 4
param : Kst_phi_TRUE phi 3 4
param : dilepton_M M 5 6
param : dilepton_M_TRUE M 5 6
param : dilepton_P P 5 6
param : dilepton_P_TRUE P 5 6
param : dilepton_PT PT 5 6
param : dilepton_PT_TRUE PT 5 6
param : dilepton_eta eta 5 6
param : dilepton_eta_TRUE eta 5 6
param : dilepton_IP IP 5 6
param : dilepton_IP_TRUE IP 5 6
param : dilepton_phi phi 5 6
param : dilepton_phi_TRUE phi 5 6
@0
        name : Dst
```

```
        evtGenModel : VSS
@1
        name : D0
        evtGenModel : PHSP
@2
        name : spip
        smear : spip
@3
        name : Km
        smear : Km
@4
        name : pip
        smear : pip
@5
        name : lp
        smear : lp
@6
        name : lm
        smear : lm
```

The decay file for the $D^0 \to K^-\pi^+e^-e^+$ decay proceeding via both ω and $\bar{K}^{*0}$ resonances is:

```
D*+ -> {D0 -> {K*0b -> K- pi+} {omega -> e+ e-}} pi+
```

The configuration file used for the simulation reads:

```
acceptance : AllIn
geometry : LHCb
energy : 14
paramsDecaying : M, P, PT, eta, IP, phi
paramsStable : M, P, PT, eta, IP, phi
useEvtGen : TRUE
evtGenUsePHOTOS : TRUE
@0
        name : Dst
        evtGenModel : VSS
@1
        name : D0
```

```
        evtGenModel : SVV_HELAMP 1.0 0.0 1.7 0.0 1.0 0.0
@2
        name : spip
        smear : spip
@3
        name : Kst
        evtGenModel : VSS
@4
        name : dilepton
        evtGenModel : VLL
@5
        name : Km
        smear : Km
@6
        name : pip
        smear : pip
@7
        name : lp
        smear : lp
@8
        name : lm
        smear : lm
```

E Details on hadrons’ setup

Fits to the hadrons’ sub-datasets with sigma (σ) and mean (μ) result displayed:

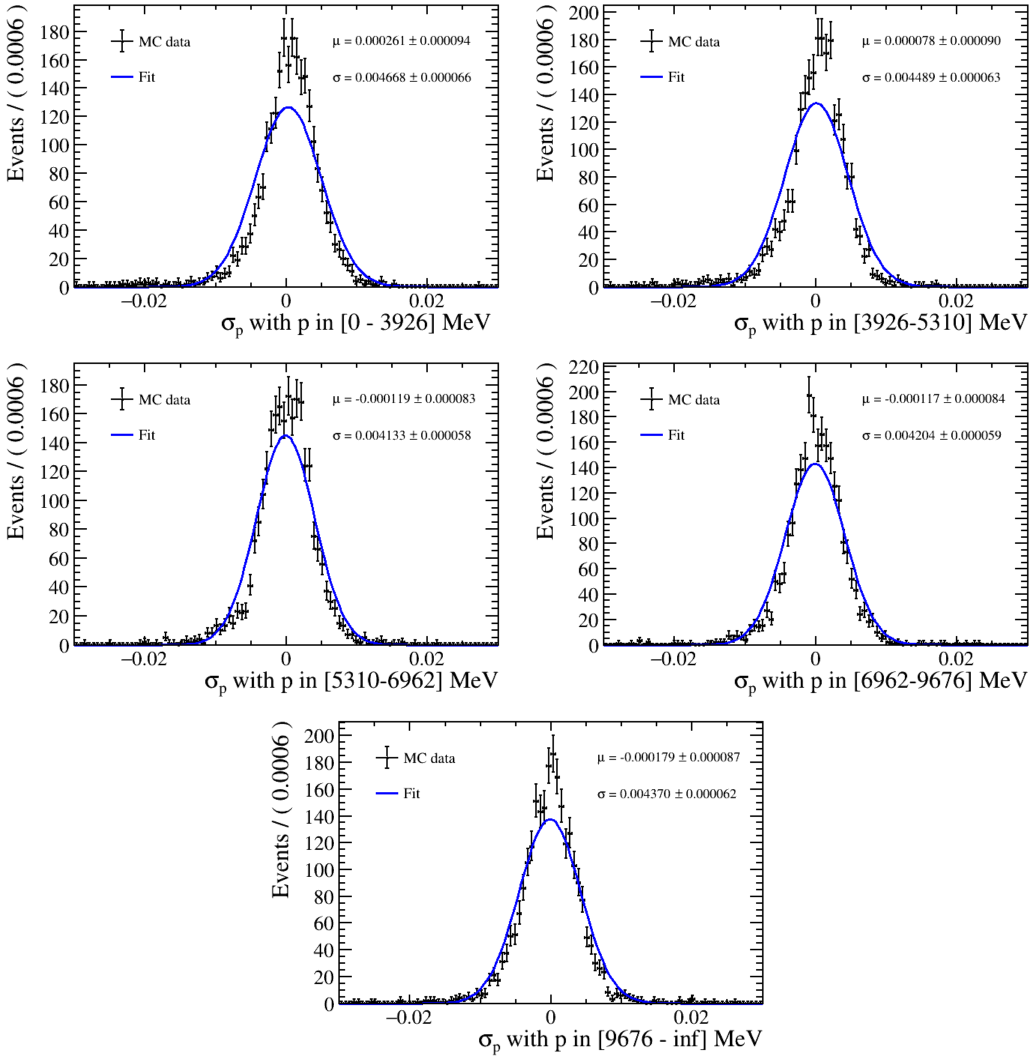

Figure 56: *Soft pion π_s^+ distributions for $\frac{p-p_{true}}{p_{true}}$, divided into 5 sub-datasets for the brem 1 category. Data points are in black, while the gaussian fit is displayed in blue.*

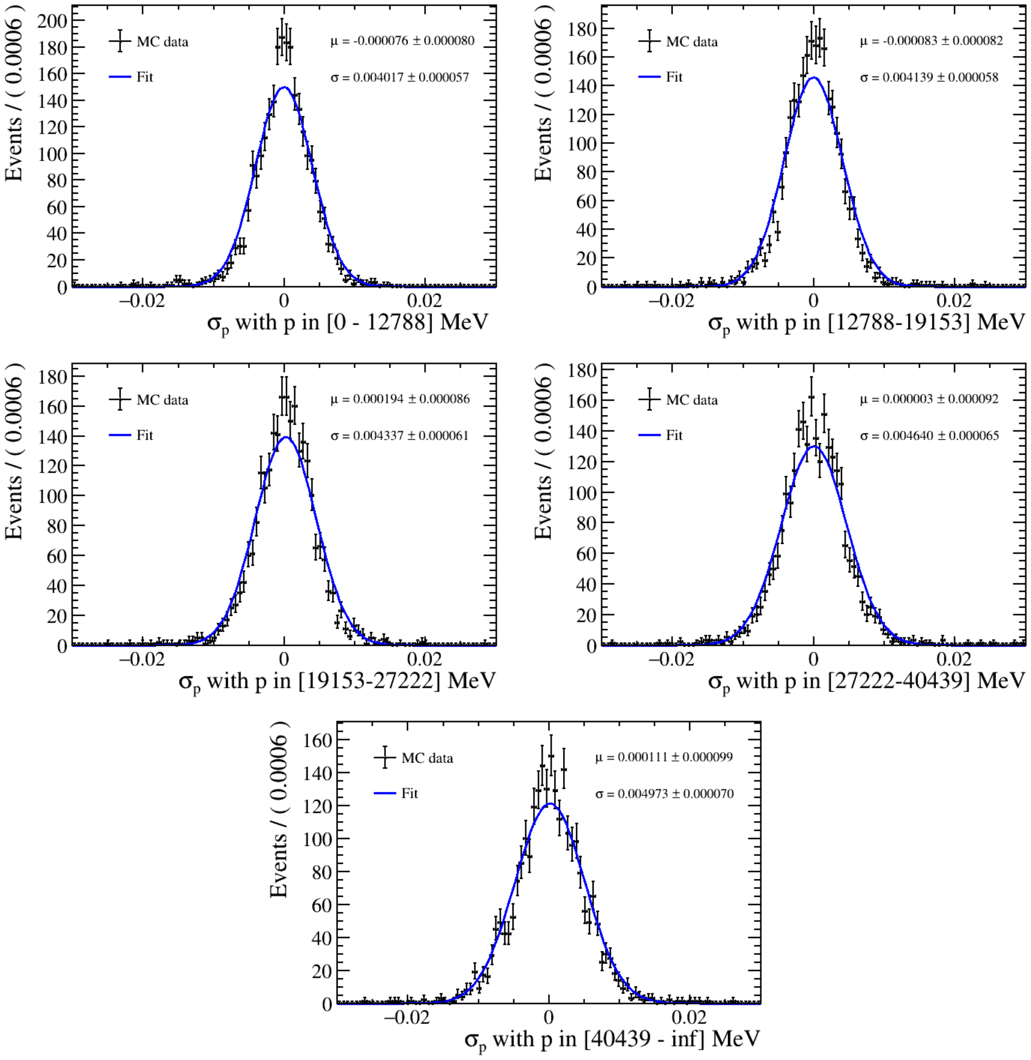

Figure 57: *Kaon K^- distributions for $\frac{p-p_{true}}{p_{true}}$, divided into 5 sub-datasets for the brem 1 category. Data points are in black, while the gaussian fit is displayed in blue.*

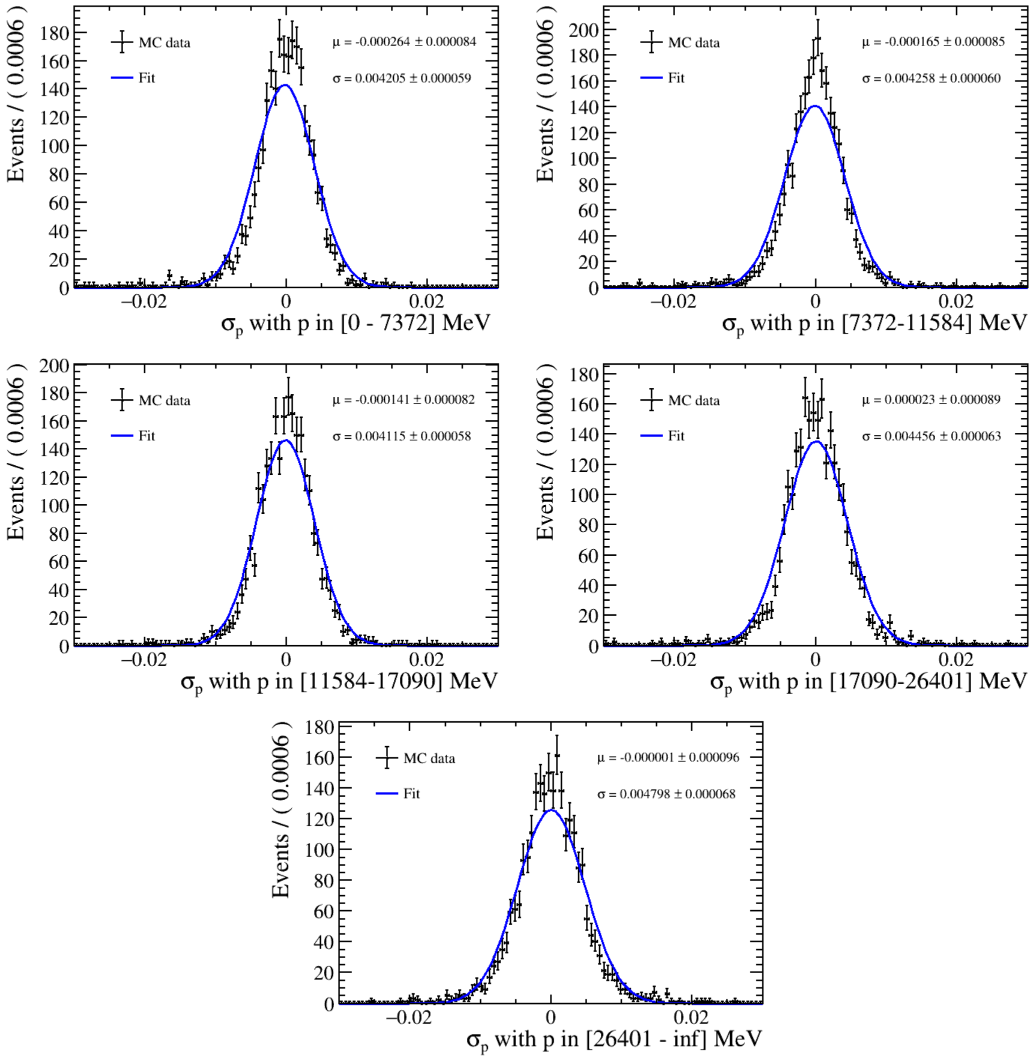

Figure 58: *Pion π^- distributions for $\frac{p-p_{true}}{p_{true}}$, divided into 5 sub-datasets for the brem 1 category. Data points are in black, while the gaussian fit is displayed in blue.*

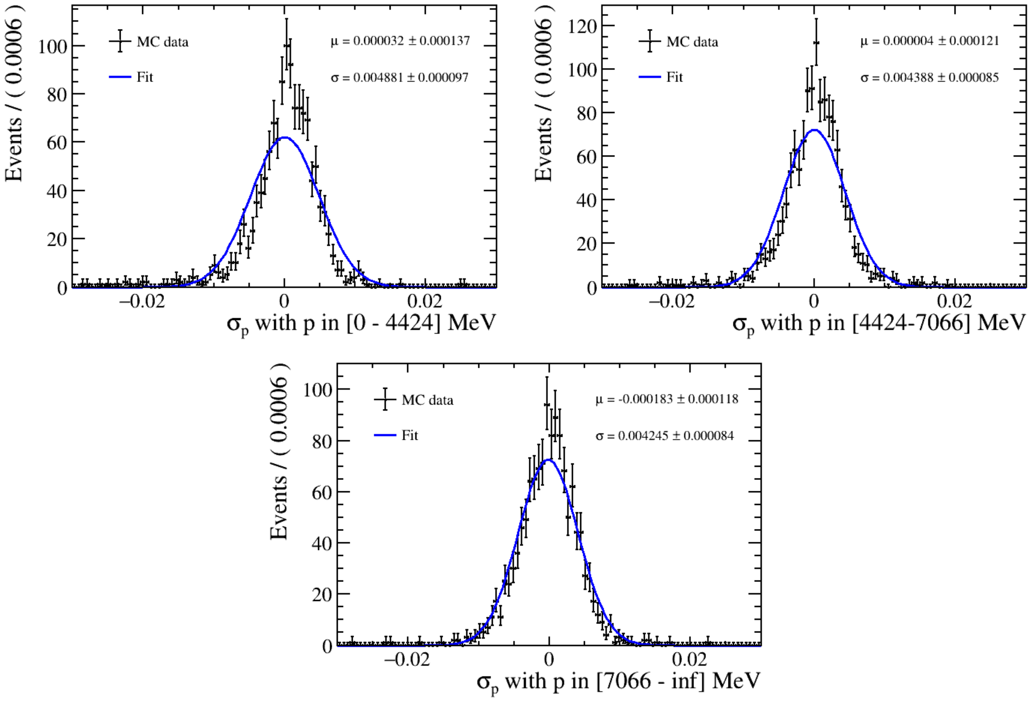

Figure 59: *Soft pion* π_s^+ *distributions for* $\frac{p-p_{true}}{p_{true}}$*, divided into 3 sub-datasets for the brem 0 category. Data points are in black, while the gaussian fit is displayed in blue.*

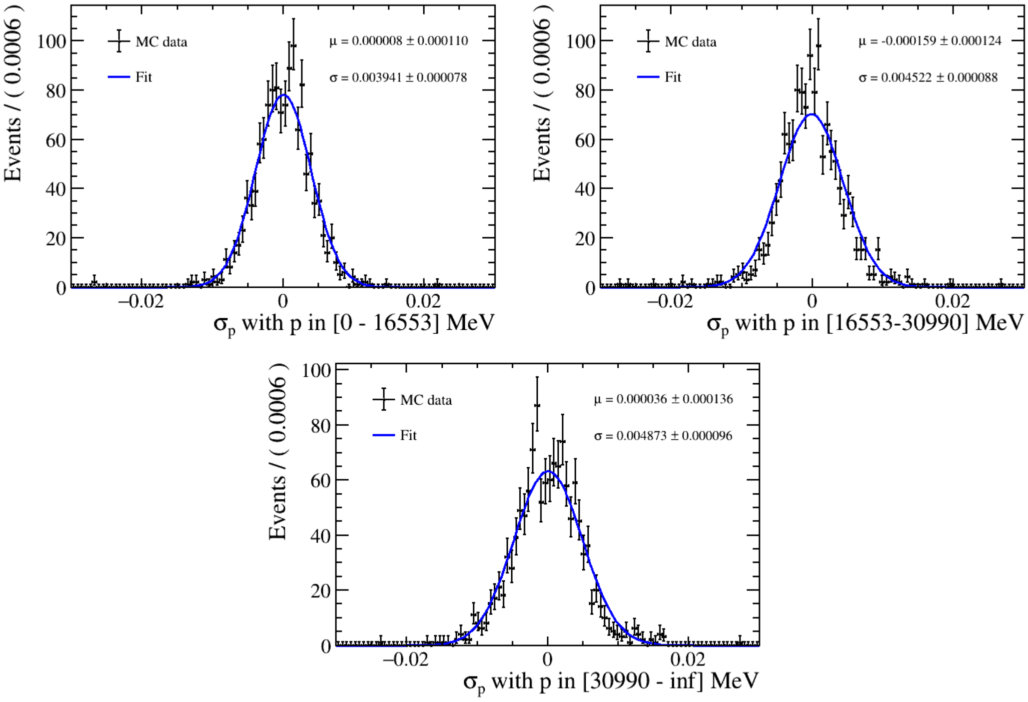

Figure 60: *Kaon K^- distributions for $\frac{p-p_{true}}{p_{true}}$, divided into 3 sub-datasets for the brem 0 category. Data points are in black, while the gaussian fit is displayed in blue.*

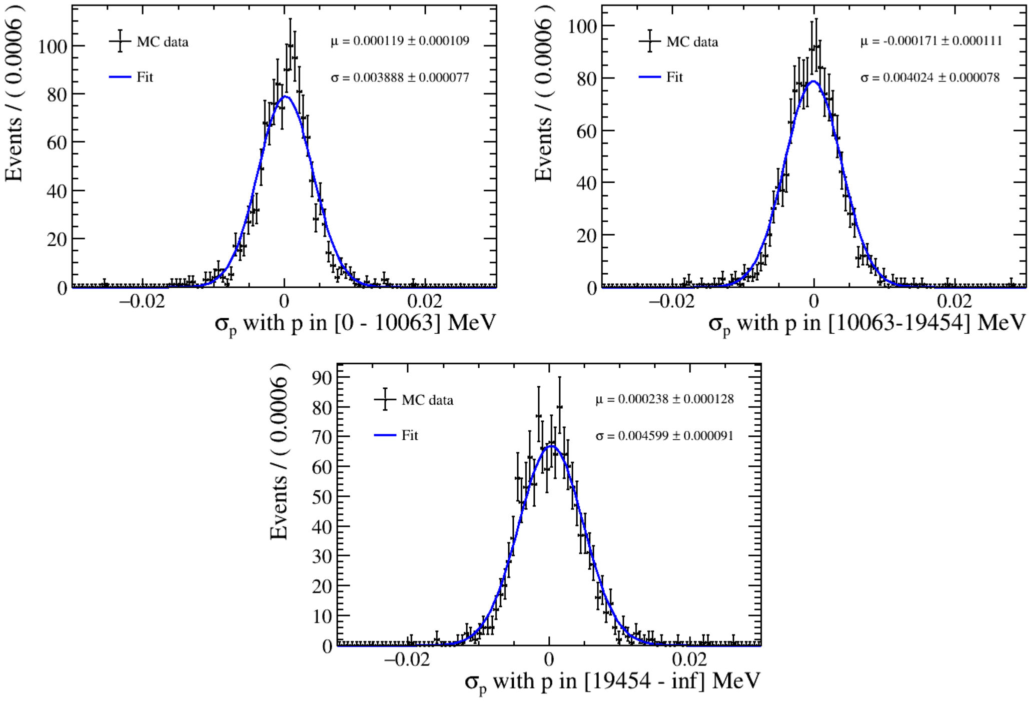

Figure 61: *Pion π^- distributions for $\frac{p-p_{true}}{p_{true}}$, divided into 3 sub-datasets for the brem 0 category. Data points are in black, while the gaussian fit is displayed in blue.*

F RapidSim validation brem 1 category

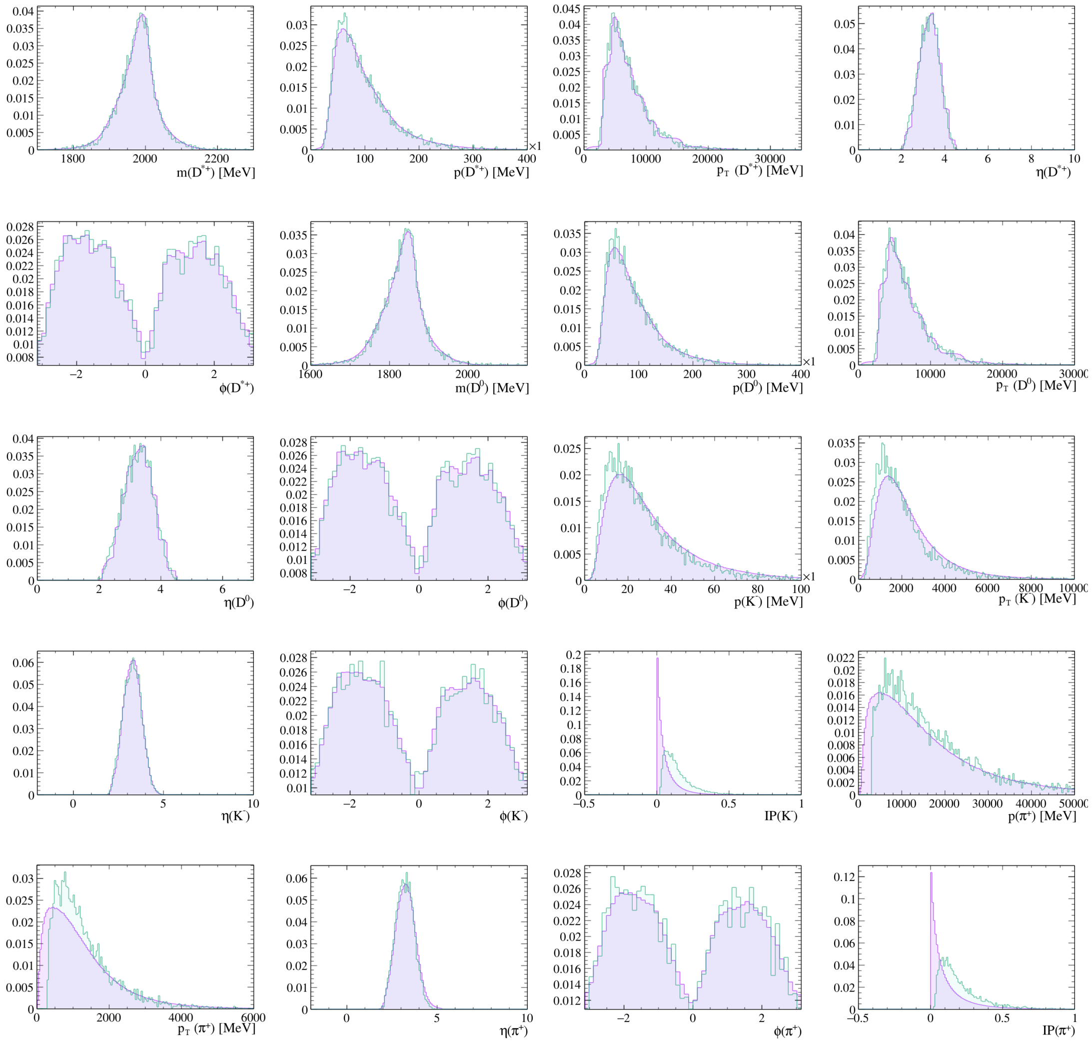

Figure 62: *Comparison between the distributions obtained with the RapidSim simulation (purple) and the official LHCb sample (green) for brem 1 category. The shown variables are topological or kinematical, and the comparison is performed over all particles in the decay.*

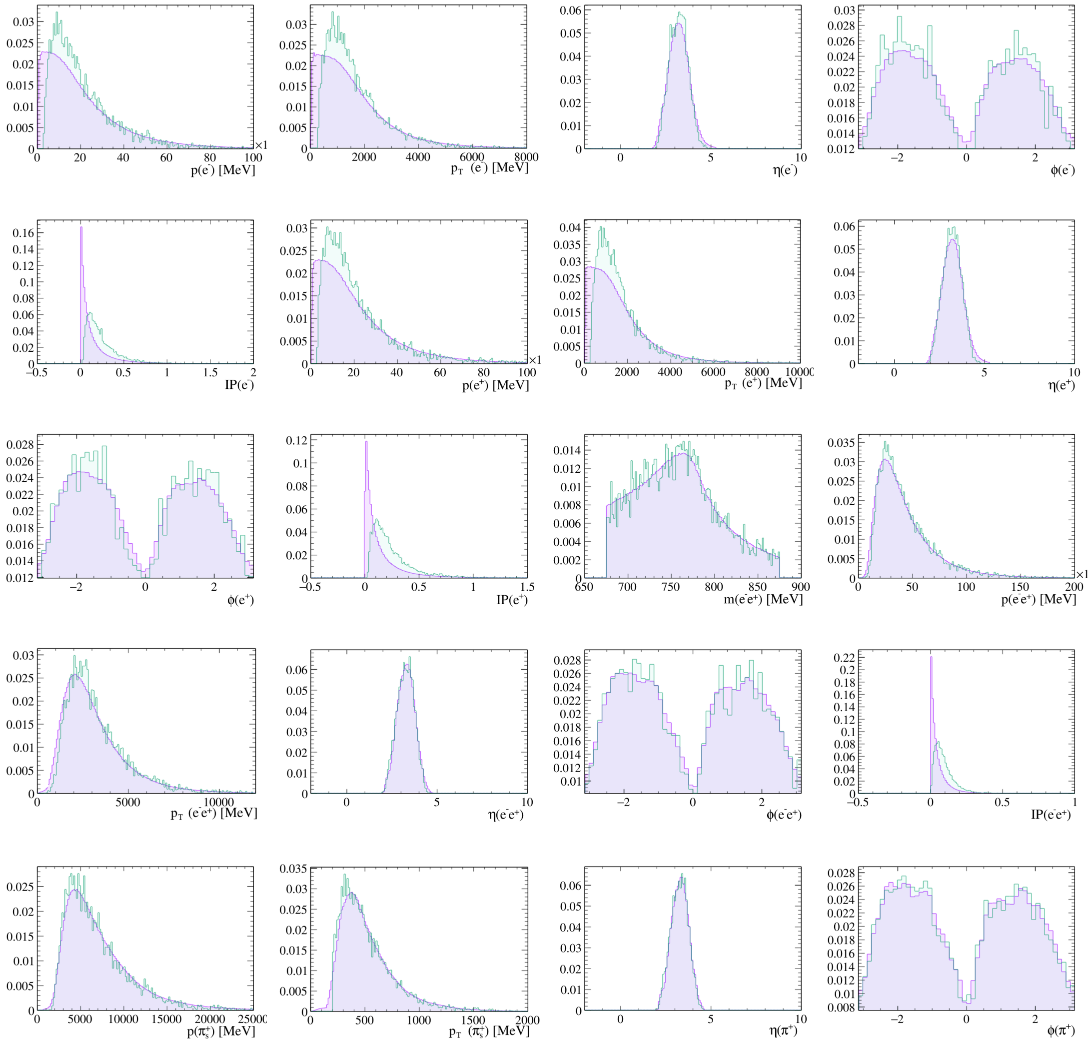

Figure 63: *Comparison between the distributions obtained with the RapidSim simulation (purple) and the official LHCb sample (green) for brem 1 category. The shown variables are topological or kinematical, and the comparison is performed over all particles in the decay.*

G RapidSim validation brem 0 category

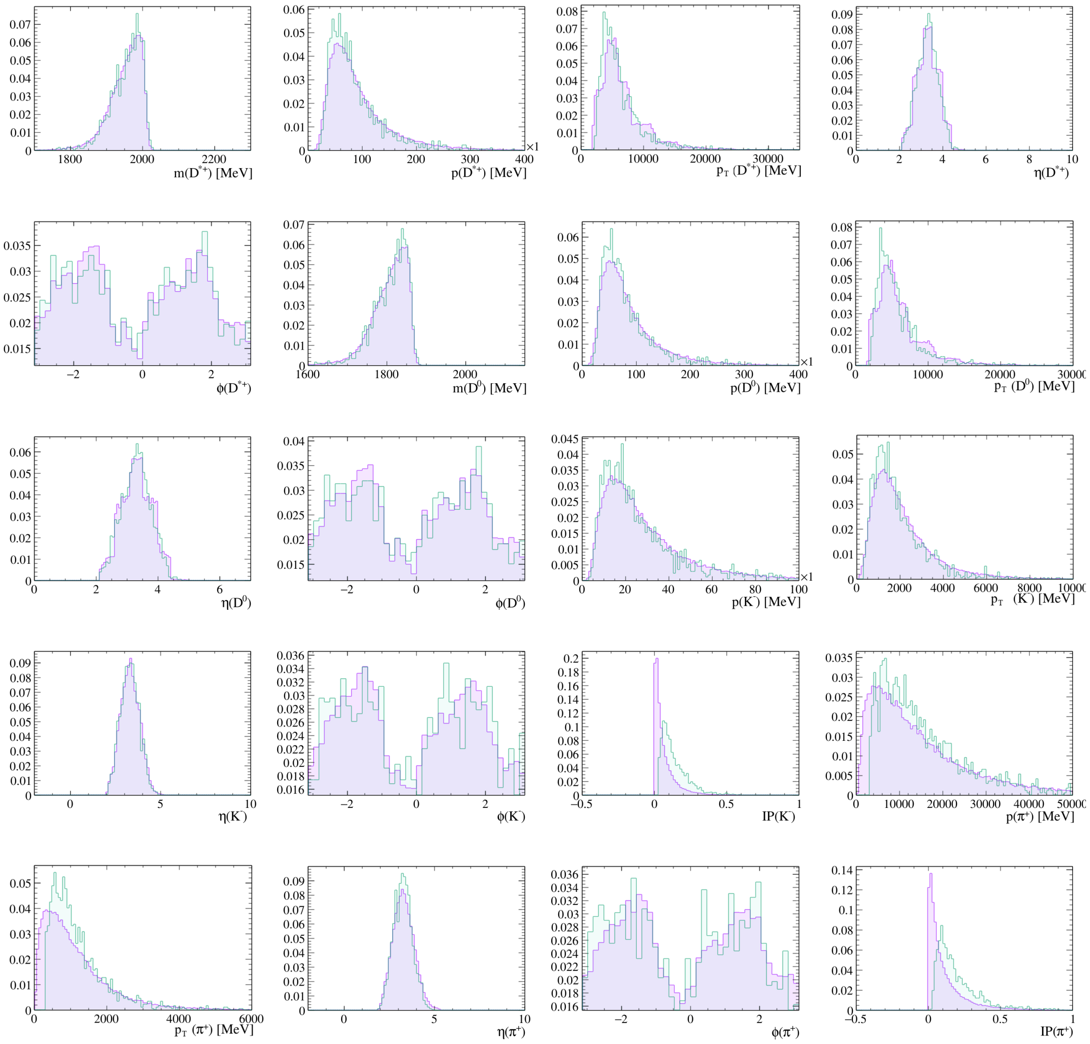

Figure 64: *Comparison between the distributions obtained with the RapidSim simulation (purple) and the official LHCb sample (green) for brem 0 category. The shown variables are topological or kinematical, and the comparison is performed over all particles in the decay.*

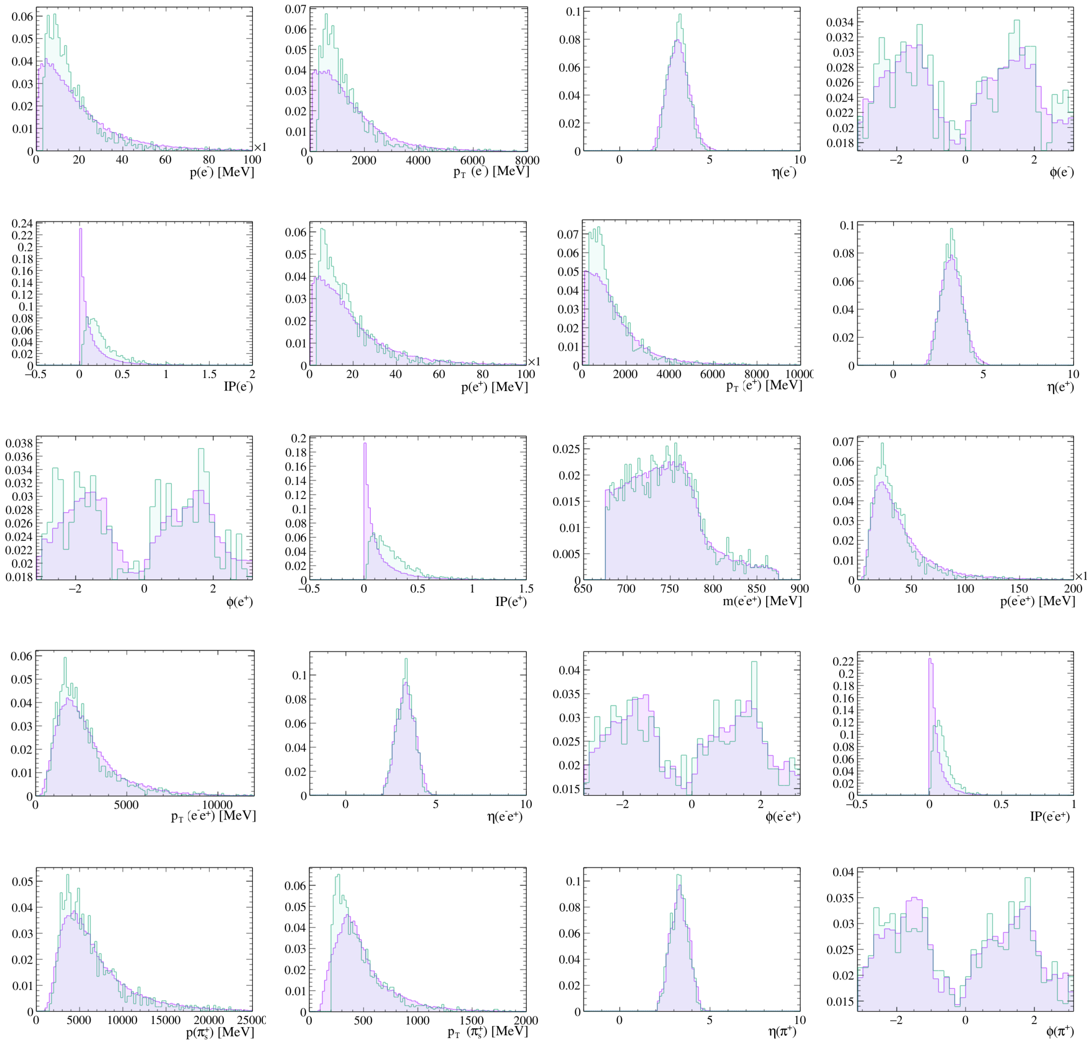

Figure 65: *Comparison between the distributions obtained with the RapidSim simulation (purple) and the official LHCb sample (green) for brem 0 category. The shown variables are topological or kinematical, and the comparison is performed over all particles in the decay.*

References

[1] S. L. Glashow. Partial-symmetries of weak interactions. *Nuc. Phys. 22.4*, 1961. https://doi.org/10.1016/0029-5582(61)90469-2.

[2] Steven Weinberg. A model of leptons. *Phys. Rev. Lett.*, 19:1264–1266, Nov 1967. https://link.aps.org/doi/10.1103/PhysRevLett.19.1264.

[3] Abdus Salam. Weak and Electromagnetic Interactions. *Conf. Proc. C*, 680519:367–377, 1968. https://inspirehep.net/literature/53083.

[4] G. Aad et al. Observation of a new particle in the search for the Standard Model Higgs boson with the ATLAS detector at the LHC. *Physics Letters B*, 716(1), 2012. http://dx.doi.org/10.1016/j.physletb.2012.08.020.

[5] S. Chatrchyan et al. Observation of a new boson at a mass of 125 GeV with the CMS experiment at the LHC. *Physics Letters B*, 716(1), 2012. http://dx.doi.org/10.1016/j.physletb.2012.08.021.

[6] M. Gell-Mann. Isotopic Spin and New Unstable Particles. *Phys. Rev.*, 92:833–834, 1953. https://inspirehep.net/literature/46730.

[7] Kazuhiko Nishijima. Charge Independence Theory of V Particles. *Prog. Theor. Phys.*, 13(3):285–304, 1955. https://inspirehep.net/literature/1616449.

[8] Murray Gell-Mann. A Schematic Model of Baryons and Mesons. *Phys. Lett.*, 8:214–215, 1964. https://doi.org/10.1016/S0031-9163(64)92001-3.

[9] Nicola Cabibbo. Unitary symmetry and leptonic decays. *Phys. Rev. Lett.*, 10:531–533, Jun 1963. https://link.aps.org/doi/10.1103/PhysRevLett.10.531.

[10] Donald H. Perkins. *Introduction to High Energy Physics, 4th edition*. University of Cambridge, 2000.

[11] A.Ceccucci (CERN), Z.Ligeti (LBNL), and Y.Sakai (KEK). CKM Quark-Mixing Matrix. *PDG*, April 2024. https://pdg.lbl.gov/2024/reviews/rpp2024-rev-ckm-matrix.pdf.

[12] Luciano Maiani. The GIM Mechanism: origin, predictions and recent uses, 2013. https://arxiv.org/abs/1303.6154.

[13] J. J. Aubert et al. Experimental Observation of a Heavy Particle J. *Phys. Rev. Lett.*, 33:1404–1406, Dec 1974. https://link.aps.org/doi/10.1103/PhysRevLett.33.1404.

[14] J. E. Augustin et al. Discovery of a Narrow Resonance in e^+e^- Annihilation. *Phys. Rev. Lett.*, 33:1406–1408, Dec 1974. https://link.aps.org/doi/10.1103/PhysRevLett.33.1406.

[15] Makoto Kobayashi and Toshihide Maskawa. CP-Violation in the Renormalizable Theory of Weak Interaction. *Progress of Theoretical Physics*, 49(2):652–657, 02 1973. https://doi.org/10.1143/PTP.49.652.

[16] M. E. Peskin and D. V. Schroeder. *An Introduction to quantum field theory*. Addison-Wesley, 1195.

[17] Aron J. Beekman et al. An introduction to spontaneous symmetry breaking. *SciPost Phys. Lect. Notes 11*, 2019. https://doi.org/10.48550/arXiv.1909.01820.

[18] Frederick J. Gilman and Yosef Nir. Quark Mixing: The CKM Picture. *Ann. Rev. Nucl. Part. Sci.*, 40:213–238, 1990. https://doi.org/10.1146/annurev.ns.40.120190.001241.

[19] M. Bargiotti et al. Present knowledge of the Cabibbo-Kobayashi-Maskawa matrix. *Riv. Nuovo Cim.*, 23N3:1, 2000. https://doi.org/10.48550/arXiv.hep-ph/0001293.

[20] Ling-Lie Chau and Wai-Yee Keung. Comments on the Parametrization of the Kobayashi-Maskawa Matrix. *Phys. Rev. Lett.*, 53:1802–1805, Nov 1984. https://link.aps.org/doi/10.1103/PhysRevLett.53.1802.

[21] F.J. Gilman, K. Kleinknecht, and B. Renk. The cabibbo-kobayashi-maskawa quark mixing matrix. *PDG*, 2004.

[22] Lincoln Wolfenstein. Parametrization of the Kobayashi-Maskawa Matrix. *Phys. Rev. Lett.*, 51:1945–1947, Nov 1983. https://link.aps.org/doi/10.1103/PhysRevLett.51.1945.

[23] C. Jarlskog. Commutator of the Quark Mass Matrices in the Standard Electroweak Model and a Measure of Maximal CP Nonconservation. *Phys. Rev. Lett.*, 55:1039–1042, Sep 1985. https://link.aps.org/doi/10.1103/PhysRevLett.55.1039.

[24] J. Charles et al. CP violation and the CKM matrix: assessing the impact of the asymmetric B factories. *The European Physical Journal C*, 41(1):1–131, May 2005. http://dx.doi.org/10.1140/epjc/s2005-02169-1.

[25] A. Höcker et al. A new approach to a global fit of the CKM matrix. *The European Physical Journal C*, 21(2):225–259, June 2001. http://dx.doi.org/10.1007/s100520100729.

[26] M. Bona et al. The 2004 UTfit collaboration report on the status of the unitarity triangle in the standard model. *Journal of High Energy Physics*, 2005(07):028–028, July 2005. https://arxiv.org/abs/hep-ph/0501199.

[27] M. Bona et al. Model-independent constraints on $\Delta F = 2$ operators and the scale of new physics. *Journal of High Energy Physics*, 2008(03):049–049, March 2008. https://arxiv.org/abs/0707.0636.

[28] UTfit. http://utfit.org/UTfit/ResultsSummer2023SM.

[29] Andrzej J. Buras. Flavor changing neutral current processes. In *28th International Conference on High-energy Physics*, pages 243–270, 10 1996. https://arxiv.org/abs/hep-ph/9610461.

[30] Hector Gisbert, Marcel Golz, and Dominik Stefan Mitzel. Theoretical and experimental status of rare charm decays. *Modern Physics Letters A*, 36(04), 2021. http://dx.doi.org/10.1142/S0217732321300020.

[31] Stefan Hollands and Robert M. Wald. The Operator Product Expansion in Quantum Field Theory, 2023. https://arxiv.org/abs/2312.01096.

[32] Stefan de Boer, Bastian Müller, and Dirk Seidel. Higher-order Wilson coefficients for $c \to u$ transitions in the standard model. *Journal of High Energy Physics*, 2016(8), August 2016. http://dx.doi.org/10.1007/JHEP08(2016)091.

[33] Alessandro Scarabotto. *Search for rare four-body charm decays with electrons in the final state and long track reconstruction for the LHCb trigger*. PhD thesis, Sorbonne Université, 2023.

[34] L. et al. Cappiello. Standard Model prediction and new physics tests for $D^0 \to h_1^+ h_2^- \ell^+ \ell^- (h = \pi, K;\ \ell = e, \mu)$. *J. High Energ. Phys. 2013*, 2013. https://doi.org/10.1007/JHEP04(2013)135.

[35] LHCb Collaboration. Search for $D^0 \to K^+K^-e^+e^-$ and $\pi^+\pi^-e^+e^-$ decays. *Physics Review Letter*, 2024. http://dx.doi.org/10.1103/PhysRevD.111.L091101.

[36] LHCb collaboration. Observation of D^0 meson decays to $\pi^+\pi^-\mu^+\mu^-$ and $K^+K^-\mu^+\mu^-$ final states. *Phys. Rev. Lett. 119 181805*, 2017. https://cds.cern.ch/record/2276004.

[37] R. Aaij et al. Angular analysis of $D^0 \to \pi^+\pi^-\mu^+\mu^-$ and $D^0 \to K^+K^-\mu^+\mu^-$ decays and search for CP violation. *Physical Review Letters*, (22), 2022. http://dx.doi.org/10.1103/PhysRevLett.128.221801.

[38] S. Schael et al. Precision electroweak measurements on the Z resonance. *Phys. Rept.*, 427:257–454, 2006. https://inspirehep.net/literature/691576.

[39] ATLAS Collaboration. Test of the universality of τ and μ lepton couplings in W-boson decays with the ATLAS detector. *Nat. Phys. 17, 813–818*, 2021. https://doi.org/10.1038/s41567-021-01236-w.

[40] R. aajj et al. Measurement of the branching fraction ratios $R(D^{+})$ and $R(D^{*+})$ using muonic τ decays. *Phys. Rev. Lett.*, 134(6):061801, 2025. https://cds.cern.ch/record/2900176.

[41] CERN. https://home.cern/.

[42] Oliver Sim Brüning et al. LHC design report. CERN Yellow Report CERN-2004-003-V-1, CERN, 2004. https://cds.cern.ch/record/782076.

[43] Lyndon R Evans and Philip Bryant. LHC Machine. *JINST*, 2008. https://cds.cern.ch/record/1129806.

[44] Roel Aaij et al. Measurements of prompt charm production cross-sections in pp collisions at $\sqrt{s} = 13$ TeV. *JHEP*, 03:159, 2016. https://arxiv.org/abs/1510.01707.

[45] A. Augusto Alver Jr et al. The LHCb Detector at the LHC. *JINST*, 3:S08005, 2008. https://cds.cern.ch/record/1129809.

[46] LHCb Collaboration. The LHCb Upgrade I. *JINST 19*, 2024. https://arxiv.org/pdf/2305.10515.

[47] K. Akiba et al. The LHCb VELO Upgrade module construction. *JINST 19*, 2024. http://dx.doi.org/10.1088/1748-0221/19/06/P06023.

[48] Erik Aras Papadelis. *Characterisation and Commissioning of the LHCb VELO Detector*. PhD thesis, Vrije U., Amsterdam, 2009. https://repository.cern/records/3mjst-9zx93.

[49] M. D. Galati on behalf of LHCb. The LHCb VELO detector: operation, performance and future upgrades. *42nd International Conference on High Energy Physics (ICHEP2024)*, 2024. https://doi.org/10.22323/1.476.0925.

[50] LHCb magnet. https://lhcb-magnet.web.cern.ch/.

[51] S. Amato et al. LHCb calorimeters. 2000. https://cds.cern.ch/record/494264.

[52] RTA and DPA dataflow diagrams for Run 1, Run 2, and the upgraded LHCb detector. 2020. https://cds.cern.ch/record/2730181.

[53] HLT1 trigger efficiencies in 2024 data. https://lbfence.cern.ch/alcm/public/figure/details/3837.

[54] LHCb Upgrade GPU High Level Trigger Technical Design Report. Technical report, CERN, Geneva, 2020. https://cds.cern.ch/record/2717938.

[55] E.M. Aitala et al. Search for rare and forbidden charm meson decays $D^0 \to V\ell^+\ell^-$ and $hh\ell\ell$. *Phys. Rev. Lett. 86 3969*, 2001. https://doi.org/10.1103/PhysRevLett.86.3969.

[56] M. Ablikim et al. Search for the rare decays $D^0 \to h(h^{(\prime)})e^+e^-$. *Phys. Rev. D97 072015*, 2018. https://doi.org/10.1103/PhysRevD.97.072015.

[57] J. P. Lees et al. Observation of the decay $D^0 \to K^-\pi^+e^+e^-$. *Phys. Rev. Lett.*, 122:081802, Feb 2019. https://link.aps.org/doi/10.1103/PhysRevLett.122.081802.

[58] Wouter D. Hulsbergen. Decay chain fitting with a Kalman filter. *Nuclear Instruments and Methods in Physics Research Section A: Accelerators, Spectrometers, Detectors and Associated Equipment*, 552(3):566–575, November 2005. http://dx.doi.org/10.1016/j.nima.2005.06.078.

[59] A. Hoecker et al. TMVA - Toolkit for Multivariate Data Analysis, 2009. https://arxiv.org/abs/physics/0703039.

[60] Giovanni Punzi. Sensitivity of searches for new signals and its optimization. *eConf*, C030908:MODT002, 2003. https://inspirehep.net/literature/634798.

[61] N. L. Johnson. Systems of frequency curves generated by methods of translation. *Biometrika*, 36(1/2):149–176, 1949. http://www.jstor.org/stable/2332539.

[62] D. C. Craik G. A. Cowan and M. D. Needham. RapidSim: an application for the fast simulation of heavy-quark hadron decays. 2017. https://github.com/gcowan/RapidSim.

[63] Anders Ryd et al. EvtGen: A Monte Carlo Generator for B-Physics. Technical report, HepForge, 2004. https://evtgen.hepforge.org/doc/EvtGenGuide.pdf.

[64] Fernando Abudinén, John Back, Michal Kreps and Thomas Latham. Evtgen — recent developments and prospects. *EPJ Web of Conf.*, 2024. https://doi.org/10.1051/epjconf/202429503012.

[65] Hepforge, IPPP Durham. EvtGen Models. https://evtgen.hepforge.org/doc/models.html.

[66] Bukin PDF. https://root.cern.ch/doc/master/classRooBukinPdf.html.

[67] Crystal ball PDF. https://root.cern.ch/doc/master/classRooCrystalBall.html.

[68] Lucio Anderlini et al. The PIDCalib package. Technical report, CERN, Geneva, 2016. https://cds.cern.ch/record/2202412.

[69] PIDCalib2. https://pypi.org/project/pidcalib2/.